Mitigating Boil-Off in Cryogenic Spacecraft Propellant Tanks

A Major Qualifying Project
submitted to the faculty of
WORCESTER POLYTECHNIC INSTITUTE
in partial fulfillment of the requirements for the
degree of Bachelor of Science
In Aerospace Engineering

By:
Jacob Borowsky
Jack Charbonneau
John Dougherty
Alexander Lagle
Nicholas Masse
Jacob Mitchell
Deep Patel
Rory Veguilla

March 24th, 2023

Approved by: _____

Jagannath Jayachandran, Advisor, Assistant Professor, Aerospace Engineering Department WPI

Abstract

Cryogenic propellants are efficient for aerospace applications, but they experience significant boil-off. This project addressed the challenge of boil-off through analyzing the benefits of different tank material and geometry, and venting systems of a theoretical spacecraft and mission. Experiments for permeability, heat transfer, and venting were conducted to validate these analyses, and a computational model was developed to optimize the tank and quantify the mass lost due to boil-off. Using LCH_4 instead of LH_2, MLI, and adopting a CVS improved thermal efficiency while minimizing mass. Composite material testing indicated that more complex stacking sequences may outperform aluminum in relevant categories, however, this project conveys that AA 2024 was the ideal material selection.

Acknowledgements

We would like to thank the following individuals for their help in developing our understanding of the theory and the best laboratory practices for this project:

- Professor John Blandino
- Nolan Dexter-Brown
- Peter Hefti
- Adriana Hera
- Professor Nikolaos Kazantzis
- Doctor Andre LeClair
- Joel Mathew
- Professor Zachary Taillefer

Finally, the team would like to especially thank our advisor, Professor Jagannath Jayachandran, for his continued help, feedback, and guidance throughout the project.

Table of Contents

List of Figures

List of Tables

Table of Authorship

Section	Primary Author	Secondary Author(s)
Abstract	JC	JD
1.0 Introduction and Problem Statement	JB	JM, RV
1.1 Literature Review	JM	-
1.1.1 Overview of Cryogenic Propellants	JB	NM
1.1.2 Thermal Analysis of Cryogenic Tanks	JB	JC
1.1.2.1 Summary of Heat Transfer	JC	JB
1.1.2.2 External Thermal Loads on Spacecraft	NM	-
1.1.2.3 Internal Thermal Effects and Propellant Boil-Off	JC	JB
1.1.3 Propellant Boil-Off Management Methods	RV	NM
1.1.3.1 Insulation	NM	RV
1.1.3.2 Radiative Cooling of Rotating Spacecraft	JC	JB
1.1.3.3 Venting Techniques	JM	-
1.1.3.4 Active Methods of Boil-off Prevention	RV	-
1.1.4 Cryogenic Propellant Storage Tank Design	JB	-
1.1.4.1 Tank Geometry	JB	-
1.1.4.2 Tank Material	DP	-
1.1.4.3 Unidirectional vs Woven Composites	DP	-
1.1.4.4 Classical Laminate Theory	DP	-
1.2 Project Objectives and Methods	AL	-
1.3 Project Management	JD	-
1.3.1 Members and Roles	JD	-
2.0 Preliminary Design	JM	NM
2.1 Mission Design	AL	-
2.1.1 Delta-V Requirement	AL	JB
2.1.2 Changes in Propellant Levels Throughout Mission Phases	JC	JB
2.2 Spacecraft Design	JB	-
2.2.1 Propellant and Engine Selection	JB	-
2.2.2 Tank Design, Sizing, and Materials	JB	-
2.2.2.1 Tank Design and Sizing	JB	-
2.2.2.2 Tank Material	JB	-
2.2.3 Boil-Off Mitigation Techniques	JM	JC
2.3 Thermal Analysis	JC	-
2.3.1 Preliminary Heat Transfer Calculations	JC	-

2.3.1.1 STK Solar Flux Analysis	AL	-
2.3.2 Simplified Boil-off Model	JC	-
2.3.2.1 Assumptions and Supporting Rationale	JC	-
2.3.2.2 Finalized Model and Boil-Off ODE	JC	-
2.4 Final Design	JB	-
3.0 Experimental Approach	JM	-
3.1 Experimental Reasonings	JM	-
3.1.1 Permeability Testing of Aluminum and CFRP Specimens	JD	DP
3.1.2 Venting Test of Simplified CVS Model	JM	RV
3.1.3 Heat Transfer Analysis of CFRP Layups	AL	-
3.1.4 Computational Determination of Boil-Off Rates	JB	-
3.2 Experimental Methods and Procedures	JM	-
3.2.1 Methods and Procedures for Composite Curing	DP	JD
3.2.1.1 Safety Practices	DP	JD
3.2.2 Methods and Procedures for Permeability	JD	DP
3.2.2.1 Mass Flow Rate Derivation	DP	-
3.2.2.2 Henry's Law Calculations	DP	-
3.2.3 Methods and Procedures for Venting	JM	AL
3.2.4 Methods and Procedures for Heat Transfer	AL	-
3.2.4.1 Cold Plate Design and Assembly	AL	-
3.2.4.2 Heat Lamp Apparatus	AL	-
3.2.4.3 Vacuum Chamber Feedthroughs	AL	-
3.2.4.4 Data Acquisition and Wiring	AL	-
3.2.4.5 Thermal Testing Analysis	AL	-
3.2.5 Methods and Procedure for Computational Determination of Boil-Off Rates	JB	JC
3.3 Experiment Results	-	-
3.3.1 Permeability Testing Results	JD	DP
3.3.2 Venting Testing Results	RV	JM
3.3.3 Thermal Testing Results	AL	-
3.3.3.1 Spectrometer Results and Discussion	AL	-
3.3.3.2 Heat Lamp Flux Calculations	AL	-
3.3.3.3 Thermal Testing Results Without Vacuum	AL	-
3.3.3.4 Thermal Testing Results With Vacuum	AL	-
3.3.4 Computational Determination of Boil-Off Rates Results	JB	JC
3.4 Discussion of Design Results and Overall Conclusions	JB	-

4.0 Challenges and Future Improvements	JB	-
4.1 External Factors	JM	-
4.2 Oversights	JC	JB,NM
4.3 Additional Factors	JM	-
4.4 Recommendations	ALL	ALL
5.0 References	-	-
6.0 Appendix	-	-
6.1 Composite Curing Procedure	DP	JD
6.2 Multilayer Insulation Construction Procedure	NM	-
6.3 Thermal Testing Procedure	AL	-
6.4 Thermal Testing Microcontroller Script	AL	-
6.5 Permeability Testing Data	JD	DP
6.6 Valve Testing Script and Procedure	JM	AL
6.7 Boil-Off Model MATLAB Script	JC	JB
6.8 Initial Determination of Boil-Off Rates via Excel Spreadsheet	JB	JC
6.9 Rotating Spacecraft Solar Flux Excel Data Table	JC	-
6.10 General Fluid System Simulation Program	NM	-
6.11 Transient Model for Air Flow MATLAB Script	RV	-

1 Introduction and Problem Statement

In spaceflight, selecting the correct propellant type and propulsion method is vital to the success and design of an efficient mission. There are three main methods of propulsion: bipropellants (bi-props), monopropellants (mono-props), and electric propulsion (EP). Bi-props utilize a chemical fuel and oxidizer to impart large amounts of thrust from the launch vehicle, making them ideal for take-off and landing. Mono-props utilize a chemical fuel that reacts with a catalyst to produce thrust; as a result, they impart a smaller thrust than that of bi-props, but are simpler and more affordable, making them better suited for launching lighter payloads or for usage in low-thrust scenarios such as attitude control. Finally, EP systems expel accelerated ions from a gas stored onboard to produce thrust. EP systems are incredibly light compared to bi-props and mono-props, but since these ions are so small the impulse imparted on the spacecraft is minuscule and impractical for high thrust scenarios like take-off, but ideal for long periods of slow acceleration, such as transferring payloads to another planet or maintaining an orbit (Sutton & Biblarz, 2017).

An immense amount of energy is required to launch mass to Earth's orbit or for interplanetary missions, and it only increases for crewed missions with the addition of life support systems. Furthermore, rocket launches are very expensive. SpaceX's Falcon 9 costs $2,720 USD per kilogram to launch (Jones, 2018). Cryogenic propellants address this issue with their "dramatically [increased] specific impulse (I_{sp}), or the amount of thrust delivered per unit mass of rocket fuel, providing much higher performance than conventional propellants" (Boen, 2013). As a result of this increased efficiency, cryogenic propellants can significantly reduce the amount of propellant required, and therefore mass, as opposed to the use of non-cryogenic propellants, while increasing performance and meeting mission requirements.

Cryogenic propellants must be stored at 120 K (-153 ℃, -244 ℉) or lower to remain liquid for the purpose of more efficient energy storage (ASHRAE Terminology, n.d.). The chemical reactants used in rocket propulsion, such as hydrogen and oxygen, are stable gases at room temperature, but liquids are denser than gases, so they have a higher energy density (energy per unit volume). This means more energy can be packed into a given volume of liquid propellants than of gaseous ones. However, hydrogen and oxygen have boiling points of -423 ℉ (-253 ℃) and -298 ℉ (-183 ℃) respectively, so they must be stored below these temperatures

and at their respective vapor pressures to remain liquid and utilize the increased energy density (Krishnan, 2010; Desert, 2001).

The primary problem with cryogenic propellants is known as boil-off. When these liquids are exposed to heat sources that induce temperature gradients, and therefore heat transfer via radiation, conduction, and convection, the liquid boils into a gas. As a result, the internal pressure of the tank increases. To alleviate the rise in pressure, the gases inside the tank must be vented out. If the gas is not released, the tank could rupture and result in catastrophic failure, and the usable amount of liquid propellant decreases.

Passive and active solutions are used to mitigate this issue, such as insulation and refrigeration, respectively. However, insulation does not completely prevent thermal energy from transferring into the propellant, and refrigeration requires additional power systems, which adds mass to the spacecraft. To avoid increasing the mass cost of launch and spaceflight systems, boil-off must be mitigated through informed propellant choice and tank design.

Liquid hydrogen (LH_2) and liquid oxygen (LOx) is the most common cryogenic bi-prop combination due to their superior performance (i.e., energy density) compared to other cryogenic propellants. However, LH_2's low temperature and affinity for leakage make it difficult to work with. Additionally, LH_2 has a density of 71 g/L (significantly less than water), so it must be stored in large tanks, increasing the mass and cost of missions. Larger tanks also result in a larger surface area and a smaller surface-to-volume ratio; as these parameters increase and decrease, respectively, the area for heat to transfer into the tank also increases, resulting in a higher rate of boil-off (Desert, 2001).

Due to these challenges, liquid methane (LCH_4) has risen in popularity as an alternative fuel due to its higher boiling point, comparable energy density, and higher density than LH_2 (Krishnan, 2010; Native Dynamics, 2015). As a result of its higher density LCH_4 can be stored in smaller tanks (given similar propellant mass requirements) at temperatures that decrease temperature gradients compared to LH_2, all while maintaining impressive performance, reducing costs, and mitigating factors that contribute to increased boil-off rates.

Boil-off can be further reduced through choices in propellant tank design, namely in its geometry and material selection. Spherical tanks are the best shape for minimizing weight and boil-off, while still meeting structural requirements, as they have the smallest surface-to-volume ratio among common shapes. However, spheres are difficult to incorporate into the profile of a

rocket and its fairing, which is important in the launch phase of a mission when aerodynamic forces are present. Therefore, many rocket propellant tanks are shaped like capsules, as shown in Figure 1 (Werner & Bolt, 2006).

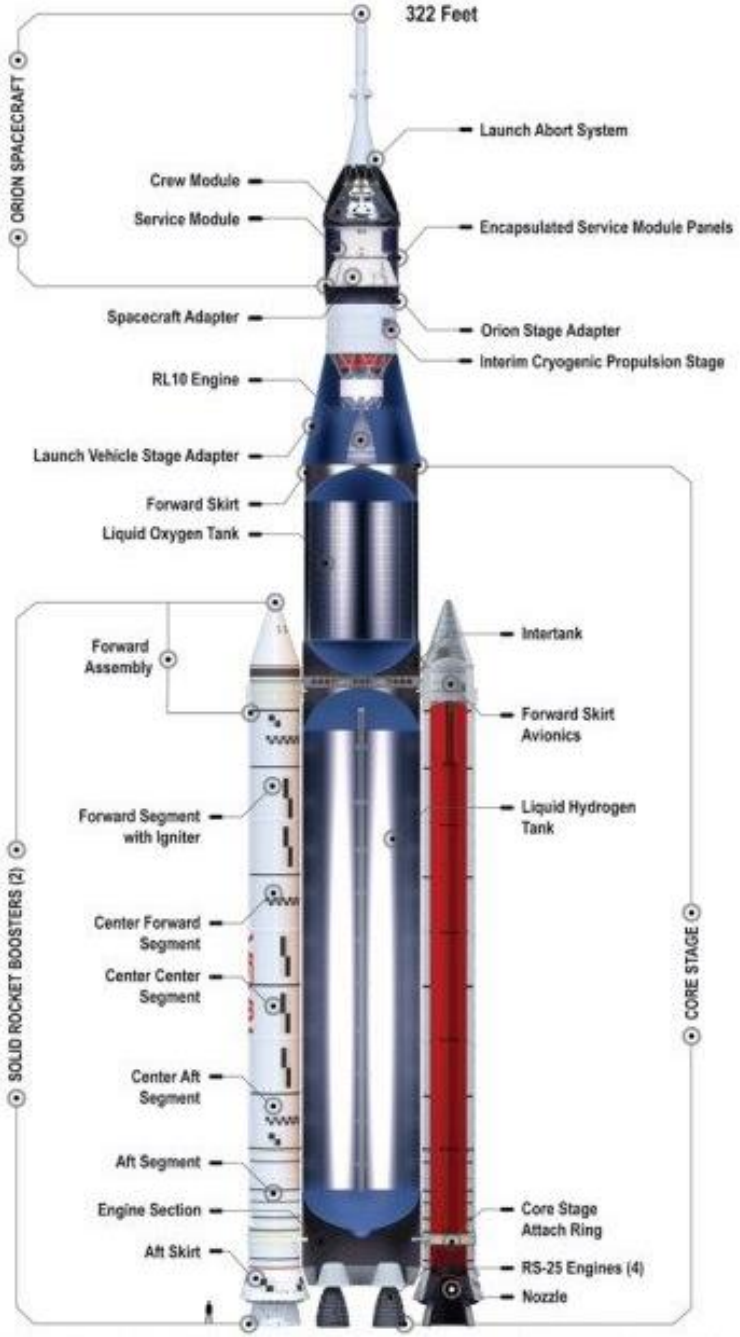

Figure 1: Cutaway of NASA's Space Launch System, showcasing its capsule-shaped LH_2 and LOx tanks (Kanable, 2022)

Additionally, metals commonly used to construct cryogenic tanks, such as titanium and aluminum, have high densities and high thermal conductivities, contributing to increased weight and rate of heat transfer (via conduction), respectively. To mitigate these issues, research has been conducted into the use of composite materials in the construction of cryogenic tanks. Composite materials consist of two or more materials with different chemical and physical properties combined to achieve certain desired characteristics. Compared to metallic alloys, composites have a higher specific strength, lower density, and lower thermal conductivity. Therefore, these materials are stronger, lighter, and more efficient at mitigating heat transfer via conduction than metal alternatives (Arnold et al., 2007).

Based on this information, this project's goal was to design different cryogenic propellant systems, based on choices in cryogenic fuel and oxidizer, tank material, tank design, and mission. Furthermore, analyses were conducted to determine how these factors affect the boil-off rates of said cryogenic propellants. Specifically, this project focuses on analytically comparing the use of LH_2/LOx and LCH_4/LOx as cryogenic propellants, and numerically and experimentally comparing aluminum and carbon fiber reinforced polymers (CFRP) as cryogenic tank materials, to determine how the chemical and mechanical properties of these materials affected the boil-off rate of the cryogenic propellants. Finally, based on these design choices, this project sought to verify the efficacy of a venting system to prevent over pressurization of the designed cryogenic tanks due to gases produced by boil-off.

1.1 Literature Review

In the process of preparing to solve the problems of cryogenic propellant, several topics were researched including types of propellants, methods of heat transfer, boil off mitigation techniques, venting strategies, and materials used for the construction of cryogenic tanks. This research provided an understanding of the issue and served as a basis for further research and development of specific project objectives.

1.1.1 Overview of Cryogenic Propellants

Rockets use chemical thrusters to deliver payloads to space. These thrusters utilize the energy stored within molecules like hydrogen (H_2), oxygen (O_2), and hydrazine (N_2H_4) to produce thermal energy through chemical reactions within the vehicle's engines. The hot,

expanding gas is then focused through a nozzle, expelling it from the engine and generating thrust in the opposite direction.

Chemical propellants exist within two categories: bi-props and mono-props. Bi-props utilize two reactants–a fuel and an oxidizer–to produce thrust. Mono-props utilize a single fuel and a catalyst to produce thrust. Conversely, electric thrusters emit accelerated ions from gas stored aboard the spacecraft like Xenon to impart an impulse on the vehicle (Sutton & Biblarz, 2017). Electric and mono-prop thrusters are common in the space industry, but since these systems lack oxidizers and do not require their fuel to be cryogenically stored (as they are efficient enough to accomplish their designed mission), they are by definition not cryogenic propellants and therefore outside the scope of this project. As a result, they were not considered beyond a basic level of understanding.

Some of the most common bi-prop fuel and oxidizer combinations are LH_2 and LOx, RP-1 (Rocket-Propellant 1, a kerosene derivative) and LOx, hydrazine (N_2H_4) and nitrogen tetroxide (NTO), and LCH_4 and LOx, respectively, as shown in Figure 2.

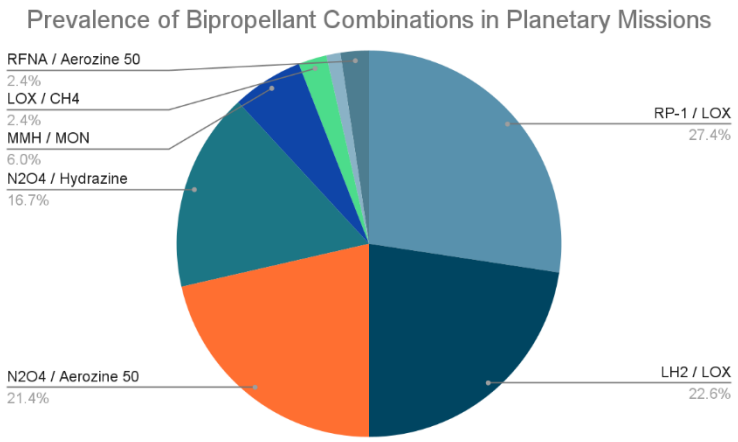

Figure 2: Prevalence of bipropellants for across space missions from 1958-2016 (Siddiqi, 2018)

The propellant combinations included RP-1 (which was used on the first stage of NASA's Saturn V and SpaceX's Falcon 9), hydrazine (including its derivatives monomethyl hydrazine (MMH) and Aerozine 50), and oxidizers such as NTO are all stable at STP conditions and need not be stored cryogenically, so they too are by definition not cryogenic propellants and beyond the scope of this project.

LH_2/LOx is a common propellant combination due to its efficiency, namely its I_{sp}. LH_2/LOx rocket engines typically have a specific impulse of ~450s, which is the highest of any viable chemical propulsion system, making it the most efficient propellant combination for producing thrust per unit mass (Engelbrecht, 1997). Additionally, the reaction of hydrogen and oxygen produces only steam, making LH_2/LOx an environmentally safe option compared to RP-1 in terms of greenhouse gas output.

At standard temperature and pressure (STP), hydrogen has a density of 0.0837 g/L and an energy density of 0.01 MJ/L. Its specific energy (energy per unit mass), which does not change with conditions, is 142 MJ/kg, Hydrogen can efficiently store high amounts of energy per unit mass, as demonstrated by its specific energy. However, because hydrogen is a gas at STP conditions, its energy density is low. On the other hand, LH_2 has a density of 71 g/L, resulting in an energy density of 9 MJ/L (McCarty, 1975). For comparison, kerosene, from which RP-1 is derived, has a density of 830 g/L, a specific energy of 46.2 MJ/kg, and an energy density of 38 MJ/L (Native Dynamics, 2014). So, while it contains more energy per unit volume due to its greater density, its lower specific energy means it's not as efficient as storing energy, exemplifying the superior efficiency of hydrogen as a cryogenic propellant.

Despite its powerful capabilities, hydrogen is difficult to store effectively without leaking through fuel lines and propellant tanks due to its small size, contributing to increased boil-off rates before and after launch. Additionally, LH_2's low boiling point makes it incredibly difficult to store and transport as it becomes volatile when the storage tank contacts the ambient air, resulting in boil-off (Zona, 2010). LH_2's low density necessitates massive tanks for storage, and its high specific impulse does not always justify this increased mass. Therefore, most launch vehicles do not use hydrogen fueled first stage boosters to leave Earth's atmosphere. The benefits of hydrogen are typically realized for second or third rocket stages where high efficiency engines with lower thrust to mass ratios are required to place payloads into the desired orbit or high energy transfers to the moon, other planets, or geostationary Earth orbit (GEO) (Sutton & Biblarz, 2017). This trade-off makes other fuels more appealing for some applications and is one reason why liquid methane (LCH_4) is currently being explored as an alternative.

For example, United Launch Alliance is replacing its entirely hydrogen fueled Delta IV Heavy rocket with a next generation vehicle known as Vulcan, which has a LCH_4/LOx and solid rocket booster powered first stage, and a LH_2/LOx fueled second stage. Vulcan will be able to

launch heavier payloads and will have a greater thrust at liftoff due to the higher density of its first stage propellant even though the Delta IV Heavy is a significantly larger rocket (Wang & Lantz, 2021).

LCH_4 is also planned for use in SpaceX's Starship, which was chosen due to its availability for production in-situ on Mars (NASA Johnson Space Center, 2013). Alongside this aspect of Starship's mission, methane's properties make it an attractive alternative to hydrogen for general use. LCH_4 has a density of 423 g/L, a specific energy of 55 MJ/kg, and an energy density of 24 MJ/L (Native Dynamics, 2014). So, while its energy storage capabilities are not as great as hydrogen's, it is still efficient and exceeds the capabilities of other propellants like RP-1. Additionally, methane has the lowest hydrogen-to-carbon ratio among all hydrocarbons, making it another environmentally safe option compared to RP-1 in terms of greenhouse gas output.

What LCH_4 lacks in sheer performance against LH_2, it makes up for in its potential to mitigate boil-off. Methane has a boiling point of -260 °F (-162 °C), which is significantly greater than hydrogen's, making it less volatile to handle and store, thereby reducing its rate of boil-off when in contact with the ambient environment (Krishnan, 2010). Additionally, oxygen's boiling point is significantly closer to the boiling point of methane than to that of hydrogen. Therefore, LCH_4 and LOx propellant tanks could share common support structures since they are stored at similar temperatures, whereas LH_2 and LOx cannot. This design choice would reduce the total spacecraft mass.

LCH_4's density is also higher than LH_2's, which means more propellant can fit in a smaller space by mass. This results in smaller tanks, requiring a less massive spacecraft that experiences less heat transfer, and therefore boil-off, than a traditional LH_2/LOx rocket. Finally, another measure that can be used to compare each fuel's effectiveness in mitigating boil-off is their enthalpy of vaporization. This measures the energy required to be added to a certain amount of liquid to turn said amount into a gas, and using publicly available data, can be calculated as

$$\Delta H_{vap} = H_{gas} - H_{liquid} \tag{1}$$

Where H_{gas} is the enthalpy of a substance in the gaseous phase, and H_{liquid} is the enthalpy of the same substance in the liquid phase. At its boiling point and vapor pressure LCH_4 has an enthalpy of vaporization of 509 kJ/kg (Majer & Svoboda, 1985). Conversely, at its boiling point LH_2 has an enthalpy of vaporization of 447 kJ/kg (McCarty, 1975), showcasing that more energy, i.e.,

heat, is required to boil a kilogram of methane than hydrogen, therefore suggesting LCH_4 is more resistant to boiling off, barring other factors. For comparison, the enthalpy of vaporization of oxygen at its boiling point is 213 kJ/kg (Roder & Weber, 1972). Table 1 summarizes important parameters from this section.

Table 1: Properties of LH_2, LCH_4, and LOx

	Propellant		
	LH_2	LCH_4	LOx
Density (kg/m^3)	71	421	1149
Boiling Point (°C)	-253	-162	-183
Specific Energy (MJ/kg)	142	55	N/A
Energy Density (MJ/L)	9	24	N/A
Enthalpy of Vaporization at boiling point and vapor pressure (kJ/kg)	447	509	213

1.1.2 Thermal Analysis of Cryogenic Tanks

The issue of boil-off is one of heat transfer. To understand the main drivers of boil-off, the team conducted research into existing thermal analyses performed on space faring cryogenic tanks. First, the different modes of heat transfer were investigated to understand the phases of heat transfer into the propellant tanks and propellant. Next, the external sources of heat on the tanks were researched to quantify the magnitude of the incident flux on the spacecraft. Finally, the behavior of the propellant within the tanks was researched to understand the energy flow and distribution, giving the team a method to estimate the rate of boil-off.

1.1.2.1 Summary of Heat Transfer

Thermodynamics provides the foundation for understanding the transfer of energy to or from a system based on its interactions with its surroundings. This transfer of energy is defined by two distinct modes: work and heat transfer. Work requires an agent to exert a force over a distance, or a change in the volume of the system. Heat is thermal energy in transit due to a spatial temperature difference. This process can occur in three distinct modes pictured in Figure

3: conduction, convection, and radiation. Each process can be quantified in terms of an appropriate rate equation which computes the amount of energy being transferred per unit time (Bergman et al., 2011).

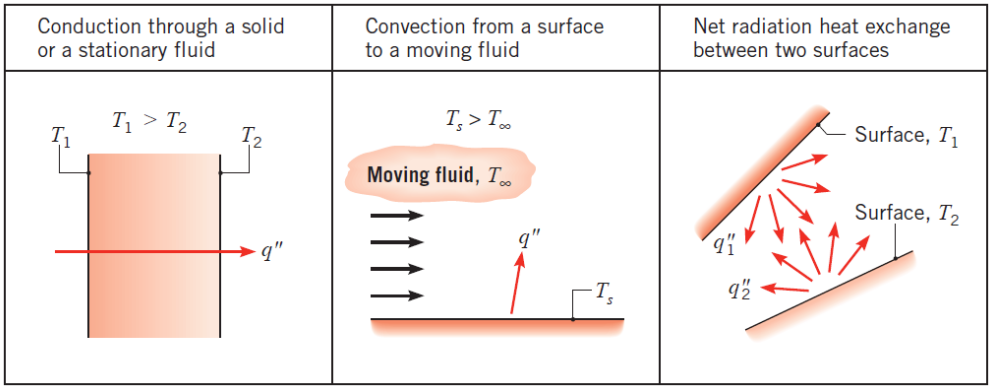

Figure 3: Conduction, convection, and radiation modes of heat transfer (Bergman et al., 2011)

Conduction

Conduction is the transfer of energy from one object to another by direct contact. More specifically, it is the transfer of energy from the more energetic to the less energetic particles of a substance due to atomic level interactions. While most normally associated with the heat transfer across a solid, conduction occurs in gases, liquids, and solids. Naturally, energy (temperature) will flow from a higher concentration to a lower concentration. In liquids and gases, molecules are constantly colliding due to random motion, and as they are doing so, a transfer of energy from the more energetic to the less energetic molecules must occur. This process is accelerated in liquids as the particles are more closely spaced. Conversely, in solids, lattice vibration defines the movement of particles and therefore the transfer of energy (Bergman et al., 2011).

The rate equation which defines conduction is known as Fourier's Law. In a one-dimensional model, the rate equation is expressed as:

$$\dot{q}_x'' = -k\frac{dT}{dx}$$

The heat flux, $\dot{q}_x''$ $[W/m^2]$ is the heat transfer in the x-direction per unit area perpendicular to the direction of transfer. It is equal to the temperature gradient, $\frac{dT}{dx}$, in this direction, multiplied by the material's thermal conductivity, k $[W/m \cdot K]$. This property defines the ability of a specific material to transport thermal energy through its molecules. The minus sign indicates the natural

flow of heat being in the direction of decreasing temperature. Since the heat flux value is a value per unit area, the heat rate,$\dot{q}_x$ $[W]$, can be found by taking the product of the flux and the area it is incident upon such that:

$$\dot{q}_x = \dot{q}_x{}'' \cdot A$$

Convection

Convective heat transfer defines how heat energy moves is a fluid based on the characteristics of its flow. Like conduction, convection considers the random molecular motion of the material, but this is in addition to the bulk motion of the fluid. Where conduction through fluids is considered a stagnant, or zero flow condition, convection provides a method to calculate how energy is transferred by a variety of flow conditions. This heat transfer occurs between a fluid in motion and a bounding surface when a temperature difference exists.

A phenomenon crucial to understanding convective heat transfer is the formation of the fluid boundary layer. As the fluid flows over the bounding surface, the two interact in such a manner that the fluid begins to slow down, forming a velocity distribution that varies from zero at the surface to a bulk fluid flow value u_∞, known as the hydrodynamic boundary layer. Similarly, if there is a difference between the surface temperature and the bulk flow temperature, a temperature gradient forms which varies from T_S at the surface to T_∞. These two distributions are pictured in Figure 4. Convective heat transfer will occur from the surface to the outer flow if $T_s > T_\infty$ (Bergman et al., 2011).

Within the mode of convective heat transfer, sub-classifications exist based on the nature of the flow. Forced convection occurs when the flow is generated by an external force such as a fan. Free convection occurs due to the buoyancy forces generated by temperature dependent density distributions. These flow conditions are not independent of each other and can be modeled together through mixed flow conditions. Regardless of the fluid flow's nature, the convective heat transfer process is found through the Newton's Law of Cooling rate equation.

$$\dot{q}'' = h(T_s - T_\infty)$$

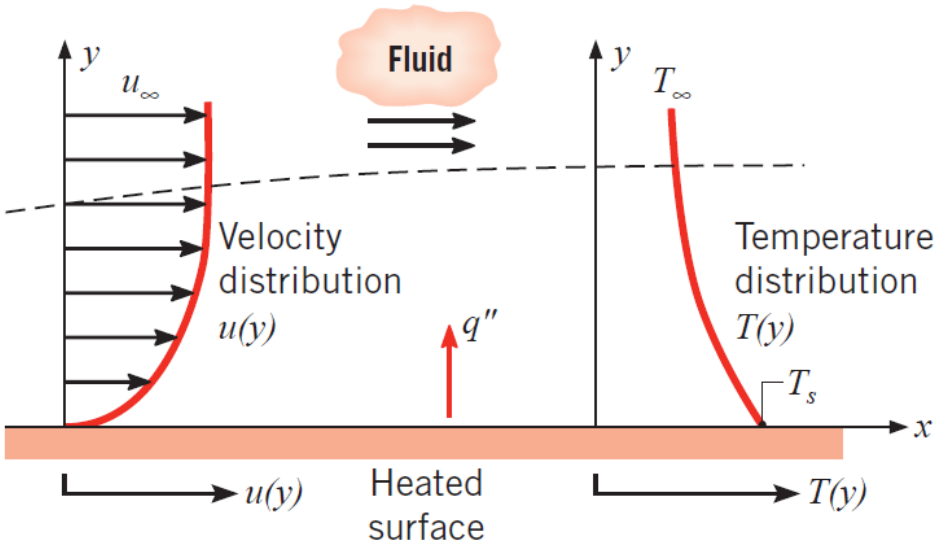

Figure 4: Boundary layer development in convective heat transfer (Bergman et al., 2011)

As previously mentioned, T_S represents the surface temperature and T_∞ is the bulk flow temperature. This equation supports the conclusion that convective heat transfer, q'' $[W/m^2]$, only occurs when a temperature gradient exists at a rate proportional to the convective heat transfer coefficient, h. This coefficient is a property dependent on the conditions at the boundary layer and often is the main quantity to be determined in a convective heat transfer study. Figure 5 displays useful approximate ranges for the value depending on simplified fluid flow classification and thermophysical conditions.

Process	*h* (W/m² · K)
Free convection	
Gases	2–25
Liquids	50–1000
Forced convection	
Gases	25–250
Liquids	100–20,000
Convection with phase change	
Boiling or condensation	2500–100,000

Figure 5: Typical values of the convective heat transfer coefficient (Bergman et al., 2011)

Radiation

The last mode of heat transfer is radiation. Like conduction, radiation is often only associated with the energy emitted by solid matter, however, this phenomenon also occurs in gases and liquids. While convection and conduction heat transfer utilize the motion of particles for the transfer of thermal energy, radiative energy occurs through electromagnetic waves. Importantly related to this is the fact that unlike the previous two modes of heat transfer, radiative heat transfer can occur, and occurs most efficiently, in a vacuum.

The release, or emission, or radiation from a surface is a process that is dependent upon its own thermal energy. This rate of energy release, known as surface emissive power, E, has an upper limit defined by the Stefan-Boltzmann law. For a perfect radiator, the maximum amount of energy that can be released through radiation is given by:

$$E_b = \sigma T_s^4$$

where E_b is proportional to the product of the Stefan-Boltzmann constant, σ ($5.67 \cdot 10^{-8}[W/m^2 \cdot K^4]$), and the absolute temperature of the surface, T_s, raised to the fourth power. This perfect radiator is called a blackbody radiator and is the basis for comparison for all realistic radiating bodies. Emissivity, ϵ, has values in the range of $0 \leq \epsilon \leq 1$, and provides a measure of how efficient a surface is at emitting energy compared to a blackbody radiator (which is represented by $\epsilon = 1$). A body that has an emissivity less than one is considered an 'imperfect' radiator or a 'grey body'. To perform calculations, grey bodies are assumed to have a constant emissivity over all wavelengths and temperatures. These surfaces do not exist in reality but offer a valuable approximation relative to the radiative performance of a blackbody. Applying the grey body approximation to the Stefan-Boltzmann law yields

$$\mathrm{E} = \epsilon \sigma T_s^4$$

Where E represents the surface emissive power of grey bodies and is now additionally proportional to the radiative surface property emissivity, ϵ,. Specific values of ϵ are strongly dependent upon the surface material and its finish (Bergman et al., 2011).

While the Stefan-Boltzmann law considers the release of radiative energy from matter based on its temperature, radiation can also be incident upon a surface from another source. The irradiance, G, is defined as the rate at which radiation is incident upon a given surface area. A portion of this incident radiation will be absorbed by the surface, increasing its thermal energy at a rate proportional to

$$G_{abs} = \alpha G$$

where α represents the surface absorptivity property and is given in the range of $0 \leq \alpha \leq 1$. In addition to the surface absorptivity, the material is also defined by the surface reflectivity ρ and the transmissivity of the body, τ. The absorptivity value of a surface is dependent upon these material properties in addition to the nature of the incident radiation. Surface reflectivity is more specifically determined by the diffuse reflectivity ρ_d and specular reflectivity ρ_s constants. Therefore, the outgoing radiation occurs at a rate of:

$$G_{ref} = (\rho_d + \rho_s)\mathrm{G}$$

where $\rho = \rho_d + \rho_s$ represents the surface reflectivity in given in the range of $0 \leq \rho \leq 1$. The rate at which radiation is transmitted through a body is similarly defined by:

$$G_{tran} = \tau G$$

where the transmissivity of a body is represented by the factor τ given in the range of $0 \leq \tau \leq 1$ and may occur in bodies that are considered semi-transparent (Bergman et al., 2011).

For all radiating bodies the absorptivity, reflectivity, and transmissivity are related to one another by the first law of thermodynamics. The law requires that the sum of the rate of radiative heat transfer by each property is equal to the overall incident radiation G. Looking purely at the material specific variables, they are internally related to one another by:

$$\alpha + \rho + \tau = 1$$

A surface can be considered either opaque or semitransparent, defining how the transmission of radiation through the surface will be treated. An opaque surface is one where radiation is not transmitted through the body, and therefore $\tau = 0$. A semitransparent surface accounts for the transmission of radiation through the body such that $\tau < 1$. When the absorptivity $\alpha < 1$, and the surface is opaque, portions of the irradiation are reflected based on ρ. Most opaque bodies behave as ideal gray bodies, meaning that the absorptivity and emissivity are equal, and the reflectivity is therefore obtained by:

$$\alpha = \epsilon = 1 - \rho$$

The above equation is vital to understanding the relationship between the emissivity of a surface and its reflectivity. Materials that are 'highly reflective' will be defined by a reflectivity ρ close to 1 and therefore an emissivity ϵ close to 0. From the grey body heat rate equation, a highly reflective surface will therefore experience a small heat flux from its surroundings. Conversely, a dull, or very low reflective surface will experience a large heat flux from its surroundings due to an emissivity ϵ close to 1 (Bergman et al., 2011).

Including the factor of incident radiation upon a surface and the portion of radiation absorbed produces the grey body heat rate equation given by

$$q''_{rad} = \epsilon E_b(T_s) - \alpha G = \epsilon\sigma(T_s^4 - T_{sur}^4)$$

Where T_s represents the surface temperature and T_{sur} the surroundings temperature (Bergman et al., 2011).

1.1.2.2 External Thermal Loads on Spacecraft

Throughout a mission, a rocket will experience thermal loads from a variety of sources, both internal and external. These involve radiation from the sun and planets as well as internal heat generation respectively. Radiation is the only source from which a spacecraft can receive external heating in space because there is no medium through which heat can be conducted. The main radiation sources are the Sun and planets, which impart a heat flux on the exterior of the spacecraft, introducing thermal energy to the system (Ortega & Juan, 2017).

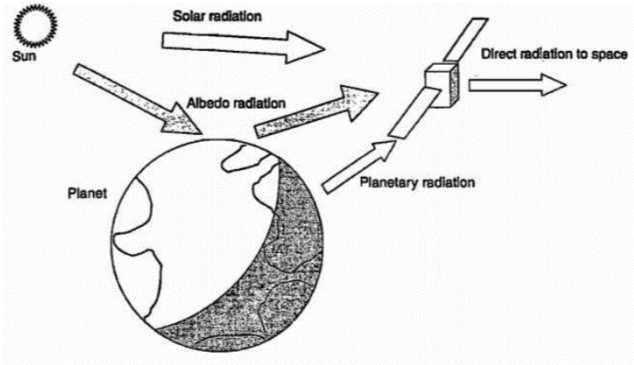

Figure 6: Sources of thermal energy in deep space on a spacecraft (Ortega & Juan, 2017)

Among these sources, the Sun produces the greatest thermal load on the spacecraft when it is within direct view of the spacecraft. The heat flux produced by the sun, S, is known to be approximately 1353 W/m^2 near Earth (Li & Junlan, 2013). Radiation from planets exists in multiple forms, these being albedo radiation and planetary radiation. The former is the phenomenon of the Sun's radiation reflecting or otherwise being re-emitted by planets. The latter mode is heat generated by a planet and radiated away to heat the spacecraft. Within the scope of this project, albedo and planetary radiation are ignored for simplicity, because they are insignificant compared to the flux imparted by the sun in this part of the solar system.

1.1.2.3 Internal Thermal Effects and Propellant Boil-Off

The thermal effects within cryogenic fuel tanks are the primary concern of the heat transfer analysis of this project and were key to the solutions later presented. Accurate and thorough research into the fundamentals of boil-off was crucial for gaining a strong understanding of the governing physics and making simplifying assumptions that were grounded and justifiable based on the conditions at play. Accurate modeling of cryogenic fluid boil-off is not new to the area of astronautical engineering but has not always been easily achieved. As discussed by Corpening, many models exist for calculating the fuel lost due to boil-off in launch vehicles, such as the models developed for the Saturn era missions, Ares missions, and the Space Shuttle. One specific example is the ROCETS model, which has the "major disadvantage of the inability, to date, to calculate mass transfer from evaporation, liquid bulk boiling, or condensation" (Corpening, 2010). The model developed by Corpening was designed to accurately consider the mass transfer at the surface layer in all three forms: evaporation, liquid bulk boiling, and condensation. This source is the primary reference for the model discussed below.

The previous sections define the external energy flux effects that the proposed spacecraft would experience on a given mission. A combination of radiation from the sun, albedo radiation from nearby bodies, and conductive heat transfer from structural components will induce a heat flux across the surface of the vehicle. Understanding the external effects is crucial to some material selections and optimization of the tank design. It is important to note that identifying what heat is imparted on the surface of the vehicle does not directly answer the question of what heat is imparted upon its stored fuel since only a portion of the energy flux will be transmitted. An arbitrary control volume pictured below in Figure 7 displays the various heat and mass transfer effects that must be considered when accurately modeling boil off. A list of variables and definitions is given in Table 2.

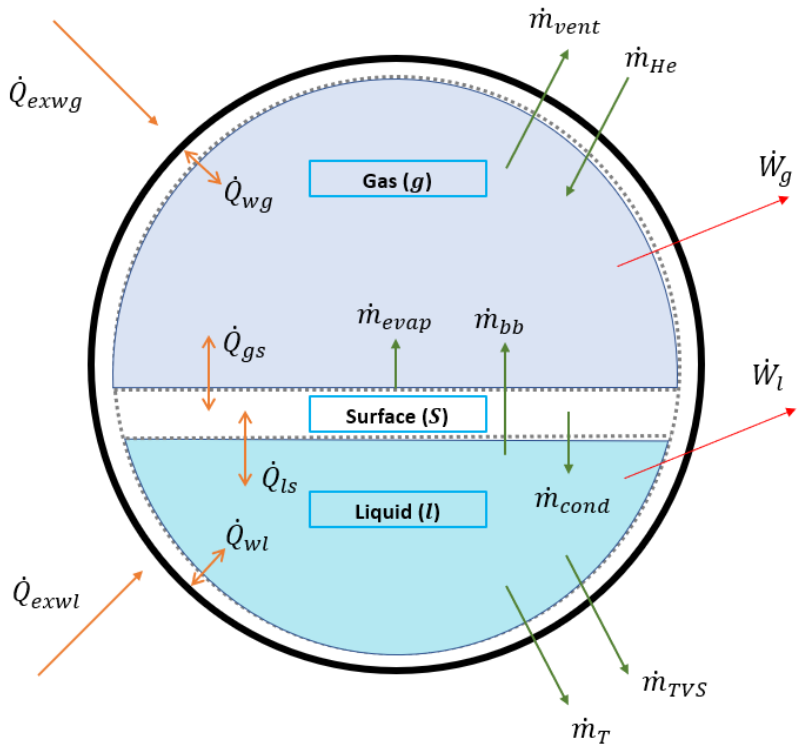

Figure 7: Internal model of cryogenic fuel storage tank

Table 2: Internal model of cryogenic fuel storage tank definition of variables

Variable	Units	Definition
$\dot{m}_{He}$	kg/s	Helium pressurization mass flow rate
$\dot{m}_{vent}$	kg/s	Vent relief mass flow rate
$\dot{m}_{evap}$	kg/s	Propellant evaporation mass flow rate
$\dot{m}_{bb}$	kg/s	Propellant bulk boiling mass flow rate
$\dot{m}_{cond}$	kg/s	Propellant vapor condensation mass flow rate
$\dot{m}_{TVS}$	kg/s	Propellant Thermodynamic Vent System (TVS) mass flow rate
$\dot{m}_T$	kg/s	Propellant liquid mass flow rate
$\dot{Q}_{exwl}$	W	Heat transfer rate from the external environment to tank skin exposed to liquid
$\dot{Q}_{exwg}$	W	Heat transfer rate from the external environment to tank skin exposed to gas
$\dot{Q}_{wl}$	W	Heat transfer rate between liquid node and tank wall exposed to liquid node
$\dot{Q}_{wg}$	W	Heat transfer rate between gas node and tank wall exposed to gas node
$\dot{Q}_{ls}$**	W	Heat transfer rate between liquid node and saturated surface layer node
$\dot{Q}_{gs}$**	W	Heat transfer rate between gas node and saturated surface later node
$\dot{W}_l$	W	Liquid node work rate

$\dot{W}_g$	W	Gaseous node work rate
P_g	MPa	Tank Pressure
T_g	K	Gas temperature
T_l	K	Liquid temperature
V_g	m^3	Gas volume
V_l	m^3	Liquid volume

**These variables are slightly misrepresentative of the fact that heat transfer across the surface node will occur only from either the gas node to the liquid node, or the liquid node to the gas node depending on the temperature gradient. The surface node is infinitely thin and therefore does not hold any thermal energy itself. While this is a fundamental understanding of heat transfer, the equilibrium equations used in Corpening require the extended form of the variables shown above.

Heat Transfer

For accurate fluid boil-off calculations, multiple sources, and modes of heat transfer into the fluid must be considered. The overall source of heat transfer on to the tank is through radiation, but this value may not be uniform across the entire external surface of the tank. $\dot{Q}_{exwl}$ *and* $\dot{Q}_{exwg}$ denote the heat transfer rate from the external environment to the tank skin exposed to the liquid node and gaseous node respectively. These values represent an average over the associated skin surface area, but another level of detail could be introduced by considering how uniform the distribution of $\dot{Q}_{exwl}$ *and* $\dot{Q}_{exwg}$ individually are. As mentioned in section 1.1.2.2, a variation in heat flux on to the skin could be present due to a 'light' side and a 'dark' side of the spacecraft, albedo radiation, or conduction from supporting structures.

Moving inward through the tank wall, heat transfer into the fluid and gaseous phase are individually considered as $\dot{Q}_{wl}$ and $\dot{Q}_{wg}$ respectively. A factor not pictured in Figure 7 but important to consider is that the flux through the tank wall is dependent on the conditions on the inside of the tank. For the liquid phase, the temperature of the fluid may rise until it reaches its boiling temperature (dependent upon its vapor pressure). Once the fluid reaches its boiling temperature it will be unable to continue to rise in temperature. Therefore, a constant temperature boundary condition at the inner layer of the tank wall is apt. The flux through this portion of the tank wall will continue to rise with time until steady state between the outer and inner surface is reached. In opposition, the temperature of the gaseous phase will continue to rise as energy is imparted upon the spacecraft, so the flux through the tank wall will vary with the internal gas temperature. This heat transfer across the tank wall occurs due to convection.

Furthermore, the heat transfer that occurs at both the inner wall of the liquid phase and gaseous phase is directed by convective heat transfer, modeled by the equation listed in section 1.1.2.1. Both fluids will have some degree of convective flow occurring, generating a velocity field that will affect how energy is transferred in to and through the liquid. At the liquid – wall contact layer, gaseous bubbles will form as boiling occurs, generating flow into the gaseous phase. When the assumption that the liquid node is uniform in temperature is applied, flow does not affect heat transfer within the liquid, but it will affect the motion of the bubbles. This multiphase flow can be modeled by computational tools such as multiphase turbulent flow with assumptions made to the velocity field conditions. These dynamic effects are neglected in the current study.

Lastly, heat transfer across the surface layer, s, must be considered from both the liquid phase and gaseous phase, denoted by $\dot{Q}_{ls}$ and $\dot{Q}_{gs}$ respectively. This layer node is an infinitely thin layer of propellant which allows for the heat transfer to occur between the two bounding phases. Like the heat transfer into the liquid and gaseous nodes from the tank internal wall, the heat transfer across the surface, s, to the liquid and gas occurs due to convective heat transfer. Therefore, heat transfer within the fluid tank occurs across 4 different mediums: flux applied to the external skin of the tank, flux through the tank wall, flux from the tank wall into the liquid and gaseous nodes, and flux across the saturated liquid-gas surface into or out of the liquid and gaseous nodes (Corpening, 2010).

Mass Transfer

Mass transfer within the tank can occur in four different mechanisms: evaporation from the saturated surface layer, liquid bulk boiling, propellant vapor condensation, and deliberate exhaustion of mass (Corpening, 2010). The first three mechanisms of mass transfer are strictly dependent upon conditions within the tank.

Deliberate exhaustion of mass from the tank is a strategy used to maintain pressure in the tank, and to use for generating thrust. Specific requirements of a propellant and the propellant tank are defined by given mission parameters and will vary between different mission types. Generally, though, the propellant will be removed from the tank and directed to the thruster(s) for the completion of a ΔV burn at a rate of $\dot{m}_T$. Other accessory burns and thrusts may occur, such as a thermodynamic venting system (TVS) burn designed to keep the fluid within the tank

at desired thermodynamic conditions, designated by $\dot{m}_{TVS}$. The use of a TVS in a mission design is explained further in 1.1.3.4. Perhaps most important to a cryogenic fuel storage tank is the release of mass in the gaseous phase to maintain desired safety or thermodynamic conditions. Release of gas by the venting system, $\dot{m}_{vent}$, is modeled based on the nature of the release vent. As will be later discussed in section 1.1.3.3, this mass can be utilized by ullage thruster systems to perform attitude correction maneuvers to a spacecraft or be jettisoned out into space. This release of mass may be paired with the flow of additional ullage gas into the tank volume at a rate of $\dot{m}_{He}$, again to maintain ideal conditions. These factors are mission dependent and can easily be simplified for the purpose of a refined boil-off specific model.

Mass transfer due to condensation and evaporation at the surface layer is dependent upon the temperature of the gas and fluid. Propellant vapor condensation from the gas to liquid phase can only occur if the tank gas temperature drops below the gaseous propellant vapor saturation temperature. Furthermore, this means that the saturation pressure of the gaseous phase, P_{vlc}, which is dependent upon its temperature, drops below its partial pressure, P_{vl}. This will occur when the internal pressure of the tank increases or decreases as ullage gas is added or removed from the system, or when a ΔV burn is performed, rapidly increasing the volume of the gas in the tank. On the other hand, evaporation of liquid propellant into gaseous propellant occurs when the heat transfer rate from the gas to liquid exceeds the heat transfer from the liquid to the gas, netting in an overall heat flux into the liquid from the gas.

Lastly, is the loss of mass due to bulk liquid boiling. When the tank pressure, P_g, drops below the liquid vapor pressure, P_{vl}, liquid bulk boiling will occur. As noted by Ring, "if the total pressure of the tank gas drops to the vapor pressure of the bulk liquid, bulk boiling of the liquid will occur. The rate of boiling is that sufficient to maintain the tank gas pressure equal to the tank liquid vapor pressure" when venting is occurring (Ring, 1964). The process of bulk boiling is complex and difficult to model, however Corpening offers a simplified form of the bulk boiling equation based on the simplifications offered by Ring. Therefore, in a high-fidelity model, the overall mass that will be lost to boil-off is the sum of the mass transfer from condensation, evaporation, and bulk boiling (Corpening, 2010).

While the above discussion by Corpening on the modeling an accurate boil-off model is valid the contect of the researchers proposed problem, a broader approach is required by the nature of this paper. The conditions of bulk boiling, condensation, and evaporation also do not

consider the presence of liquid-gas phase change occuring at the wall-liquid contact area. In a traditional boiling problem, such as a boiling pot of water, the primary driver of mass release from liquid to gas is the formation of bubbles at the wall that are released from the liquid. The Using the model discussed by Corpening as a reference, a broader approximation of the rate of fluid boil off is required. This simplification is outlined in the simplfied form of the boil off model in 2.3.2.2.

1.1.3 Propellant Boil-Off Management Methods

Despite their performance, cryogenic propellants are difficult to handle and store due to heat transfer from the ambient surroundings that drive boil-off. Therefore, launch vehicle stages using cryogenic propellants are generally jettisoned within hours or even minutes after launch. For missions to the Moon and back, spacecraft are subjected to a week-long round trip before returning to Earth, so cryogenic propellants are not often used for the entirety of these missions. After separation from the launch vehicle, most spacecraft (e.g., satellites, probes, and manned capsules) use EP or propellants that remain liquid at room temperature, often hydrazine fuel and nitrogen tetroxide oxidizer (Wertz et al., 2011). Cryogenic stages used for lunar missions have historically been expended after completing a translunar injection burn, which places a spacecraft into an eccentric Earth orbit designed to intercept the Moon's sphere of influence. For example, the crewed Apollo Command and Service Module used non-cryogenic propellants while traveling to the moon and for entering lunar orbit after launch via the Saturn V rocket, which used cryogenic propellant (Biesbroek & Janin, 2000). Since the duration for which cryogenics are used is relatively short (one or two days at most) boil-off rates are managed through active and passive cooling methods. Active cooling continually measures and regulates cryogenic tank properties, and passive cooling methods such as thermal insulation or spacecraft rotation do not continuously measure and regulate cryogenic tank properties. Space systems also use gaseous propellant venting to avoid over-pressurization (Barsi, 2011).

The use of cryogenic propellant in spacecraft will be necessary for missions requiring high thrust and efficiency, so scientists and engineers are developing active methods such as zero boil-off for future exploration. According to NASA, "the storage of cryogenic propellants will be critical to future, long-term human exploration missions beyond low-Earth orbit."

1.1.3.1 Insulation

As detailed in section 1.1.2.2, the primary source of heat transfer onto a spacecraft is radiation from the sun, so spacecraft employ multi-layered insulation (MLI) blankets to reflect this thermal energy (Stefansson, 2014). Figure 8 shows the Hubble Space telescope wrapped in MLI with an outer cover of aluminized Teflon.

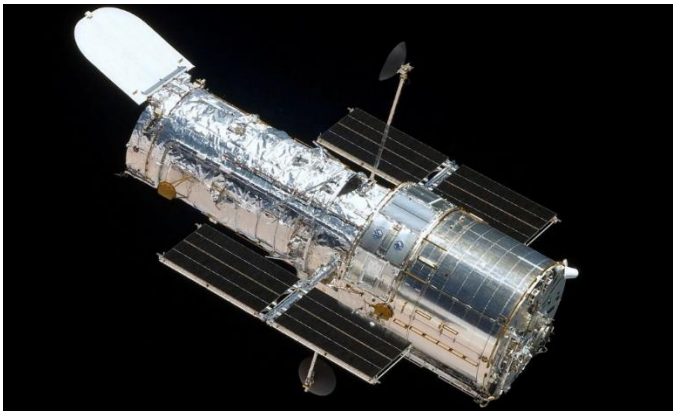

Figure 8: Hubble Space Telescope covered in MLI with an aluminized Teflon outer layer (Wittry, 2009)

MLI blankets consist of highly reflective materials with insulating layers stacked between them to prevent conduction between each reflective sheet. Reflector layers are commonly polymers like Mylar or Kapton, with a reflective coating of aluminum, gold, or copper. These layers have low emissivity and thermal conductivity, providing a shield against solar or other radiation in space.

Table 3: Thermal and material properties of commonly used reflector layers (Finckenor & Dooling, 1999)

Material	Aluminized Kapton	Goldized Kapton	Aluminized Mylar	Polyester	Teflon
Specification	MDAC-STM0691, Type II, Class 1, Grade A	Rockwell MB0135-038, Type II, Class 1, Grade A	MDAC STM0691, Type II, Class 1, Grade A	–	–
Description	Single or double aluminized	Single or double goldized	Double aluminized	Single or double aluminized	Single or double aluminized
Vendors	Sheldahl, Dunmore	Sheldahl	Sheldahl, Dunmore	Sheldahl, Dunmore	Sheldahl, Dunmore
Thickness, mm (mil) metal, Å	0.0076–0.127 (0.3–5.0) 1,000	0.0076–0.127 (0.3–5.0) 750	0.0051–0.127 (0.2–5) 1,000	0.00006–0.0013 (0.25–5); 300	0.00003–0.0013 (0.1–5); 300
Weight, gm/cm^2 (oz/yd^2) 0.0051 mm (0.2 mil) 0.0064 mm (0.25 mil) 0.0076 mm (0.3 mil) 0.013 mm (0.5 mil) 0.025 mm (1.0 mil) 0.051 mm (2.0 mil) 0.076 mm (3.0 mil) 0.127 mm (5.0 mil)	 0.0011 (0.020) 0.0019 (0.034) 0.0036 (0.066) 0.0071 (0.131) 0.011 (0.20) 0.019 (0.34)	 0.0011 (0.020) 0.0019 (0.034) 0.0036 (0.066) 0.0071 (0.131) 0.011 (0.20) 0.019 (0.34)	 0.0007 (0.013) 0.00093 (0.017) 0.0017 (0.031) 0.0033 (0.060) 0.0066 (0.12) 0.0104 (0.19) 0.0175 (0.32)	–	–
Temperature, °C (°F) Continuous, max/min Intermittent, max/min	 –250/+288 (–420/ 550) –250/+400 (–420/750)	 –250/288(–420/550) –420/750 (–250/400)	 –250/93 (–420/200)[1] –250/150 (–420/300)	260 (500)	260 (500)
Absorptance, a (max/typ)	0.14; 0.12	0.30; 0.28	0.14; 0.12	<0.14	<0.14
Infrared emittance, e	0.05; 0.03 [2]	0.04; 0.02 [2]	0.05; 0.03 [3]	<0.04	<0.04

The separator layers consist of light, easy to handle, meshed plastic fabric such as Dacron or Nomex, which are made from polyester (Stefansson, 2014). This acts to physically separate reflector layers by limiting contact area, thereby preventing conduction between the metallized reflector layers. Conduction between layers is the most significant form of thermal energy transfer through the MLI, so limiting this is important to creating an effective MLI blanket.

Table 4: Thermal and material properties of separator materials (Finckenor & Dooling, 1999)

Material	Dacron Netting	Nomex Netting
Specification	Rockwell MB0135–042, MDAC–STM0605–03	
Description	100% polyester fabric mesh[1]	100% Nomex aramid fabric mesh[2]
Vendors	Apex Mills	Stern & Stern Textiles, J.P. Stevens
Thickness, mm (in.)	0.16 ± 0.01 (0.0065 in.±0.0005)	0.16 ± 0.01 (0.0065 in.±0.0005)
Construction Meshes/cm^2 (in.^{2}) Denier filaments	7.8±1.2 (50 ± 8) 40	7.9±1.2 (51±8) 40
Weight, gm/m^2 (oz/yd^2)	6.3 ± 0.85 (0.185 ±0.025)	6.3 ± 0.85 (0.185±0.025)
Burst strength, kg/cm (lb/in.)	5.625 (10)	5.625 (10)
Temperature range continuous, °C (°F)	−70 +120 (−94 +250) continuous −70 +177 (−94 +350) intermittent	−70 +120 (−94 +250) continuous −70 +177 (−94 +350) intermittent

Radiation that penetrates the upper layers can be reflected by subsequent layers as shown in Figure 9, so, with more layers, less radiation penetrates the MLI to impact the internal components of the spacecraft. However, increasing the number of layers of MLI has diminishing returns as the total heat energy available to reflect drops off. Between 10 and 30 layers of reflective sheets are often utilized for a single MLI blanket, and they are often between 10 and 25 mm thick (Concept Group, 2019). In determining the effectiveness of a material in an MLI blanket, one must consider its emissivity and thermal conductivity, among other factors. Mylar is a common choice for an MLI reflector, with an emissivity value of 0.044 and a thermal conductivity of 0.155 W/mK at room temperature (Domen, 1991; Rule, 1996). However, it is important to consider the environment in which the MLI will be working. In operation, the temperature of the tank will be near 20K (the boiling temperature of Hydrogen), significantly colder than room temperature, meaning the properties of the materials will be different. In these conditions, aluminized Mylar has emissivity and thermal conductivity values of 0.0002 and

0.044 W/mK respectively (Heaney, 1998; Rule, 1996). One of the other most important factors for the efficacy of MLI is the spacer material. This is a low conductivity material that goes between the reflector layers to separate them and form a more effective insulation. This role is often filled by materials like Dacron mesh or other forms of netting because this limits the contact area with the Mylar, in turn limiting thermal conduction through the blanket. Dacron netting has a thermal conductivity value of 0.09108 W/mK at the boiling temperature of Hydrogen (Ross, 2015). MLI are most often used after a spacecraft has exited the Earth's atmosphere, because despite their thermal resistance capabilities they are very delicate and are designed to prevent heat transfer due to radiation as opposed to conduction. This is accomplished by encasing the upper stage modules in the MLI, so they are only exposed once the lower stages and outer shells are discarded. Once in low Earth orbit (LEO), reflector materials are subject to atomic oxygen erosion and micrometeoroid bombardment, which can penetrate and damage the MLI. This is why outer covers of Teflon or Beta Cloth are often used to protect the MLI (Finckenor & Dooling, 1999; Groh & Banks, 1994).

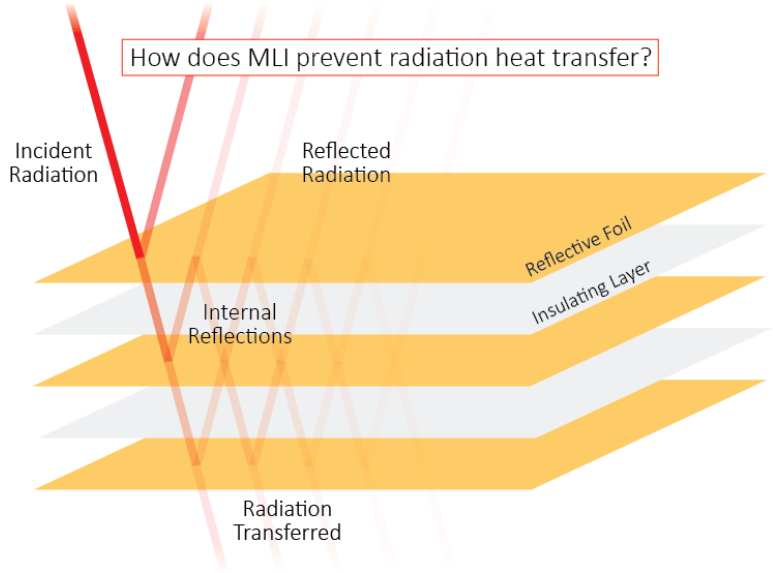

Figure 9: Diagram of the function of multiple layers of reflective and insulating material in a MLI blanket (Concept Group, 2019)

During the launch phase of a mission, heat transfer into cryogenic propellants due to drag and conduction from the atmosphere must be mitigated to avoid boil-off and over pressurization

(Harbaugh, 2022). Therefore, organizations including NASA and United Launch Alliance (ULA) use spray-on polyurethane-based foam to insulate their launch vehicle's cryogenic propellant tanks (Mohon, 2015). This orange insulating foam can be seen on the Delta IV Heavy rocket in Figure 10. Foam is used due to its high thermal resistance, which means it is highly capable of preventing thermal energy from entering the cryogenic tank (Harbaugh, 2022) Foam insulation is not used once the spacecraft has exited the atmosphere because its thermal resistance is largely resultant of its large air capacity, which is evacuated in the extreme low-pressure environments of the upper atmosphere and deep space (Jianpeng, n.d.). Therefore, rocket stages using foam insulation are jettisoned before the spacecraft leaves the atmosphere.

Figure 10: The entirely LH_2 fueled Delta IV Heavy rocket preparing for launch; exhibiting orange foam insulation (Erwin, 2019)

1.1.3.2 Radiative Cooling of Rotating Spacecraft

Fundamentally, the concept of a spinning spacecraft is not new to astronautical engineering and has been employed in the past for different reasons. Depending on the mission design, different benefits arise when a spacecraft is spinning in a controlled manner. For example, a spacecraft with a controlled spin about a specific axis will introduce a gyroscopic stabilizing effect. This would be valuable for missions such as a deep-space vehicle designed to collect and transmit data at very specific attitudes. Alternatively, a spacecraft spinning at a high rate would introduce an internal centripetal acceleration force which could be important for the proper flow of fuel to a thruster system depending on its design.

Including a slow controlled rotation to a spacecraft takes advantage of the phenomenon of radiative cooling. This method is known as Passive Thermal Control (PTC) and has been used in multiple missions, most notably the Apollo missions. As explained by Atkinson, the goal of this technique, coined *Barbecue Mode*, was "to spin the spacecraft … on its long axis at one to three revolutions per hour to even out solar heating" (Atkinson, 2020). Section 1.1.2.1 explains the principle of heat transfer through radiation and applying that knowledge to this scenario it is easy to identify the benefits of rotating a spacecraft. The radiative power a surface emits is proportional to its temperature and the temperature of its surroundings. By rotating the spacecraft at a controlled rate, the portion of the spacecraft that was in direct contact with the sun is then moved away, allowing it to re-radiate its energy out to space and cool off. Simultaneously, the opposing side is heating up. The cycle continues as any point on the spacecraft will alternate between heating up and cooling. Applying this to the proposed cryogenic tank design, rotating this vehicle will lower the total solar flux that is imparted on the fluid and therefore lower the magnitude of boil-off.

1.1.3.3 Venting Techniques

Venting is a widely used strategy to manage boil-off which involves opening and closing valves to release some of the boiled off gas into space. This process causes a loss of the overall propellant in the tanks and therefore must be factored into the total amount of propellant required for the mission. Despite the need for additional propellant, venting is still a lightweight and simple method for managing boil-off, and when combined with insulation and other boil off

mitigation techniques, it can provide a safe and effective method to combat boil-off (Neher, 1971).

There are various styles of venting. The cyclic vent system used on the Centaur Upper Stage of the Titan rocket uses solenoid locking valves, with two on the LH_2 tank and one on the LOx tank (Rudman & Austad, 2002). During a coast period, these valves remain closed unless the pressure reaches a point where venting is needed. At this point, the valves will stay open until the tank reaches the designed pressure and they are closed again. The downside to this system is that there is no thrust during the coast period. This prevents the liquid propellant from settling at the bottom and bubbles of gaseous propellant can form throughout the tank. During venting, auxiliary thrusters must be used to prevent liquid propellant from being vented. This adds weight to the system and complexity to the design. Additionally, cyclic venting causes a larger area of the tank walls to become wet. Heat transfer into the tank occurs through the tank walls, so a larger wet area causes increased boil-off (Neher, 1971).

Another system is the Thermodynamic Vent System (TVS) with a cooling shroud. The system only involves venting the LH_2 tank and not the LOx tank. Instead, the vented gas from the LH_2 tank is passed through a cooling shroud around the LOx tank. Due to the lower boiling point of LH_2, the gaseous hydrogen keeps the LOx below its boiling point (Burge & Blackmon, 1972). This system has the same disadvantages as the previous system, with auxiliary thrusters needed to vent and a larger surface area of the tanks becoming wet. However, with the LOx tank not needed to be vented, less LOx needs to be carried resulting in weight reduction.

The last system is the continuous venting system (CVS) on the Saturn S-IVB. The main venting system aboard this vehicle is a fixed size orifice that vents gaseous propellant continuously during the coast period. There is a secondary non-propulsive valve (NPV) to provide extra venting should the system experience unexpected heat. The vented gas from the CVS is routed through a wrap-around duct system where it exits through nozzles parallel to the spacecraft's direction, as shown in Figure 11. This provides continuous thrust during the coast period, keeping the propellant settled at the bottom of the tank. The thrust provided is minimal since the area of the orifice is small, however it is effective in reducing boil off due to a smaller wet wall area (Neher, 1971).

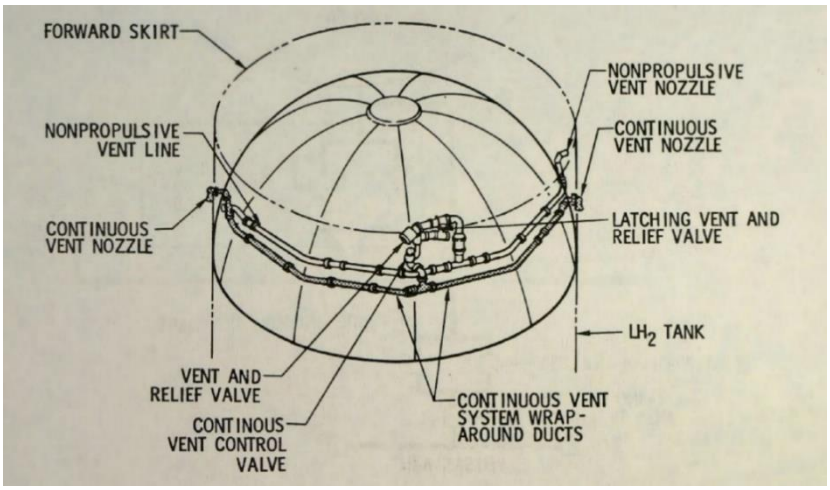

Figure 11: Diagram of the wrap around duct system on the Saturn S-IVB (Neher, 1971)

1.1.3.4 Active Methods of Boil-off Prevention

Active boil-off prevention strategies continuously respond to tank temperature and pressure to mitigate boil off or avoid it entirely.

Mixing is a method of controlling pressure which promotes condensation of vaporized propellant by bringing subcooled settled fluid to the liquid-vapor interface in a cryogenic tank. For a cryogenic tank on the surface of a planet, or under constant acceleration (due to the use of a CVS for example), higher density subcooled liquid will settle, and lower density, warmer liquid and vapor will rise to the top of the tank as heat is introduced to the system. Once the pressure begins to rise higher than the design conditions mixing will be initiated in an active system. Mixing settled liquid towards the warmer vapor layer can cause the vapor to condense. Mixing strategies include axial or radial liquid jets and spray bars which intake propellant and spray it back into the tank. Figure 12 shows a liquid-vapor interface in a cryogenic tank and a mixing jet. Despite its effectiveness in actively preventing boil-off, mixing is only a temporary solution because it adds kinetic energy to the system which will eventually cause the temperature to rise and result in further boil-off. For this reason, mixing is used for short duration missions or used in combination with refrigeration (Barsi, 2011). For relatively short missions “lasting from a few days to weeks, depending on the insulation performance and the degree of bulk liquid subcooling [below the boiling point of the fluid before launch], tank mixing may be sufficient to control the tank pressure with no propellant loss” (Hastings, 2003). Therefore, with effective MLI and subcooling, mixing is effective for relatively short missions.

Furthermore, TVS systems pump propellant into a heat exchanger to cool, then mix it back into the tank through a jet or spray. TVS heat exchangers pump sacrificial propellant out of the tank and expand the fluid through a valve to cool through the Joule-Thomson effect, where a fluid decreases in temperature as it expands. The expanded propellant is used to cool the cryogenic propellant pumped into the heat exchanger from the tank and is eventually vented. This allows thermal energy to be transferred to the lower temperature, expanded fluid which is then removed through venting as shown in Figure 12. Mixing or venting alone do not use heat exchangers to efficiently remove energy from the tank, so TVS designs yield greater control of tank temperatures and pressures (Hastings, 2003) . NASA and Rockwell Aerospace have extensively tested TVS designs that were capable of successfully controlling pressure within necessary tolerances for various mission scenarios (Barsi, 2011).

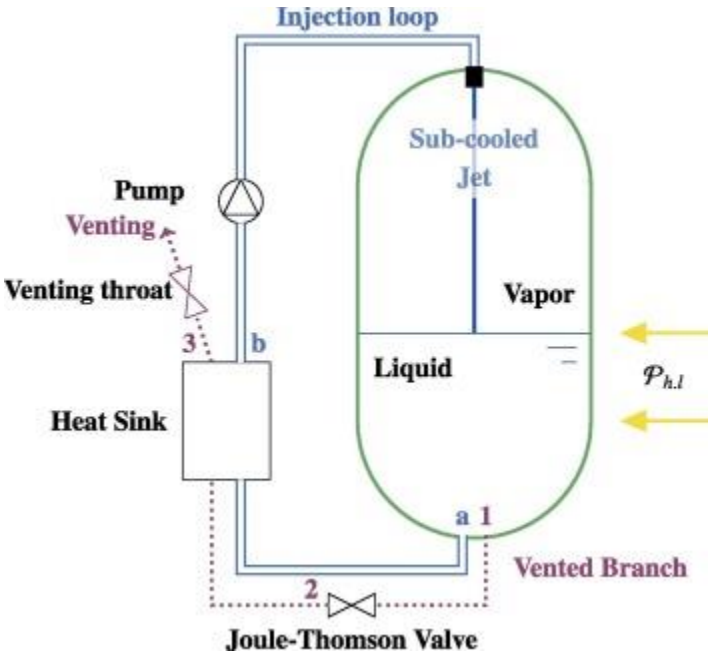

Figure 12: Schematic of a TVS system (Mer et al., 2016)

Cryogenic propellants are promising for future missions because of their high thrust, efficiency, and potential to be synthesized on the Moon or Mars using natural water-ice or carbon dioxide supplies. For interplanetary missions or orbiting propellant depots, cryogenic propellant will need to be stored for months or years (NASA, n.d.). Therefore, researchers are pursuing zero boil-off systems. These systems avoid venting completely using cryocoolers, often

combined with mixing via jets or spray bars. An example of a cryocooler and its power system components is shown in Figure 13. This system uses liquid helium which has a boiling point of 4.2 Kelvin (Britannica, 2022).

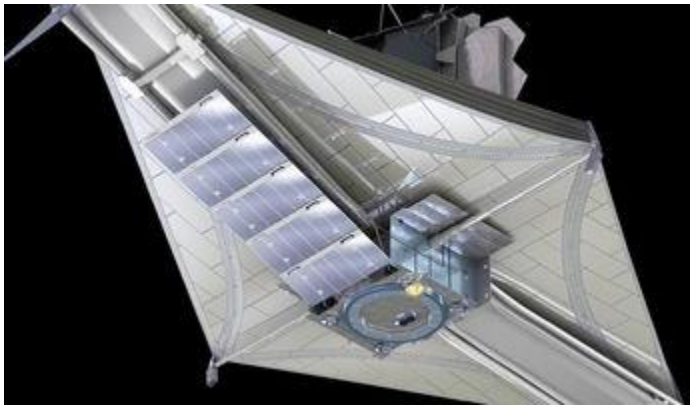

Figure 13: James Webb Space Telescope sun facing side (NASA Goddard Space Flight Center, 2022)

Although cryocoolers add mass, complexity, and electrical power requirements to spacecraft, zero boil-off systems can be worth pursuing due to the saved propellant mass that would otherwise be vented for long duration missions. Analysis shows that zero boil-off methods will result in cost-benefits for mission durations of one week for those using liquid oxygen, two weeks for liquid methane, and two months for liquid hydrogen. Further research is required to optimize zero boil-off strategies by minimizing mass and power costs and to gain a "better understanding of the complicated and coupled transport phenomena inside the tank which can affect thermal stratification, self-pressurization, and pressure control" (Boen, 2013).

1.1.4 Cryogenic Propellant Storage Tank Design

As discussed in the introduction, active and passive methods to mitigate boil-off are not enough to solve this problem on its own. Instead, cryogenic tanks themselves must be designed to reduce the rate of heat transfer into the propellant. This section details how the geometry and material of cryogenic tanks can be selected and designed to minimize the rate of heat transfer into the tanks.

1.1.4.1 Tank Geometry

Propellant tank geometry is constrained by structural considerations, weight, and boil-off minimizations. Spherical tanks are the best shape for meeting these requirements, as spheres have the smallest surface-to-volume ratio among common shapes. As a result, there is less surface area per unit volume that heat can transfer through, slowing down boil-off. However, spheres are difficult to incorporate into the aerodynamic profile of a rocket, which is important in the launch phase of a mission where aerodynamic forces are present. This is why many rocket propellant tanks are capsule-shaped. However, depending on the mission requirements, spherical tanks can be small enough to fit into commercially available launch vehicles (Wertz et al., 2011).

The size, i.e., surface area, volume, mass, and thickness of cryogenic tanks can be determined from geometry. For a capsule-shaped tank (a cylinder with a hemisphere on each end) the surface area, volume, and mass are respectively defined as

$$SA_{capsule} = 2\pi r(2r + h) \tag{2}$$

$$V_{capsule} = \pi r^2 \left(\frac{4}{3}r + h\right) \tag{3}$$

$$M_{capsule} = \rho(A_c t_c + A_s t_s) * PMD \tag{4}$$

where r and h are the inner radius and height of the capsule, respectively, ρ is the density of the tank material, A_c is the surface area of the cylindrical section, A_s is the surface area of the spherical section, and PMD is a factor (generally between 1.2-1.3) that accounts for the propellant management devices (Wertz et al., 2011) .The thickness of the cylindrical and spherical sections, t_c and t_s, respectively, are defined as

$$t_c = SF\left(\frac{pr_{cylinder}}{\sigma_{ult}}\right) \tag{5}$$

$$t_s = SF\left(\frac{pr_{sphere}}{\sigma_{ult}}\right) \tag{6}$$

where p is the operating pressure of the tank, r is the inner radius of the cylindrical or spherical section, σ_{ult} is the ultimate strength of the tank material, and SF is a safety factor. Similarly, for a spherical-shaped tank, the surface area, volume, and mass are defined as

$$V_{sphere} = \frac{4}{3}\pi r^3 \tag{7}$$

$$SA_{sphere} = 4\pi r^2 \tag{8}$$

$$M_{sphere} = \rho A_s t_s * PMD \tag{9}$$

where r is the inner radius of the sphere, A_s is the surface area of the sphere, and t_s is the thickness of the sphere, as defined in equation (6). The inner radius and height of each tank, which are needed to size the tank, are unknown. However, the required volume of each tank can be determined from given mission requirements. Therefore, for the capsule-shaped tank, equations (2) and (3) can be solved numerically using the required tank volume to find an inner radius and height that minimize the surface area of the tank, and therefore area for heat to propagate through and contribute to boil-off. Conversely, the dimensions of a spherical tank can be determined with simple arithmetic. From equation (7), the inner radius of the tank can be calculated as

$$r_{sphere} = \sqrt[3]{\frac{3V_{sphere}}{4\pi}} \tag{10}$$

Where, by assuming the volume of the sphere is equivalent to the propellant volume, the volume of the sphere can be calculated as

$$V_{sphere} = V_{prop} = \frac{m_{prop}}{\rho_{prop}} \tag{11}$$

where ρ_{prop} is the density of the propellant (a known value) and m_{prop} is the mass of the propellant. The propellant mass can be calculated from the oxidizer-to-fuel mixture ratio of the thruster used on the spacecraft and the Rocket Equation. The Rocket Equation is derived from Newton's second law for an accelerating rocket and relates the change in velocity of a rocket (ΔV) to its initial, total fueled (wet) mass (m_i), its final, total unfueled (dry) mass (m_f), and specific impulse (I_{sp}) of the thruster, i.e., LH_2 plus LOx, used on the spacecraft as

$$\Delta V = -cln\left(\frac{m_f}{m_i}\right) \tag{12}$$

or

$$\frac{m_f}{m_i} = e^{-\frac{\Delta V}{c}} \tag{13}$$

where

$$c = (I_{sp})(g) \tag{14}$$

Where g is the acceleration due to gravity. ΔV can be determined using parameters from the desired mission profile, e.g., launching to the Moon, via software such as Ansys' Systems Tool Kit (STK). Furthermore, the total mass of the propellant can be defined as the difference between the wet and dry mass of the rocket, i.e.,

$$m_{prop_{total}} = (m_i - m_f) * CF \tag{15}$$

Where *CF* is a contingency factor. This factor varies based on the mission, but a 10%-20% margin is a typical value (Wertz et al., 2011). The final mass can then be solved from equation (12), given an initial guess for the wet mass. Therefore, using the total propellant mass and the mixture ratio of the thruster (i.e., the mass ratio of oxidizer that is required to mix with one part fuel in the thruster's combustion chamber), the mass of the fuel can be calculated as

$$m_{prop_{fuel}} = \frac{m_{prop_{total}}}{mixture\ ratio + 1} \tag{16}$$

And the mass of the oxidizer is

$$m_{prop_{oxidizer}} = \left(m_{prop_{fuel}}\right)(mixture\ ratio) \tag{17}$$

Which, by equations (11), (10), (8), (6), and (9) and from the material properties of the tank material, yield the volume, inner radius, surface area, thickness, and mass of the cryogenic fuel and oxidizer tanks, respectively.

1.1.4.2 Tank Material

Aluminum alloys (AA) are some of the most common metallic materials used in the construction of cryogenic propellant tanks. However, a major drawback of metallic tanks is their weight. NASA spends more than $10,000 to send one pound of payload into space (Dunbar, 2008), and current metallic cryogenic tanks account for approximately 70% of the solid mass of launch vehicles (Birkland et al., 2017)! With new and highly demanding space launch vehicles

requiring most of the rocket's mass to be propellant to meet mission requirements, engineers are challenged with designing and implementing lightweight materials for cryogenic tanks.

To overcome this challenge, engineers have been researching and testing the use of composite materials in the construction of cryogenic tanks. Composite materials consist of two or more materials with different chemical and physical properties that are combined in order to achieve certain desired characteristics. Compared to metallic alloys, composites are stronger, lighter, and have lower thermal conductivities, making them more thermally efficient. The strength of composites is due to their high tensile and yield strengths, which makes them less likely to fail under tensile loads and permanently deform, respectively.

The decreased weight of composites is due to their density, which is lower than that of metallic materials and allows for less material to be used in the design of cryogenic tanks, for a given tank volume. Finally, the increased thermal efficiency of composites is a result of their low thermal conductivity, which is a measure of a material's ability to transfer heat via conduction. In the case of propellant tanks, a lower thermal conductivity means less heat is being transferred through the wall of the tank and to the propellant, resulting in a smaller temperature gradient and therefore boil-off rate (Arnold et al., 2007). Mechanical properties of IM7 carbon fiber and S2-Glass composite materials are compared to AA 2024, a common AA typically used in aerospace applications, in Table 5 to illustrate the advantages of using composites over metallic alloys (Prasad & Wanhill, 2017); (S-2 Glass Fiber, n.d.); (Hexcel, 2020); (Hexcel HexTow IM7 Carbon Fiber - Epoxy Composite, n.d.).

Table 5: Comparison of mechanical properties for example composite and metallic materials

	Material		
Property	AA 2024	IM7 Carbon Fiber	S2-Glass
Density (g/cm^3)	2.77	1.78	2.46
Tensile Strength (MPa)	470	5688	4890
Yield Strength (MPa)	325	2760	N/A*
Thermal Conductivity (W/m K)	180	5.40	1.45

*S2-Glass does not have a yield strength as it does not exhibit elastic behavior.

One of the most popular composite materials is carbon fiber reinforced polymers (CFRP), a carbon fiber matrix held together by a polymer binding. CFRPs have been extensively researched and have been implemented into various aerospace applications such as automobiles, aircraft, and cryogenic tanks. A CFRP composed of 30% epoxy resin and 70% carbon fiber would have a density of 1.55 g/cm^3. When comparing this value to aluminum (2.7g/cm^3), titanium (4.5 g/cm^3) and steel (7.9 g/cm^3), it can be shown that the density of the CFRP is almost two times smaller than aluminum and more than five times smaller than steel. Additionally, when comparing a composite plate to an aluminum plate, the composite plate will be 31% more rigid, weigh 42% less, and have 60% more strength (Dexcraft, 2015).

The largest issue facing composite materials, specifically CFRPs, is leakage. Since the molecules in cryogenic propellants, namely LH_2, are so small, they can leak out of the tank, either by diffusion through voids in the material, or through microcracks formed by external forces. Leakage due to microcracks is the main form of leakage, however, it can be mitigated with advanced molding techniques, toughening of the carbon fiber layers, and toughening of the resin matrix present in CFRPs. These measures reduce brittleness (which is especially important at cryogenic temperatures), increase fracture toughness, and decrease the density of microcracks (Liu et al., 2021).

1.1.4.3 Unidirectional vs Woven Composites

The fiber matrix layup comes in two forms: unidirectional or woven fibers. Unidirectional fibers refer to all lamina fibers running parallel to each other, which is illustrated in Figure 14. Woven fibers have fibers interlocking with each other in at least two directions, typically 0° and 90°; Figure 15 depicts various style weaves that can be used, common ones being plain, 5 harness satin, and 8 harness satin weaves.

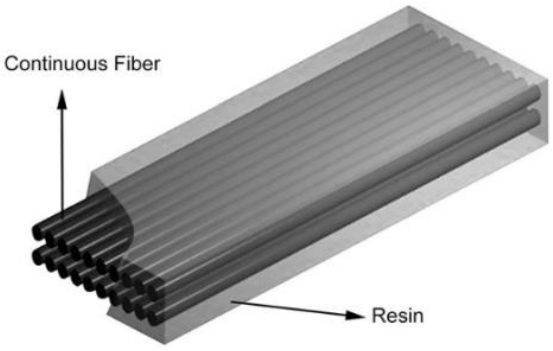

Figure 14: Illustration of unidirectional fiber matrix in resin (TOPOLOCFRT, n.d.)

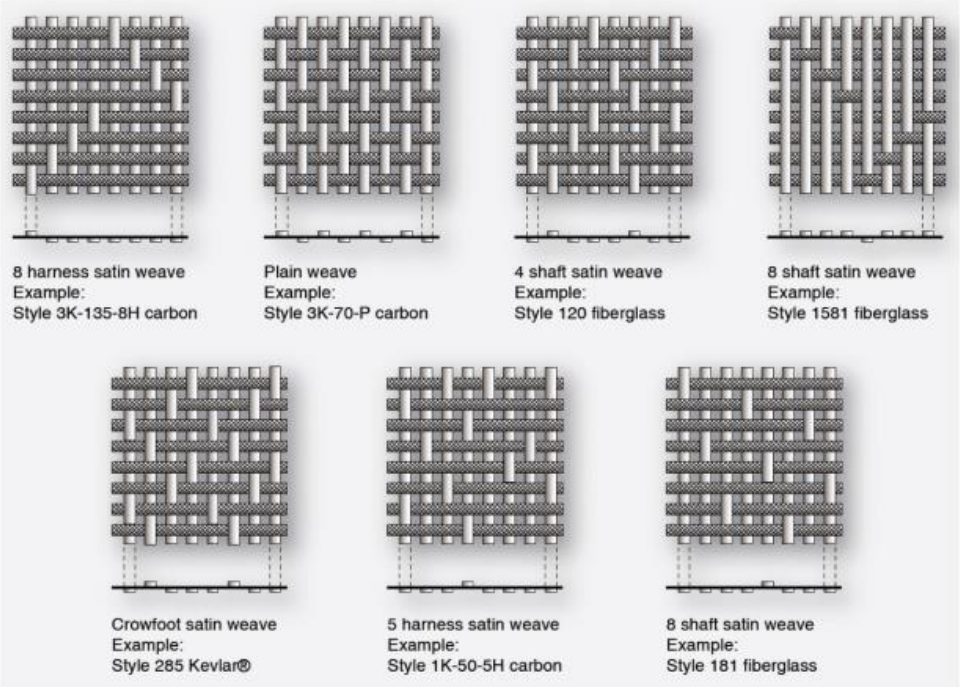

Figure 15: Various woven composite fiber layouts (Aeronautics Guide, 2020)

There are benefits and drawbacks to both unidirectional and woven fibers. Unidirectional laminates can have as many layers as desired to pass structural requirements. Fibers can be oriented in any direction as well, where 0° is commonly set in the direction of principal (local) axial loads, ±45° for shear loads, and ±90° for side loads. For many aerospace applications, composite structures are made of quasi-isotropic materials. Quasi-isotropic materials are defined as having uniform properties in all directions, which is independent of the axis of testing. For comparison, aluminum and titanium, which are common cryogenic materials, are quasi-isotropic

metals. The stacking sequence to simulate quasi-isotropic materials is illustrated in Figure 16 which can also be written as [0/90/±45]s (Aeronautics Guide, 2020). In a study by Meng, et. al. on the leakage performance of a CFRP laminate under cryogenic temperature, it was observed that quasi-isotropic layup, $[0_2/+45_2/-45_2/90_2]$s, used in the experiment showed high leakage resistance compared to an orthogonal layup ([0/90]4s), which is an area of interest for this project (Meng et al., 2022).

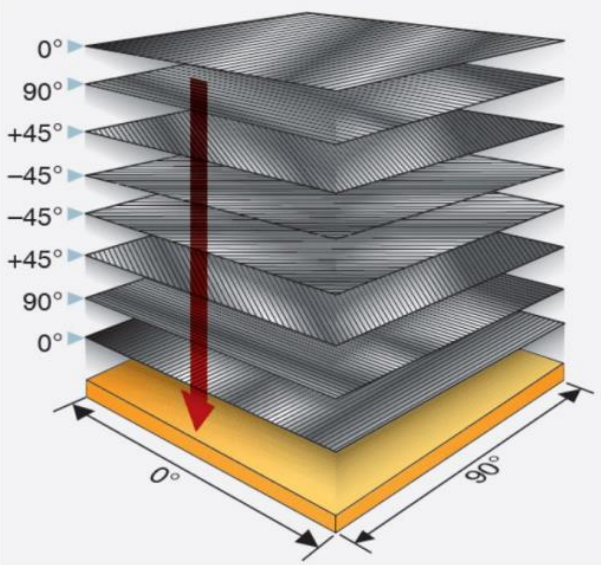

Figure 16: Quasi-isotropic stacking sequence used to simulate properties of quasi-isotropic metals (Aeronautics Guide, 2020)

Woven fibers are more optimal for creating complex shapes since they can be easily laid over a 3D contour without having fibers separating/spreading out. It is important to avoid fiber separation since it can create voids, which in turn will compromise the integrity of the laminate by creating cracks that can propagate and cause structural failure. Woven fibers are more ideal for machining as well. For example, if a hole was drilled in the material, the interlocking fibers would still hold the material together. For unidirectional lamina, the crack would propagate along the fiber direction and split it in two. These benefits come at the cost of processing time to weave the fiber, which is associated with a higher cost compared to unidirectional fibers. For woven fibers, the fibers weave over and under each other, which compromises the strength of the fibers. The fibers have fixed directions, with half of the fibers pointing in each direction. Woven fibers are also likely to experience a crimping effect which is highlighted in Figure 17.

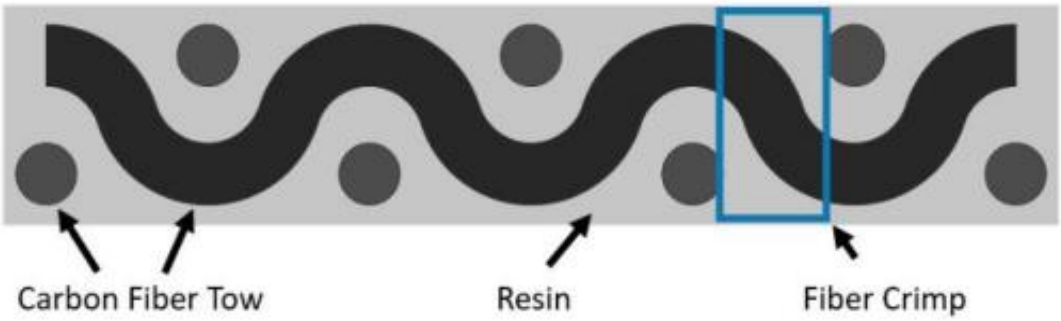

Figure 17: Illustration identifying where crimping occurs in woven fiber composites (Olliges, 2019)

1.1.4.4 Classical Laminate Theory

A popular method to describe the behavior of composite materials is using classical laminate theory (CLT). A laminate is defined as two or more unidirectional lamina (parallel fibers in plane with each other), also referred to as "layers" or "plies", that are stacked (not woven) together. The stacking sequence gives the orientation of fibers with respect to a global axis, which corresponds to the dimensional directions of the laminate, starting with the top lamina (Fragoudakis, 2019). The nomenclature is defined as follows:

- Different orientations are separated by the '/' symbol
- Repeating groups have a subscript 'n', where 'n' is the number of repetitions
- Stacking sequence is enclosed in square brackets
- Symmetric laminates are denoted by subscript 's'

For example, Table 6, which denotes several stacking sequences, has a stacking sequence $[(\pm 45)_2/0]s$. This means that the fiber orientation, beginning with the top lamina, is +45°, -45°, +45°, -45° and 0°. Since it is denoted by the subscript 's', this means there will be the same fiber orientation but in reverse order (i.e. 0°, -45°, +45°, -45°, +45°). Therefore, there will be a total of 10 layers. This is illustrated in Figure 18, note that the z-axis is in the direction for lamina thickness and the +y-axis (not shown) is pointing out of the page. The midplane is defined at 'z=0' with the topmost layer defined at 'z = -H' and the bottommost layer is at 'z = +H'.

Table 6: Examples of classical laminate theory stacking sequences.

Stacking Sequence	Description	# of Layers
[90/45/0]	One layer of 90°, 45°, and 0°	3
$[(45)_2/0]$	Two 45° layers and one 0°	3
[±45/±90]	+45°, -45°, +90°, and -90° layers	4
$[(\pm45)_2/0]_s$	Symmetric with one group of +45°, -45° and one 0° layer	10
$[02/45_2/-45_2/90]_s$	Symmetric with pairs of 0°, +45°, -45°, and 90° layers	16

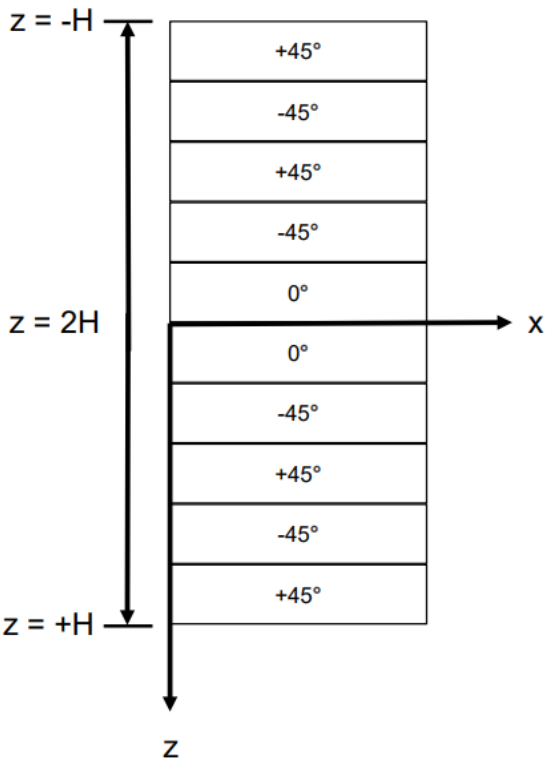

Figure 18: Illustration of stacking sequence [(±45)2/0]s

CLT would not be plausible without some key assumptions. First, it is assumed that the laminate has perfectly bonded layers, with no slip between adjacent layers. Displacement continuity through laminate thickness is assumed as well, with displacements assumed to be small relative to the thickness of the laminate. Each laminate is homogenous so that the effective

properties are known. Each lamina can be isotropic, orthotropic, or transversely isotropic, and is considered to be in a state of plane stress. Transverse shear stresses will be neglected, and the laminate will deform according to the Kirchhoff-Love assumption for bending and stretching of thin plates (NPTEL, n.d.)

To determine the behavior of the composite material under mechanical stresses, the Tsai-Hill failure criterion will be implemented to determine if each lamina can withstand the stresses applied on it. The formula for determining this is presented as follows:

$$\left(\frac{\sigma_{11}}{X_{11}}\right)^2 - \left(\frac{\sigma_{11}\sigma_{22}}{X_{11}}\right) + \left(\frac{\sigma_{22}}{X_{22}}\right)^2 + \left(\frac{\tau_{12}}{S_{12}}\right)^2 \geq 1 \quad (18)$$

where X_{11} is the minimum value of the allowable tensile or compressive strength in the longitudinal direction (0°), X_{22} is the minimum value of the allowable tensile or compressive strength in the transverse direction (90°), S_{12} is the plane shear stress, σ_{11} is the stress in the global axis x-direction, σ_{22} is the stress in the global axis y-direction, and τ_{12} is the stress in the global axis xy-direction. See Figure 19 for a visual of the coordinate system. If the inequality is proven to be true, then the lamina will not rupture. This calculation can be made into an iterative process by checking each lamina, starting from the top and going down, to determine if each lamina passes the Tsai-Hill criterion.

The Tsai-Hill criterion is useful since it can be used to check different composite layup configurations to see if it would fail under the expected stresses the composite would experience. It is important to note that if a single lamina fails, then the entire composite fails, and new configurations must be tested.

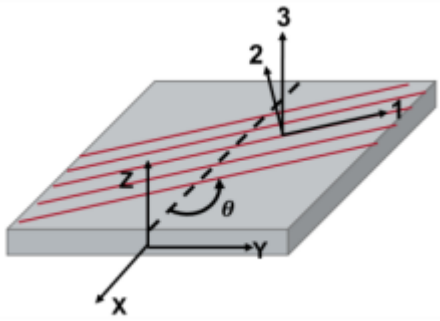

Figure 19: Global and rotated coordinate system of a lamina (Krarajgokar, 2022).

1.2 Project Objectives and Methods

To help guide the team and give direction to conduct studies and experiments, a set of overarching project objectives were made. These objectives correlate to the aspects of the project that were most focused on, helping the team home in on what topics were most important. The finalized list is shown below.

1. Conduct Research into Fundamental Topics
    a. Conduct literature reviews on the topics of boil-off and heat transfer, composite material science and curing, types of venting systems, and types of boiloff mitigation techniques.
2. Create a Set of Design Parameters
    a. Create mission that will be the basis for all analyses.
    b. Create models to test different tanks, designs, and geometry for thermal efficiency.
    c. Choose type of venting system for spacecraft.
    d. Using experimentation, analysis, and simulation, investigate the effects of different material types on heat flux through the walls of different types of tanks.
3. Validate Models Through Experimentation
    a. Formulate testing procedures for the following experiments:
        i. thermal analysis of heat transfer through tank walls.
        ii. Curing composites for use in permeability experiments.
        iii. MLI creation for use in thermal testing.
        iv. Permeability experiments to characterize the permeability for different layups of CFRPS.
    b. Create a computational model that an quantify the amount of boiloff in a cryogenic tank based on tanks size, type of fuel used, and ΔV required.
    c. Validate created models with results derived from experiments.

1.3 Project Management

To effectively achieve all our objectives, it was necessary to split the team into sub-teams. Additionally, each member of the team had a specific role that led to facilitation of meeting project objectives.

1.3.1 Members and Roles

Member	Team Role	Contributions
Jacob Borowsky	Project Lead	Boil-off model and analysis Tank design research
Jack Charbonneau	Lab Monitor	Thermodynamics research Boil-off model and analysis COMSOL simulations
John Dougherty	Procurement Lead	Material research Permeability testing
Alexander Lagle	Presentation Lead	Thermal testing Venting testing
Nicholas Masse	Report Lead	MLI research and testing
Jacob Mitchell	Safety Officer	Venting research and testing
Deep Patel	Scribe	Material research Permeability testing
Rory Veguilla	Lab Monitor	Venting research, testing, and analysis

Additionally, all members of the team completed an STK level one certification to assist in modeling our mission.

2 Preliminary Design

To run tests, the team designed a mission scenario to perform analysis related to heat transfer researched in the literature review. Additionally, several design choices were made to model elements of the spacecraft propellant tank material that could be simulated in COMSOL and would support experiments on three key elements. These choices bridged the gap between the literature review and the performed experiments.

2.1 Mission Design

In spacecraft design, the initial basis for all things is the mission itself. The mission and its goals are what drive almost all design factors, directly or indirectly. To have a platform where one could conduct analysis on the performance of cryogenic tanks, the team needed to choose a mission. From this, the team was able to find necessary ΔV requirements, which is necessary to know the amount of propellant needed for each maneuver the spacecraft performed. This then affected the relative size of the tanks and could be used to estimate boil-off.

The team first decided that a deep space mission would be the best for analysis. Two main destinations were analyzed: the Moon and Mars. The team eventually decided that the Moon was the best celestial body to visit, as a total trip time would be on the magnitude of days, where a Mars mission could possibly last from months to years.

With a mission to the Moon decided, the path to get there was then plotted. After conducting research, the team took inspiration from the Moon missions of the Apollo Era, where the command module, service module, and lunar lander were sent on a trajectory to intercept the Moon from a boost given by the upper stage of the Saturn V. The spacecraft then coasted for 73 hours while on route to the Moon. Upon arrival, the service module initiated a burn to capture the spacecraft around the Moon, and finally after the mission to the lunar surface had ended, conducted another burn to put the spacecraft on a trans-earth trajectory to bring the spacecraft back to earth in 52 hours. A schematic that shows the mission is below in Figure 20.

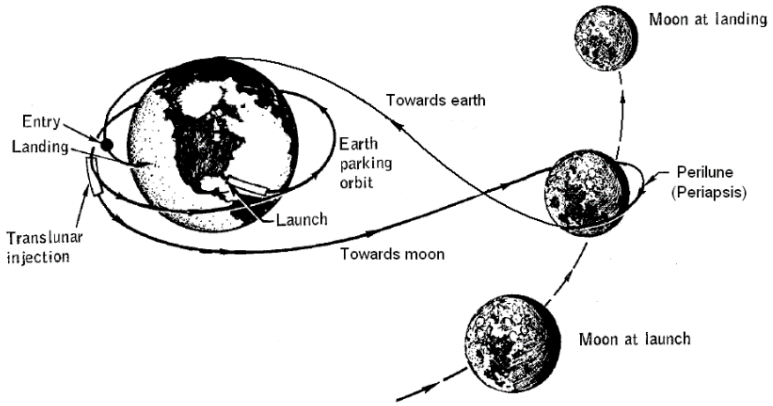

Figure 20: Apollo trajectory schematic (NASA, 1969)

2.1.1 Delta-V Requirement

The whole mission had two total burns, giving the amount of ΔV required to complete the mission. The chart below shows the ΔV values for each maneuver for a typical Apollo mission.

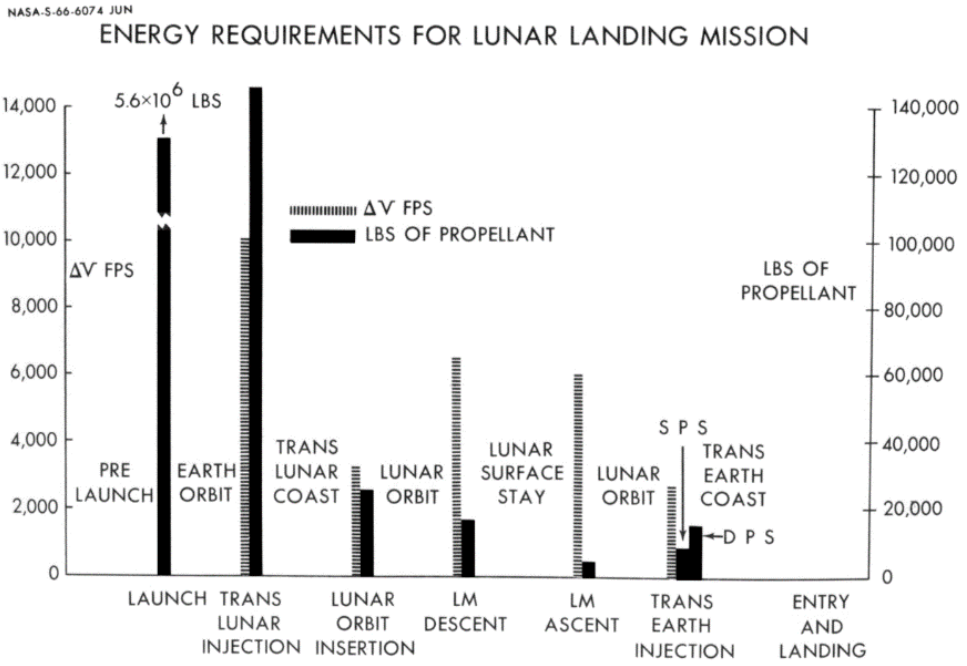

Figure 21: Apollo energy requirements (Maynard, 1966)

The data points most useful for the mission team is studying would be the ΔV values for the lunar orbit insertion, and trans-earth injection. All ΔV values for launch and a landing would

not be applicable in our case. In total the ΔV needed to complete the mission would be approximately 2000 m/s. With these values in hand, the team was able to start the design of the spacecraft itself. Table 7 below shows the ΔV required to inject into each phase of the mission and its duration.

Table 7: Required mission ΔVs and durations

Mission Phase	ΔV required (m/s)	Duration (hr)
Trans-Lunar	Done by launch Vehicle	73
Lunar Orbit	937.6	24
Trans-Earth	999.4	52
Total	1937	149

2.1.2 Changes in Propellant Levels Throughout Mission Phases

As noted above, the spacecraft will execute two burns: a lunar orbit insertion and trans-earth injection. While these are the two occurrences of designed propellant release, propellant will also be lost throughout the entire duration of the mission due to boil-off. Figure 22 below is a visual representation of when and how propellant is lost throughout the mission.

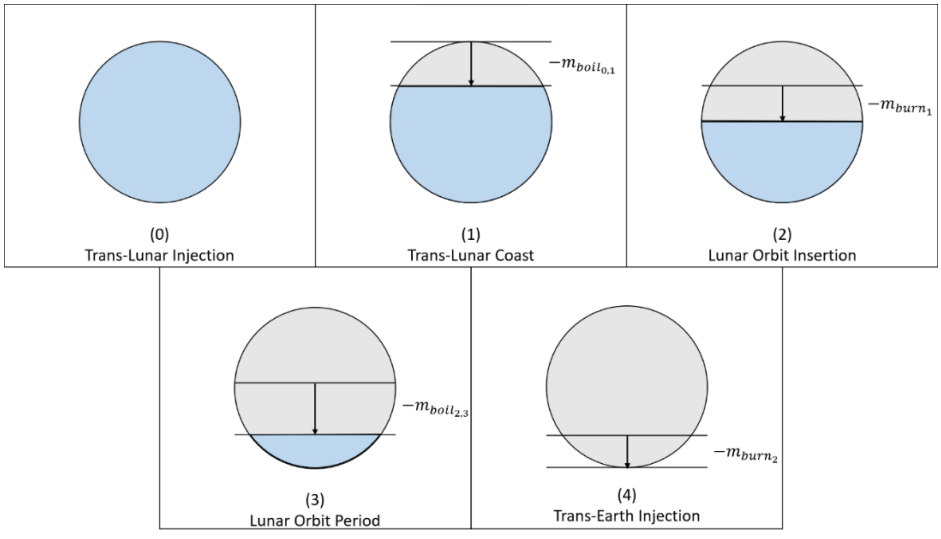

Figure 22: Chronological display of fluid (fuel or oxidizer) release

The spacecraft begins the mission on the trans-lunar injection trajectory. For simplification of the boil-off analysis, the team assumed the fuel tank is topped off with fuel until being released. Therefore, at time zero, the fuel tank is full. During the trans-lunar coast period the spacecraft is subjected to solar radiation, which heats the tank, and causes the first loss of fuel due to boil-off, $-m_{boil_{0,1}}$. Then, the lunar orbit insertion burns fuel at an assumed instantaneous rate, $-m_{\text{burn}_1}$. This approximation is valid when the boil-off rate is significantly lower than the burn rate associated with a ΔV burn and because the time span of a burn is insignificant to the scale of the mission duration. Next, a one-day long orbit period is introduced to simulate a 'science collection' period of a spacecraft mission. During this time, fuel will again be lost due to boil-off at an amount of $-m_{boil_{2,3}}$. After this, the remaining fuel, $-m_{\text{burn}_2}$, will be used to escape the lunar orbit and place the spacecraft on a trans-earth injection orbit.

The simplified Apollo style mission allowed the team to assume that no fuel is needed for the spacecraft to be captured by earth's gravitational pull and descend naturally, rather than inserting itself into another Earth-centric orbit, which would require another burn. Therefore, the fuel tank is assumed to be empty after the burn at stage 4, i.e., $m_4 = m_f = 0$, and analysis into the boil-off on the return trajectory to Earth was not required. The fuel amounts are referenced as negative values above to indicate the loss of fuel from $m_0\ to\ m_f$. More information on the thermal effects on the spacecraft and their application to this model are elaborated on in section 2.3. The STK analysis of the mission is discussed in section 2.3.1.1.

2.2 Spacecraft Design

This section details the design choices made by the team in creating the spacecraft used to understand and measure how the choices in propellant, thruster, tank shape, tank material, and boil-off mitigation techniques affect the boil-off rates of said propellants, based on research presented in section 1.1.

2.2.1 Propellant and Engine Selection

As described in section 1.1.1, LH_2 is the most used cryogenic fuel due to its high efficiency, yet its tendency to leak and extremely low boiling point makes it incredibly difficult to store. A promising alternative, therefore, has proven to be LCH_4. While its specific energy is lower than that of LH_2, its higher boiling point and higher density yield optimizations in

spacecraft weight and propellant boil-off rates. Therefore, based on these factors, two spacecraft configurations were created for the purposes of our mission outlined in section 2.1: one configuration containing LH_2/LOx, and the other containing LCH_4/LOx. The purpose of comparing two cryogenic fuels, as opposed to selecting one, was to understand how, if at all, properties such as the boiling point, density, and enthalpy of vaporization of these propellants affected their boil-off rates. From these effects, it was determined if certain fuels better mitigated boil-off and if these mitigations outweighed other important factors, such as increases in weight and reduction in performance.

For the LH_2/LOx configuration, the Aerojet Rocketdyne RL-10C-1 engine (as shown in Figure 23) was chosen as it is a flight-proven LH_2/LOx thruster that has been used on a multitude of mission and launch vehicles, with the most recent being on the Interim Cryogenic Propulsion Stage (ICPS) of NASA's Space Launch System (SLS) that will send astronauts to the Moon and beyond. Additionally, the ICPS technical data, which was needed to design the team's propellant tanks, is public and readily available.

Figure 23 : RL-10 engine (left) (Harbaugh, 2022) on the interim cryogenic propulsion stage of NASA's SLS (right) (Mohon, Getting to Know You, Rocket Edition: Interim Cryogenic Propulsion Stage, 2017).

Similarly, for the LCH_4/LOx configuration, the Avio M10 engine was chosen as it is one of the few operational methane thrusters (AVIO, 2022). Additionally, it is one of the few

thrusters with publicly available technical data, which was needed to design our propellant tanks.

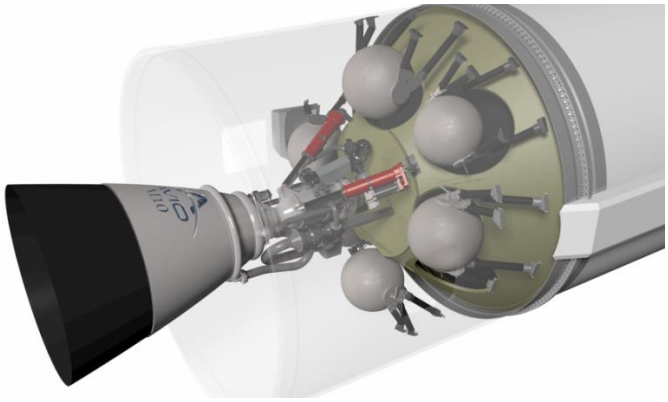

Figure 24: M10 thruster on the upper stage of the Vega-E (AVIO, n.d.)

2.2.2 Initial Tank Design, Sizing, and Materials

This section describes in detail the team's selections in tank shape and material based on research presented in section 1.1. Additionally, hand calculations from section 1.1.4 are provided to show initial justification for our choices, and to demonstrate the impact each of these factors has on mitigating boil-off.

2.2.2.1 Initial Tank Design and Sizing

As discussed in section 1.1.4 spherical tanks are the best for minimizing weight and boil-off, yet they are difficult to incorporate into the body of a rocket. However, using the relevant ΔV values from Figure 21 and the equations outlined in section 1.1.4, a preliminary analysis was conducted to determine if the required propellant amount could be stored in spherical tanks small enough to fit in commonly used launch vehicles.

Using the ΔV requirement of 1,936.5 m/s, an initial wet mass guess of 33,000 kg (which is the approximate wet mass of the ICPS (Harbaugh, 2022), a 5% volume safety factor, and the specifications of the RL-10 engine, the radius and surface area of the cryogenic fuel and oxidizer tanks were calculated as shown below. Some notes about this process: these calculations were performed using LH_2-specific parameters (i.e., density and thruster) as the LH_2 tanks will be larger than the LCH_4 tanks due to the higher density of LH_2, therefore providing a maximum tank size that can fit in commercially available launch vehicles. Additionally, a factor to account for boil-off losses was not considered in the initial tank design as the boil-off model discussed

later in section 2.3.2 was not created when this initial sizing was first conducted. However, to account for boil-off, the mass of fuel and oxidizer lost would have to be calculated and factored into the initial wet mass, as described later in this section.

$$m_f = (33{,}000\ kg)e^{-\frac{1{,}936.5\frac{m}{s}}{\left(9.81\frac{m}{s^2}\right)(450\ s)}} = 21{,}282\ \text{kg}$$

$$m_{p_{total}} = (33{,}000\ kg - 21{,}282\ kg)(1.10) = 12{,}890\ \text{kg}$$

<u>LH_2:</u>

$$m_{p_{fuel}} = \frac{12{,}890\ kg}{5.5 + 1} = 1{,}983\ \text{kg}\ LH_2$$

$$V_{LH_2} = 1.05\left(\frac{1{,}983\ kg}{71\frac{kg}{m^3}}\right) = 29.33\ m^3$$

$$r_{LH_{2}tank} = \sqrt[3]{\frac{(3)(29.33\ m^3)}{4\pi}} = 1.91\ \text{m}$$

$$SA_{LH_{2}tank} = 4\pi(4.04\ m)^2 = 46\ m^2$$

<u>LOx:</u>

$$m_{p_{oxidizer}} = (1{,}983\ kg)(5.5) = 10{,}907\ \text{kg LOx}$$

$$V_{LOx} = 1.05\left(\frac{10{,}907\ kg}{1149\frac{kg}{m^3}}\right) = 9.97\ m^3$$

$$r_{LOx_{tank}} = \sqrt[3]{\frac{(3)(9.97\ m^3)}{4\pi}} = 0.881\ \text{m}$$

$$SA_{LH_{2}tank} = 4\pi(0.881\ m)^2 = 9.75\ m^2$$

However, since these calculations started with an initial guess for the wet mass, this process was iterated upon by adding the calculated propellant and oxidizer masses, propellant and oxidizer tank masses (per equation (9)), the thruster mass (obtained from Avio and Aerojet data sheets), and an assumed 500 kg to account for additional propulsion hardware and a generic payload to obtain a new wet mass. This was substituted back into equation (13) to obtain new fuel and oxidizer mass values. This process was automated using the Excel spreadsheet shown section 6.8 until a value for the wet mass was converged upon, yielding masses, volumes, and

radii for initial construction of our tanks. This process was repeated for the LCH_4 configuration, yielding the following mass breakdowns shown in Table 8.

Table 8: Initial propellant mass and volumes for spacecraft configurations

	Configuration			
Fuel and Oxidizer	LH_2/LOx		LCH_4/LOx	
Fuel and Oxidizer Mass (kg)	68.8	378.8	149.5	508.2
Fuel and Oxidizer Tank Volume (m^3)	0.971	0.329	0.354	0.442
Fuel and Oxidizer Tank Inner Radius (m)	0.614	0.428	0.439	0.473
Fuel and Oxidizer Tank Surface Area (m^2)	4.75	2.31	2.42	2.81

For comparison, the ICPS has a radius of 8.35’ (2.55 m), and SpaceX’s Falcon 9 has a radius of 6’ (1.85 m), both of which would be able to accommodate our tanks (Harbaugh, 2022). Therefore, since these calculations show spherical tanks for the chosen mission can be incorporated into commercially available launch vehicles, the team chose two spherical propellant tanks, rather than capsule-shaped ones, for the designed spacecrafts. This choice allowed the team to minimize the vehicle’s weight, tank surface-to-volume ratio, and rate of heat transfer across the tank surface, therefore aiding in the reduction of propellant boil-off.

Additionally, the data in Table 8 shows that propellant choice can also aid in the reduction of mass and boil-off rates. Since LCH_4 is denser than LH_2 it can be stored in smaller tanks. As a result, the LCH_4 spacecraft is theoretically heavier, but has a smaller overall surface area than the

LH_2 spacecraft, minimizing the area for heat to transfer into the propellant and cause boil-off, all while meeting the same mission requirements.

2.2.2.2 Tank Material

As discussed in section 1.1, composite materials have been proven to reduce the cost and weight of cryogenic tank structures and have more desirable mechanical properties compared to aluminum alloys. One of these properties is a lower thermal conductivity, which reduces the heat flux into the propellant tanks. Therefore, the team compared the use of composite materials versus an aluminum alloy in the construction of our propellant tanks to determine how, if at all, material selection will impact boil-off. Specifically, the team opted to use prepreg CFRPs due to the level of prior research conducted and published data on these materials, as discussed in section 1.1.4.2.

The team selected AA 2024-T3 and Grafil 34-700 CFRP to compare a commonly used material in the aerospace industry with a material that possesses desirable properties for this application, such as a low density and low thermal conductivity, as discussed in section 1.1.4.2. Additionally, these materials had all the required technical specifications needed for preliminary calculations readily available, while also comparatively cheap to other options. The relevant material properties of each material are listed in Table 9 and

Table 10, respectively.

Table 9: Material properties of AA 2024-T3 (OnlineMetals, n.d.)

Density (kg/m^3)	2768
Thermal Conductivity (W/m K)	121
Ultimate Tensile Strength (MPa)	448
Specific Heat Capacity (J/kg K)	875

Table 10: Material properties and dimensions for Grafil 34-700 CFRP (Rockwest Composites, n.d.)

Ultimate Tensile Strength (MPa)	4826
Thickness (mm)	0.1524
Length (m)	0.914
Width (m)	1.00
Mass (kg)	0.213

The dimensions of the CFRP are listed as its density was not explicitly given. Instead, it was calculated using the dimensions as

$$\rho_{CFRP} = \left(\frac{m_{CFRP}}{V_{CFRP}}\right) = \left(\frac{m_{CFRP}}{L_{CFRP} W_{CFRP} t_{CFRP}}\right) = 1530 \frac{kg}{m^3}$$

However, upon obtaining the density and yield strength of the materials, initial thicknesses and masses of the propellant tanks made with each material were calculated from equations (6) and (4), as described in section 1.1.4. For these calculations a safety factor of 2 was used and a mass factor of 1.25 was used to estimate the propellant management device (PMD), as these are within typical used ranges. PMDs are devices used in rocket propellant tanks to ensure propellant provided to the thrusters is gas-free (PMD Tanks, n.d.). However, the effects of these devices on boil-off rates (outside of their mass) were not considered to simplify the project, due to time constraints. Finally, the LH_2 and LCH_4 tanks were pressurized to 30 psia and the LOx tanks were pressurized to 40 psia, as done on the third stage of the Saturn V, which closely mimics our spacecraft's mission and purpose (NASA, 1974)

Since the tank mass depends on its surface area, which is dependent on the propellant volume, the process for calculating tank mass and thickness was done iteratively and in tandem with calculating the propellant volume and mass. As done in section 2.2.2.1, this process was automated using the Excel spreadsheet until a value for the wet mass was converged upon, yielding initial tank masses and thicknesses. This process was repeated for both spacecraft configurations with both materials, yielding the following results.

Table 11: Initial propellant tank mass and thickness for AA 2024 spacecraft

Fuel and Oxidizer	LH_2/LOx		LCH_4/LOx	
Fuel and Oxidizer Tank Mass (kg)	4.85	2.20	1.77	2.95
Fuel and Oxidizer Tank Thickness (mm)	0.410	0.381	0.293	0.420

Table 12: Initial propellant tank mass and thickness for Grafil 34-700 spacecraft

Fuel and Oxidizer	LH_2/LOx		LCH_4/LOx	
Fuel and Oxidizer Tank Mass (kg)	0.24	0.11	0.09	0.14
Fuel and Oxidizer Tank Thickness (mm)	0.026	0.024	0.019	0.027

From the results in Table 8, Table 11, and Table 12 it is initially apparent that tank material, and therefore material properties, only affect the wall thickness and tank mass. These thicknesses are not realistically manufacturable, so the sheets of aluminum and CFRP would need to be stacked to meet achievable thicknesses. For comparison, the cryogenic tanks on the Saturn V were approximately 4 mm (McCutcheon, 2022). Propellant and engine choice, on the other hand, affect the total propellant amount, tank radius, tank surface area, and tank mass. Overall, this makes the propellant and engine choice seem more impactful in mitigating boil-off. However, as described in section 1.1.2.3, the main driver of boil-off is the heat flux from the Sun on the fluid in the tank. This flux in turn is affected by the material properties, i.e., thermal conductivities, of the insulation and material used on the tank. Therefore, when the thermal conductivities of these two materials are considered, it is apparent that material choice could have a greater contribution to mitigating boil-off. This contribution was made clear, however,

with results gained from the computational determination of the boil-off rates, as explained in section 3.3.4.

2.2.3 Boil-Off Mitigation Techniques

While the chosen techniques are effective in reducing boil-off, they cannot completely prevent it. Our chosen method of boil-off management is a continuous venting system similar to the one aboard the Saturn S-IVB rocket stage discussed in section 1.1.3.3. This system contributes to boil-off reduction as well as removes the gaseous hydrogen efficiently. Since the wrap-around duct system directs the vented gas parallel to the direction of the spacecraft and the venting process occurs continuously for the duration of the coast period, it can be assumed that there is a thrust imparted on the spacecraft for the duration of the mission and that the liquid propellant remains settled at the bottom of the tank. Without constant thrust, the liquid propellant is free to move around the tank, leading to a larger area of the tank wall becoming wet with propellant. Since the wetted wall area contributes to the boil-off rate, the CVS both reduces the boil-off rate and makes it easier to model boil-off (Neher, 1971).

The main difference between the CVS on the team's spacecraft and the one aboard the Saturn S-IVB is that since the S-IVB is an upper stage vehicle, the coast time is only a few hours compared to our mission which is a few days. Since the goal of this system is to keep the pressure in the tank steady and the system is venting into a vacuum, the following equation could be used to determine the specifications of the fixed sized orifice that the gaseous propellant is vented out of (where γ is the ratio of specific heats, R is the specific gas constant, P is the tank pressure, T is the tank temperature, A^* is the throat area/the area of the fixed sized orifice, and $\dot{m}$ is the mass flow rate). This equation is derived using isentropic flow relations and the ideal gas law (Sutton & Biblarz, 2017).

$$\frac{\dot{m}}{A^*} = \frac{P\gamma}{\sqrt{\gamma RT}}\sqrt{\left(\frac{2}{\gamma+1}\right)^{\frac{\gamma+1}{\gamma-1}}} \tag{19}$$

If the tank pressure rises above the intended value, an emergency vent will be opened to bring the pressure back to steady state. While the emergency vent is open, the mass flow rate will decrease with pressure, density, and temperature which will all vary with time unlike in the case of a CVS orifice. To address this difference, equation (19) can be solved for the mass flow rate

and written as a differential equation to derive equation (20). Density, pressure, and temperature were written as functions of time. The fluid density can be found by dividing the internal volume by the mass of the vapor while tank pressure and temperature at each instant of the flow can be found using equations derived using the isentropic relations (Furter et al., 2019; NASA, 2021). P_0 and T_0 represent the initial tank pressure and temperature respectively.

$$\frac{dm}{dt} = \frac{-A^* P(t)\gamma}{\sqrt{\gamma R T(t)}} \sqrt{\left(\frac{2}{\gamma+1}\right)^{\frac{\gamma+1}{\gamma-1}}} \tag{20}$$

$$\rho(t) = \frac{m}{V} \tag{21}$$

$$P(t) = P_0 \left(\frac{\rho(t)}{\rho_0}\right)^{\gamma} \tag{22}$$

$$T(t) = T_0 \left(\frac{\rho(t)}{\rho_0}\right)^{\gamma-1} \tag{23}$$

The above system of equations can be numerically integrated to solve for the propellant mass in the tank and equations (21) to (23), can be used to find the density, pressure and temperature over the time period of interest.

Alongside venting gas from propellant tanks, insulation is important for the design of a thermally efficient spacecraft. The insulation chosen for this mission, known as MLI, is widely used for in-space applications for its low mass, emissivity, and thermal conductivity. MLI can consist of up to 30 layers of alternating aluminized Mylar sheets and polyester netting to reflect solar radiation from the tank and limit conduction to the tank's walls. Aluminized Mylar is a sensible choice for an MLI reflector, with an emissivity value of 0.044 and a thermal conductivity of 0.155 W/mK at room temperature (Domen, 1991; Rule, 1996). However, it is Alongside venting boiled material from propellant tanks, insulation is important for the design of a thermally efficient spacecraft. The insulation chosen for this mission, known as MLI, is widely used for deep space applications for its low mass, emissivity and thermal conductivity. This MLI consists of 30 layers of alternating aluminized Mylar sheets and polyester netting to reflect solar radiation from the tank and limit conduction to the tank's walls. Aluminized Mylar is a sensible choice for an MLI reflector, with an emissivity value of 0.044 and a thermal conductivity of

0.155 W/mK at room temperature (Domen, 1991; Rule, 1996). However, it is important to consider the environment in which the MLI will be working. In operation, the temperature of the tank will be near 20K (the boiling temperature of Hydrogen), significantly colder than room temperature, meaning the properties of the materials will be different. In these conditions, aluminized Mylar has emissivity and thermal conductivity values of 0.0002 and 0.044 W/mK respectively (Heaney, 1998; Rule, 1996). Polyester netting has a thermal conductivity value of 0.09108 W/mK at the boiling temperature of Hydrogen (Ross, 2015). A 30-layer MLI composed of these materials will be 22 mm thick, and the team used an average thermal conductivity value of 0.1 W/mK to represent this blanket in simulations (Rule, 1996). This number is discussed further in section 4.2. This is highly effective in preventing solar thermal energy from warming the cryogenic fluid within.

Finally, rotating the spacecraft is a common method to reduce the peak heat flux from the Sun entering the propellant tanks and employed on the team's design. The rationale, with supporting simulations, for choosing this technique is described in further detail in section 2.3.1.2.

2.3 Thermal Analysis

Thermal analysis of the spacecraft and the cryogenic fuel storage tank is the primary result of this report and the most critical to the supporting experiments. Factors such as the temperature and heat flux incident on and within the spacecraft and its tanks are intrinsically linked to the various design choices and conclusions that were made in this project. The mission design discussed in section 2.1 introduced the requirement of understanding how the spacecraft will be heated throughout its mission in space. The spacecraft design and material selections discussed in section 2.2 require analysis for understanding how altering different properties will affect the boil-off. The sections listed below build off the supporting background research outlined in section 1.1.2, and answers the various questions of how to analyze the proposed problem, what simplifications can or need to be made, and how they affect the final solution.

2.3.1 Preliminary Heat Transfer Calculations

Prior to building the various experiments and the boil-off model discussed later in this paper, the team spent much of the beginning phase conducting basic calculations and simulations to gain a strong understanding of the physics at play. As discussed in sections 1.1.2.2 and 1.1.2.3,

an understanding of the internal effects of a cryogenic fuel storage tank requires an understanding of the external effects on the spacecraft and how heat will propagate through the tank wall. Section 2.3.1.1 provides an analysis of the thermal loading due to the power of the Sun and how this value will vary as the spacecraft traverses its mission. Section 2.3.1.2 discusses the initial simulations conducted through the computational software COMSOL to model how heat propagated through the tank walls.

2.3.1.1 STK Solar Flux Analysis

To understand the thermal environment in space the spacecraft experienced, the team decided to conduct some analysis in Systems Tool Kit (STK), a Multiphysics software that allows for the study and simulation of spacecraft. The team's main goal was to figure out how long the spacecraft spent being exposed to the Sun, and if the distance between the Sun and spacecraft changed enough to create any significant differences in solar flux at the spacecraft. Figure 25 below shows the modeled mission's orbit in STK.

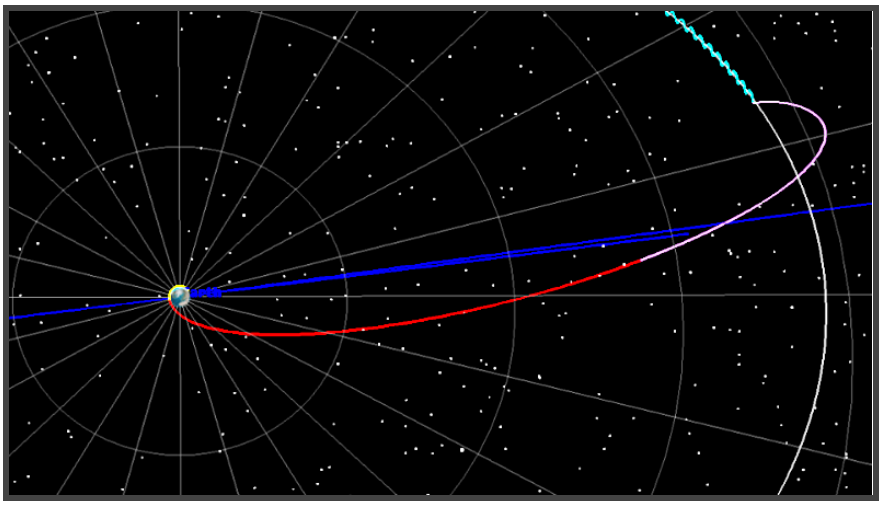

Figure 25: Trajectory of spacecraft modeled in STK

STK has many tools for analysis, but the team could not find one that specially gave the flux imparted on the spacecraft by the sun. Flux is the power per unit area the sun creates through its emission of electromagnetic radiation. This flux can transfer thermal energy on surfaces it is imparted on. To calculate this, a spreadsheet was made. This spreadsheet took the apparent vector of the sun's direction from the spacecraft, and luminosity data of the spacecraft to figure out two things, the flux imparted on the spacecraft at its current distance from the sun,

and if the spacecraft was being shadowed by any celestial bodies. Doing this produced the graph shown in the figure below.

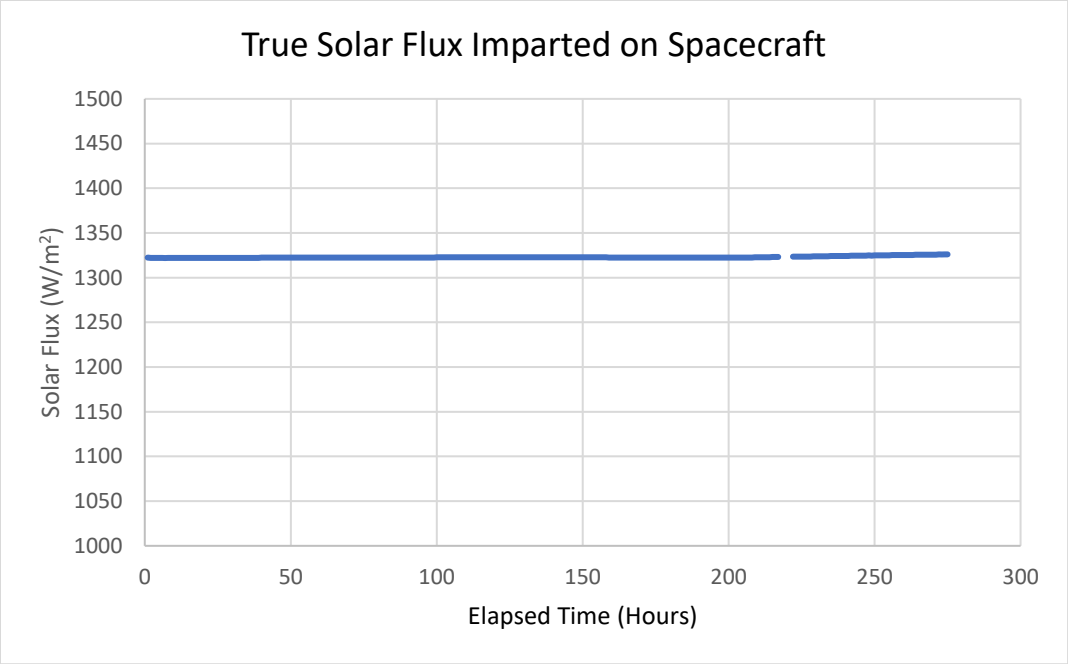

Figure 26: Flux imparted onto spacecraft

As seen in the graph above, the flux imparted on the spacecraft was steady and constant, which showed the team the thermal energy from the sun will not change at all during the mission. The data did show a small gap, which was found to be from a small eclipse period the spacecraft experienced while orbiting the moon during its lunar phase of the mission. The team believed there were a few reasons why these results made sense. One being the fact that is in relative scale of the entire solar system, the distance between the Moon and Earth is tiny compared to the distance between the Sun and Earth/Moon. This is why there was no decrease or increase in the flux's magnitude. The team also understood that the reasoning behind why there wasn't much effect from eclipsing celestial bodies is that the times periods where those eclipses occurred were extremely short compared to the entire elapsed time of the mission, thus their effect was minimal. The team also considered the effect from the Earth's Albedo. Due to the spacecraft quickly distancing itself from the planet, the team found it safe to assume it had little to no effect on the mission. With this analysis completed, the team was able to safely assume that the solar flux would not change based on the spacecraft's trajectory and used these assumptions for the rest of the analysis.

2.3.1.2 COMSOL Modeling of Heat Transfer Through Tank Walls

To understand the thermal effects on the exterior of the spacecraft, the team conducted multiple baseline and conclusive simulations in COMSOL, a finite element analysis, solver, and simulation software capable of modeling complex multi-physics problems. Initial studies were conducted for the team to gain an understanding of the software and how to apply its functionality to this project.

The simulations discussed below were modeled as displayed in Figure 27. A 2D approximation was utilized for the model to simplify calculations. While the spacecraft tank is curved by nature, the rectangular approximation is valid since the conditions along the interior and exterior of the tank do not change relative to the location on the tank skin. Additionally, the cross-section can be considered as any infinitesimally small section of the tank wall, which when scaled up will be nearly rectangular. The cross-section length is set as 1m wide and 1m in depth, therefore making all computational results of flux intrinsically measured in $[W/m^2]$. As discussed below in section 2.3.2.1, the tank wall material thickness was taken as 1mm regardless of material type. This is a valid assumption based on the manufacturability of thin sheets of aluminum or composite materials. Furthermore, the tank wall being analyzed in the below studies was constructed of a 1mm thick aluminum (AA 2024) panel and a 20mm thick MLI blanket. The thickness of the MLI is in in line with industry standard practices as discussed in section 1.1.3.1. The calculation for the thermal conductivity of the MLI is discussed further in section 4.2.

Three boundary conditions were set for this analysis. First, the incident flux on the spacecraft was confirmed to remain constant throughout the duration of the mission (explained above in section 2.3.1.1) at a value of $\dot{q}_{sol} = 1367\ W/m^2$. Next, to focus the calculations on the y-axis of the model, the heat transfer though the bounding walls, (2) and (3), is set to zero, i.e., they are perfect insulators. Lastly, the temperature of the inner tank wall was assumed to remain constant at the boiling temperature of the liquid as its temperature cannot rise past this point. Based on this point, the initial condition was chosen that the tank wall temperature starts equalized with the boiling temperature of liquid.

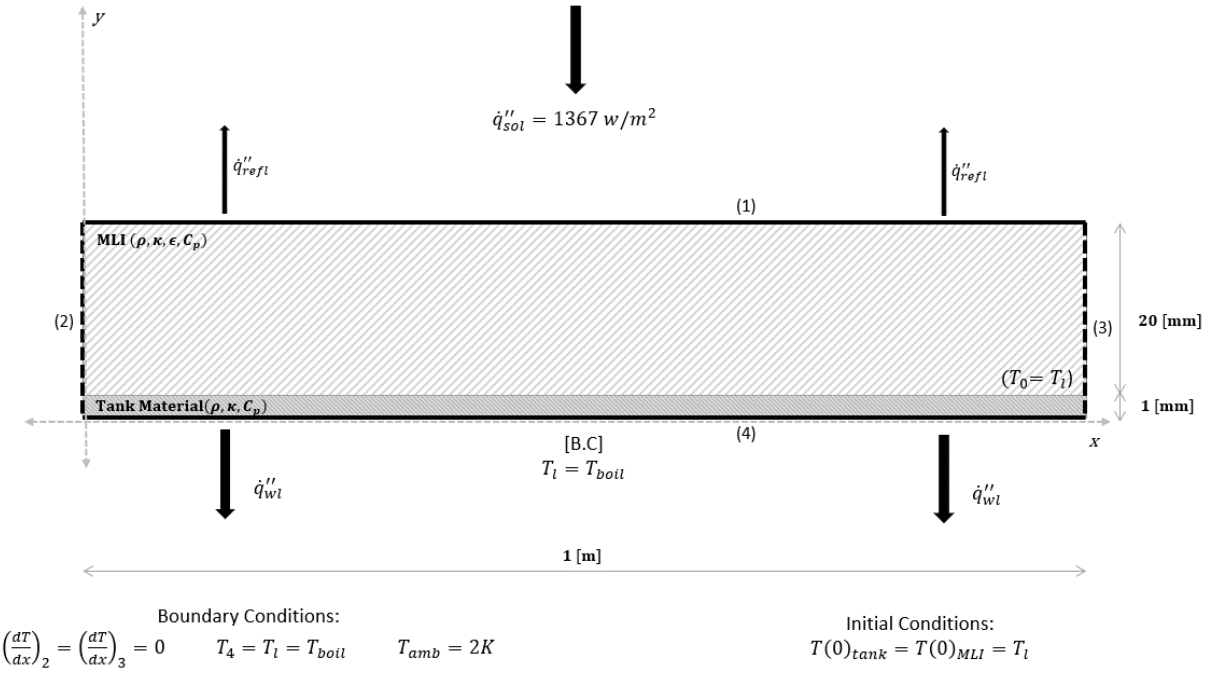

Figure 27: 2-D tank wall COMSOL model schematic

The model is based on two physics simulations – surface-to-surface radiation and heat transfer in solids. The "Surface-to-Surface Radiation" module defines how the incoming radiation will affect the surface of the spacecraft due to its emissivity, ϵ. As described in section 1.1.2.1, the incident radiation on the exterior tank skin will be reduced in its intensity proportional to its emissivity. Furthermore, this module allows for the designation of a diffuse surface, or the surface for which re-radiation of heat may occur based on the surrounding conditions. As listed above, the ambient temperature is defined as $T_{amb} = 2K$ for the temperature of space. The "Heat Transfer in Solids module" defines how heat transfers through the tank wall based on conduction. Fundamentally, since two materials are present with different thermal conductivities, a differentiation in the temperature distribution along the thickness of the wall should be observed.

Non-Spinning Spacecraft Analysis

The first simulation that the team ran through COMSOL was a thermal analysis of the tank wall where the flux on the surface remained constant with time. Two studies were conducted: a steady-state analysis to measure the temperature gradient through the tank wall regardless of the incident radiation 'exposure time' and a time-dependent study to determine how

long it takes for the heat flux through the tank wall to equalize and the temperature gradient observed in the steady-state example to develop. As expected, the final temperature gradient results of both studies were identical. The results of the time-dependent study are displayed below in Figure 28 and Figure 29.

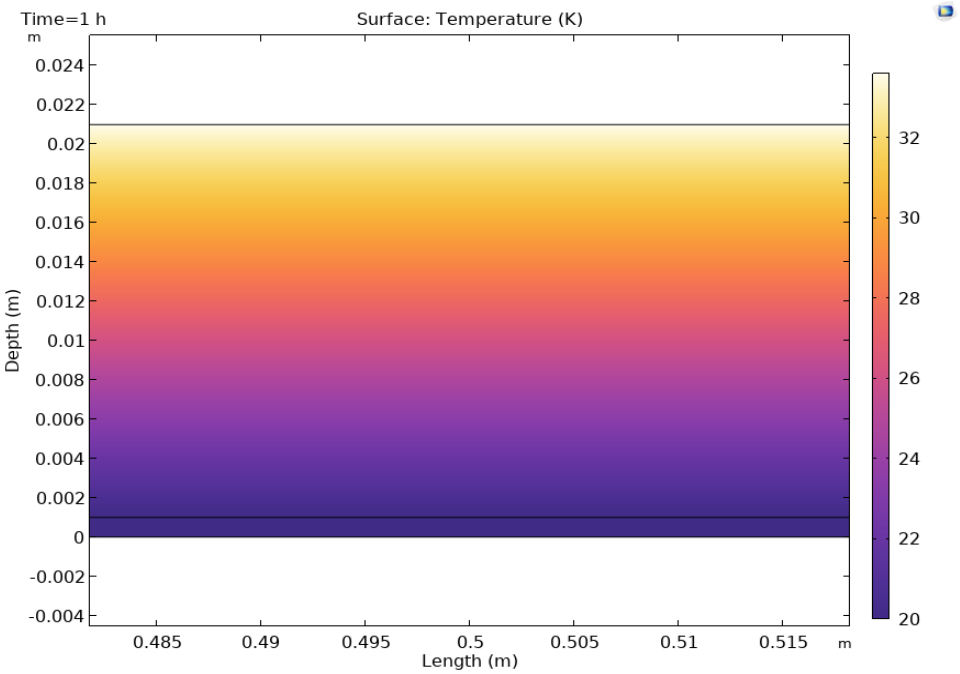

Figure 28: 2-D temperature distribution through tank wall (time-dependent study)

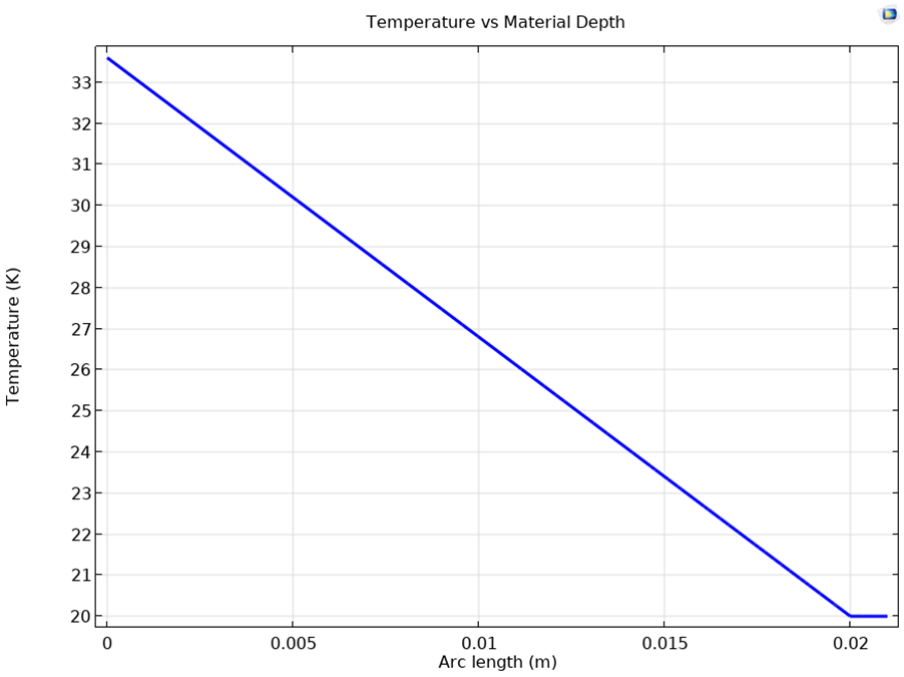

Figure 29: 1-D midline temperature distribution through tank wall (time-dependent study)

As expected, once the flux equalizes throughout the tank wall, the temperature distribution is linear with two defined separately defined gradients. The first linear portion of Figure 29 displays the gradient through the MLI, reaching a peak temperature of ~34K. The second linear portion, which at first glance appears constant, represents the temperature gradient through the aluminum wall. Due to the high thermal conductivity of AA 2024-T3 and its thinness, a noticeable temperature gradient cannot build up. However, upon further inspection it was noted that a 0.02K gradient over the 1mm thick panel exists. These gradients were confirmed by 'back-of-the-envelope' calculations using the basic conduction equation.

The time-dependent study results are displayed below in Figure 30. This graph displays the outward normal flux through surface (4) in Figure 27 over time as the heat flux through the tank wall to equalizes. The outward flux at surface (4) increases rapidly initially and settles at a value of approximately 68 $[W/m^2]$. Here the observation was made that an approximate value of the flux that will be imparted upon the interior of the tank is equal to the incident flux times the surface emissivity. This conclusion is supported by the fundamentals of radiative heat transfer discussed in section 1.1.2.1. Therefore, the important result of the various simulations and configurations that were tested was not how much flux could enter the tank wall, because all incident flux eventually would be, but how long the energy took to reach the liquid.

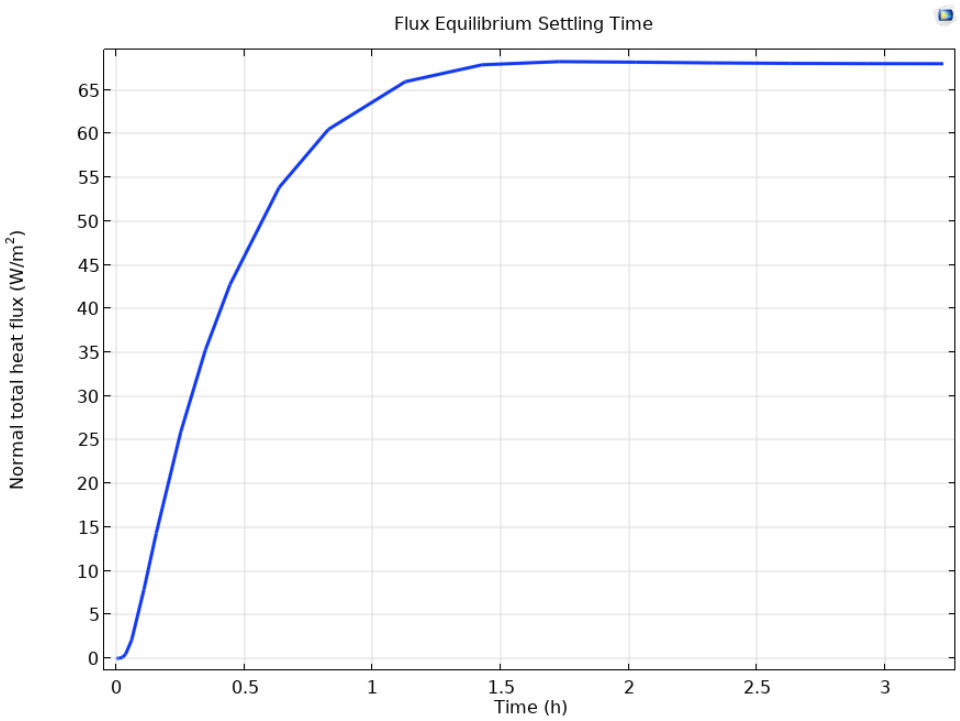

Figure 30: Time required to reach steady state for a non-spinning spacecraft

Figure 30 shows that for the AA 2024-T3 wall, steady state is reached in $\sim 1.5[h]$. Compared to the mission duration of 149 hours, this time is insignificant, leading the team to conclude that the flux on the fluid could be taken as constant. The conclusion from this study was that regardless of the configuration used for the mission, the flux incident on the spacecraft will reach the fluid. Therefore, the only potential methods to reduce the energy that reaches the liquid is to improve the reflective outer layer or increase the time required for the flux to equalize through the tank wall. Improving the quality of the reflector to lower the incident flux was determined to not be possible as MLI is the industry standard for highly reflective material, only allowing for approximately 5% of the incoming radiation to be transmitted. Furthermore, the amount of insulating material is directly related to how long the flux will take to reach the inner wall, but any significant improvements in time required unrealistically thick layers of insulations that would drastically increase the weight of the spacecraft.

Spinning Spacecraft Analysis

While the results above appeared conclusive on the effects of the incoming solar flux, further analysis was required to account for the effects of rotating the spacecraft as a means of

passive thermal control. As described in section 1.1.3.2, a widely used method to reduce the thermal loading on a spacecraft is to rotate the body at a controlled rate, allowing for some of its absorbed thermal energy to be re-radiated back out into space. To model this in COMSOL, the Surface-to-Surface radiation module was altered such that incoming solar flux was switched between a 'sun-on' condition where $\dot{q} = 1367\ [W/m^2]$ and a 'sun-off' condition where $\dot{q} = 0\ [W/m^2]$ at a rotation speed of three revolutions per hour based on the research in section 1.1.3.2. The 'sun off' condition does not set the overall normal flux at boundary (4) as zero but removes the addition of an incoming flux from the theoretical sun source. As previously mentioned, the Surface-to-Surface radiation module was configured to define a diffuse surface such that the model accounts for the re-radiation of energy back out to space. During the 'sun-off' condition, this re-radiation of energy is present and the key driving factor of this cooling method. While the incident flux is set to $\dot{q} = 0\ [W/m^2]$, the overall flux at boundary (4) will be less than 0, and therefore diffusing heat outward from the spacecraft body to space. Using Excel, this step function was modeled as data points, as depicted in Appendix 6.9, to be loaded into COMSOL as an interpolation function.

Figure 31 depicts the outward normal flux measured at boundary (4) versus time as the spacecraft is rotating. Based on this result, the team noted that the passive cooling method of rotating the spacecraft significantly improved the thermal loading on the spacecraft. As noted by the y-axis of the plot, the peak inward flux normal to the inner tank wall dropped from $\sim 68\ [W/m^2]$ to $\sim 37\ [W/m^2]$. The inward normal flux no longer equalizes to a single value but converges to an oscillation between a minimum and maximum flux. The passive thermal control also slightly increased the time taken for the flux to reach its new equilibrium behavior from $\sim 1.5[h]$ to $\sim 2.2[h]$. Figure 32 displays the same data with the variation in solar flux inputted into the calculation overlayed on the data for reference. Lastly, Figure 33 displays the 2D temperature variation in the tank wall over $t = [0, 0.5]\ hr$. From this result, the team concluded again that the time taken to reach the flux equilibrium condition is insignificant to the duration of the mission, and therefore the normal flux on the fluid can be assumed constant throughout the mission even with passive thermal control. More importantly, the team concluded that introducing passive thermal control reduces the normal flux into the fluid from $\approx 68\ [W/m^2]$ to $\approx 34\ [W/m^2]$ (taken as the average of the minimum and maximum fluctuations). For all future calculations in this report, the flux imparted through the tank wall was taken to be $\approx 34\ [W/m^2]$.

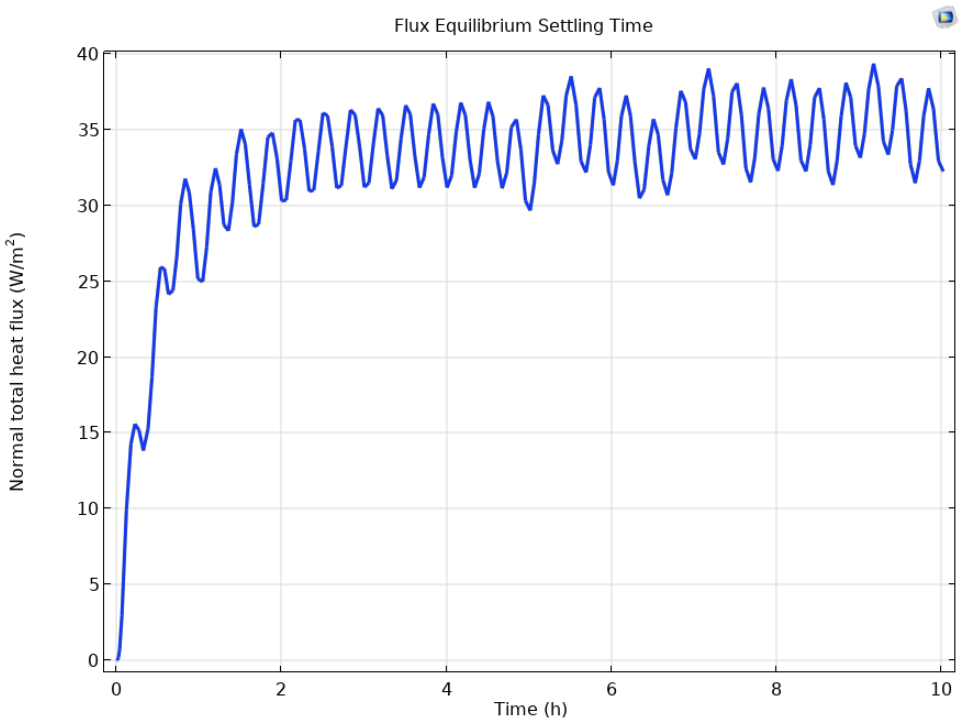

Figure 31: Outward flux variation in wall for spinning spacecraft

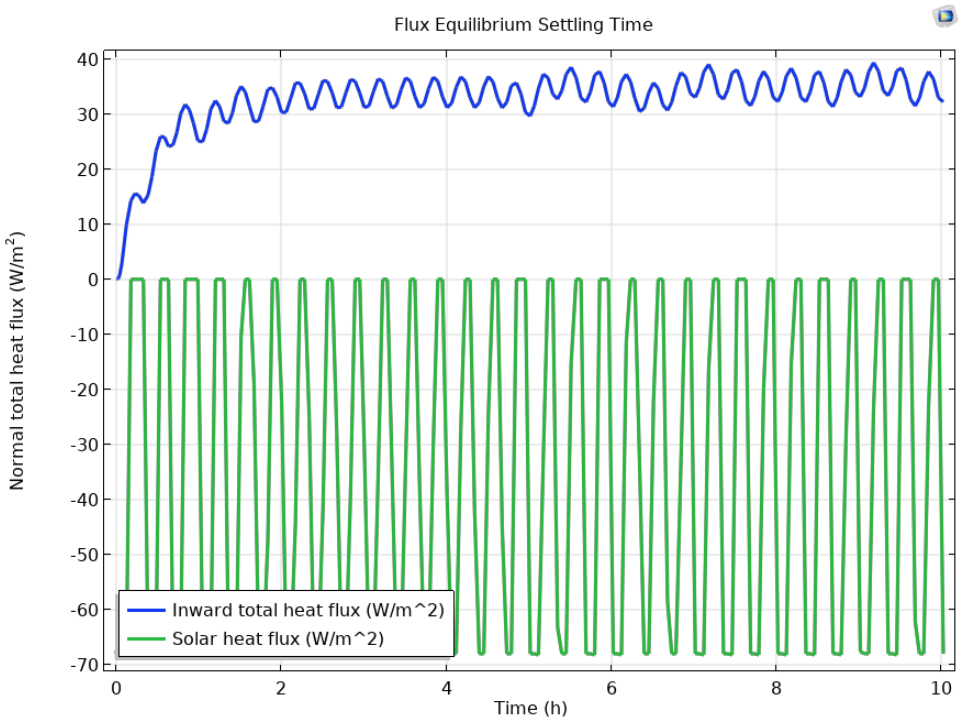

Figure 32: Outward flux variation in wall for spinning spacecraft with oscillating solar flux displayed

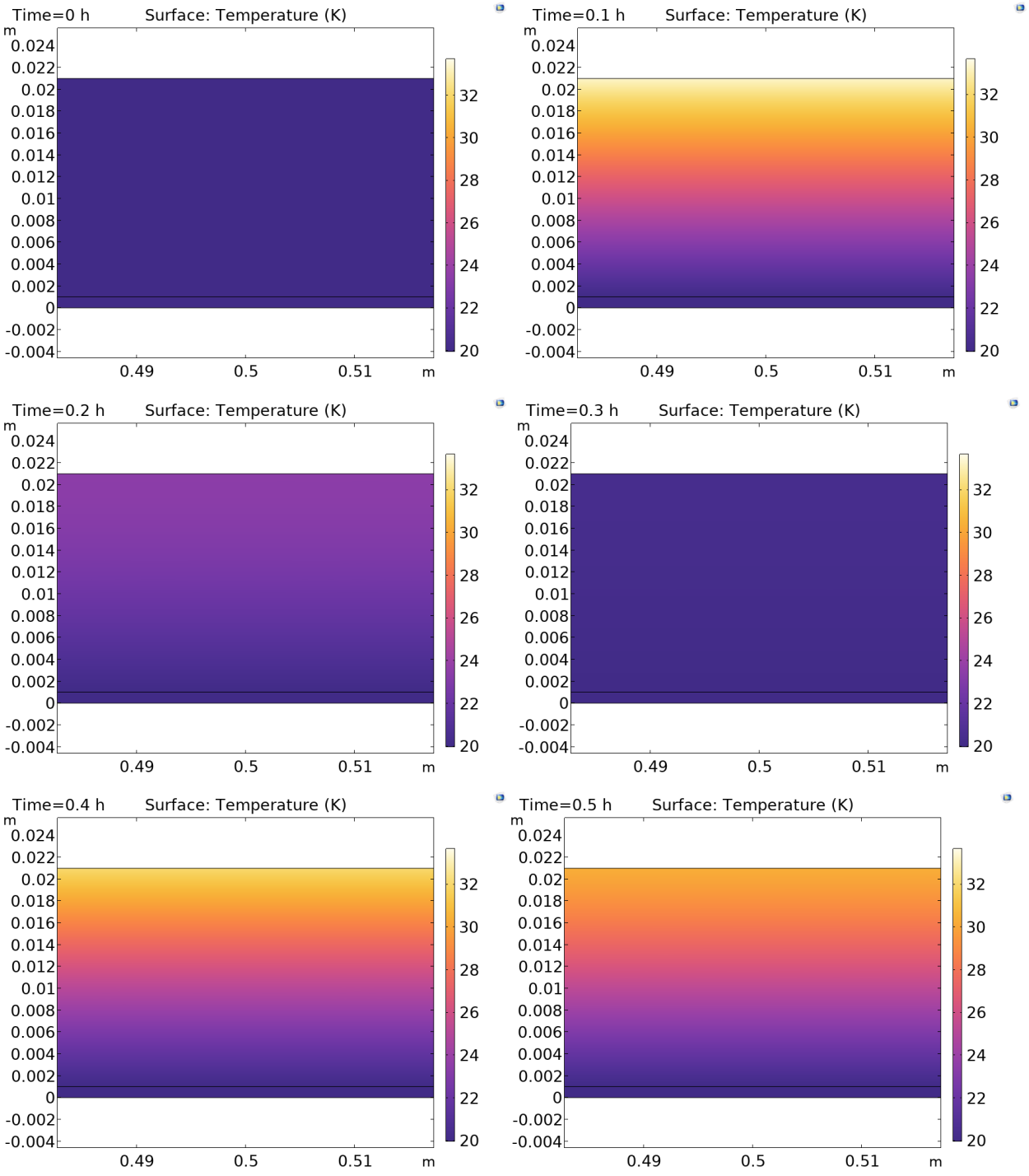

Figure 33: Temperature variation in wall for spinning spacecraft

2.3.2 Simplified Boil-Off Model

As discussed in section 1.1.2.3, the derivation of the change in mass of a cryogenic fuel storage tank is a heavily involved calculation requiring the consideration of many factors including radiative, conductive, and convective heat transfer, changing fluid properties at cryogenic temperatures, mass transfer at the gas-liquid surface layer, and mass flow out the nozzle of the propellant tank. The goal of the simplified model explained in this section is to determine how the mass of the tank changes with respect to time in the cryogenic tank, the assumptions made, and their supporting rationale.

2.3.2.1 Assumptions and Supporting Rationale

Multiple assumptions were required to simplify the model below in 2.3.2.2 to a solvable form for comparison between the use of different propellants and tank materials. The primary assumption made in this model was:

1. All energy imparted on the liquid goes into bulk boiling.

Due to this, it was also assumed that the bulk boiling conditions are met by the interior properties of the tank and that condensation and evaporation at the surface do not occur. This assumption is grounded in the second assumption:

2. The liquid temperature remains constant at its boiling temperature, $T_l = T_{boil}$

Here, it is assumed that the fluid starts at its boiling temperature and since the fluid temperature cannot exceed its boiling temperature, the temperature will remain constant throughout analysis. By already ignoring the presence of condensation and evaporation at the surface, s, the only additional potential mode of energy transfer across the surface is convective heat transfer, leading to the third key assumption that:

3. Convective heat transfer across the surface, s, is negligible compared to the heat transfer into the liquid node from the exterior wall.

As discussed in section 2.3.1, regardless of the changes in material properties, when a temperature boundary condition is applied to one side of the tank wall, the incident flux will

eventually equalize through the tank wall materials. With the consideration of rotating the spacecraft, it was found that the flux will equalize to $\dot{q}_{ex}'' \approx 31\ [W/m^2]$. Initial research and calculations for the convective heat transfer rate across the surface, s, indicated that within a margin of reason, the flux across the surface due to convection is negligible compared to the flux across the wall-liquid contact layer, and therefore the values of $\dot{q}_{ls}$ and $\dot{q}_{gs}$ are equal to 0 in the boil off model. Further discussion on this assumption is written in section 4.2.

Coupled together, these three assumptions allowed for the boil-off calculation to be simplified to the one represented by equation (24). All heat imparted upon the fluid contributes directly to boil off, therefore in equation (24), $\dot{q}'' = \dot{q}_{ex}'' \approx 31\ [W/m^2]$. Additional supporting assumptions are made. These assumptions and their supporting reasons are given below.

4. The gas pressure within the tank is constant, $P_g =$ constant.
    - A fundamental characteristic of the tank design proposed in this paper is that the tank pressure remains constant. The theorized continuous venting system in place is designed with the intent to keep the internal tank pressure constant.
5. Volumetric (V) temperature distributions within the gas and liquid nodes are uniform; $\frac{\delta T_l}{\delta V} = \frac{\delta T_g}{\delta V} = 0$
    - This bulk sum approximation allows the temperature of the liquid and gas phase to be considered uniform throughout each phase.
6. Mass transfer is only considered at the surface, s, and vent.
    - Ignore mass transfer out of the tank for auxiliary burns.
7. The gas phase is only composed of vaporized propellant.
    - Gas and fluid are composed of the same molecules; no ullage gas is considered.
8. The tank wall thickness is 1mm regardless of material type.
    - Preliminary calculations of the tank wall thickness based on the materials ultimate tensile stress yielded unrealistically low tank walls. 1mm is a valid assumption based on the manufacturability of aluminum or composite materials.
9. Any ΔV burns are instantaneous.

- The mass flow rate to the thrusters, $\dot{m}_T$, was therefore 0 throughout the analysis and the required propellant for a burn was subtracted instantaneously once the specific time, t, was met. This is supported by the fact that the time scale for a ΔV burn is significantly smaller than the mission duration.

While this model is not a perfectly realistic analysis of the mass lost due to boil-off in a cryogenic tank, based on the rationale explained above and the scope of this comparative analysis, it delivers a comfortably accurate estimation of this complex process. The achieved results offer a strong and consistent method to compare the use of LH_2 and LCH_4 in different tank design configurations. Furthermore, since it is considered that all heat imparted on the tank exterior directly contributes to bulk boiling of the propellant, this analysis can be considered a 'worst-case-scenario' of boiling and therefore the analysis conducted represents the extremes of boil-off calculations. In a real-world scenario, other factors and controls would be put in place to reduce the time the fluid spends in bulk boiling and maximize the condensation of propellant vapor back into usable propellant through active boil off mitigation techniques.

2.3.2.2 Simplified Spherical Propellant Tank Model

While the extensive boil-off model shown in Figure 7 is accurate, simplifications were required for the successful calculation of the propellant boil-off. More accurate modeling is beneficial in the long run, but diminishing returns in the value of a high-fidelity model were found based on the nature of this model's use being to compare tank configurations that vary only in selected properties. The final simplified model developed for this project is displayed below in Figure 34. The variable naming convention and definitions remain the same from Table 2.

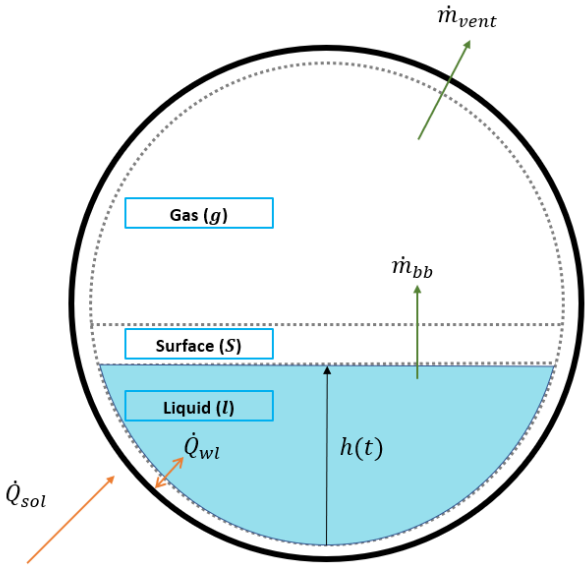

Figure 34: Simplified spherical tank boil off model

Where

Table 13: Simplified spherical tank boil ff model definition of variables

Variable	Value	Units	Definition
$\dot{m}_{vent}$	n/a	kg/s	Vent relief mass flow rate
$\dot{m}_{bb}$	calc.	kg/s	Propellant bulk boiling mass flow rate
$\dot{m}_T$	n/a	kg/s	Propellant liquid mass flow rate
$\dot{q}_{ex}$	31	W/m^2	Heat transfer rate from the external environment to tank skin exposed to liquid
$\dot{q}_{wl}$	$\dot{q}_{ex}$	W/m^2	Heat transfer rate between liquid node and tank wall exposed to liquid node
T_l	T_{boil}	K	Liquid temperature
V_l	calc.	m^3	Liquid volume

Based on the simplifying assumptions explained in the following section, the problem at hand reduces to an analysis only of the fluid phase. The boil off calculation is found through the bulk boiling formula given in section 1.1.2.3 as

$$\dot{m} = -\frac{Q * A(t)}{h_{vap}} \tag{24}$$

Where q'' is the total flux imparted upon the liquid node, with units of $[W/m^2]$; $A(t)$ is the surface area of liquid node, with units of $[m^2]$; and h_{vap} is the propellant enthalpy of vaporization, with units of $[J/kg]$. The additional key equations to this solution are the surface area and volume formulas for the liquid node. Due to the selected tank shape being a sphere, these values are represented geometrically as a spherical dome.

$$A(t) = 2\pi r h(t) \tag{25}$$

$$\mathrm{V}(t) = \frac{\pi \mathrm{h}^2(t)}{3}\big(3r - h(t)\big) \tag{26}$$

Furthermore, the key parameter that now relates the boil off rate to the liquid node properties is the height of the liquid in the tank at any given time t, as shown in Figure 34.

While the problem has been reduced significantly from the original model, the desired value of $\dot{m}$ cannot be solved for analytically. To find $\dot{m}$, an ODE of $\dot{h}(t)$ had to be found. This function was then numerically integrated with known initial conditions to solve for $h(t)$ and therefore $\dot{m}(t)$. To solve, $\dot{m}(t)$ was equated to $\frac{d}{dt}\big(m(t)\big)$, which are both functions of $h(t)$ and $\dot{h}(t)$. First, introduce the density formula based on the constant propellant density assumption.

$$\mathrm{V}(t) = \frac{\mathrm{m(t)}}{\rho} \tag{27}$$

Write $m(t)$ by equating equations (32) and (33)

$$m(t) = \left(\rho \pi \mathrm{r} h(t)^2 - \frac{\rho \pi h(t)^3}{3}\right) \tag{28}$$

Take the derivative of equation (45) with respect to t

$$\frac{d}{dt} m(t) = \rho\pi\left(2\mathrm{r} h(t)\dot{h}(t) - h(t)^2 \dot{h}(t)\right) \tag{29}$$

Therefore:

$$\dot{h}(t) = \frac{2q'' r}{\rho h_{vap}(h(t) - 2r)} \tag{30}$$

Given initial conditions, equation (36) was solved analytically in MATLAB

2.4 Final Design

In summary, the final spacecraft design chosen by the team consisted of four different spacecraft configurations: the first consisted of two spherical tanks, one filled with LH_2 and one filled with LOx, each made from AA 2024 and powered by one RL-10C-1 thruster. The second consisted of the same, except the tanks were made from Grafil 34-700 CFRP. The third configuration consisted of two spherical tanks, one filled with LCH_4 and one filled with LOx, each made form AA 2024 and powered by one M10 thruster. The final configuration consisted of the same, except the tanks were made from Grafil 34-700 CFRP These fuels were chosen as their differences in density, boiling point, and enthalpy of vaporization, all of which affected the spacecraft mass and rate at which heat propagates through the spacecraft and fluids.

A composite prepreg was purchased as opposed to a separate fiber matrix and resin, which would've needed to be combined via a resin transfer molding (RTM) process, due to project time constraints. This was the team's first time working with composite materials and having the prepreg ready resulted in fewer imperfections in the final product.

Additionally, each spacecraft is equipped with a CVS with an emergency vent valve. This allowed the team to assume that there is constant thrust during the coast period and that the propellant remained settled in the bottom of the tank for the duration of the mission. This system is designed to handle both expected and unexpected levels of heat flux. This venting system also contributes to reducing the boil-off.

Finally, all configurations were put in "*Barbecue Mode*" to reduce the peak flux entering the spacecraft and wrapped in MLI, which due to its low mass, emissivity, and thermal conductivity, reduced the magnitude of flux incident on the propellant tanks.

3 Experimental Approach, Results, and Discussion

After conducting background research, the team planned three experiments to validate the design choices for the chosen system. These experiments justify the information found in the literature review and were used to collect data related to our research.

3.1 Experimental Reasoning

The following sections discuss the reasoning behind each experiment and the value they bring to the project. Each experiment is relevant to the project and can generate data and validate design concepts.

3.1.1 Permeability Testing of Aluminum and CFRP Specimens

The permeability test was designed to analyze and compare the effectiveness of different lamina layups of carbon fiber specimens and compare these to an aluminum sheet, in mitigating gas permeation through the cryogenic tank walls. These results determined the efficacy of the CFRP laminates under the given operating pressure, as compared to the aluminum specimen. Two different Grafil 34-700 CFRP laminates (one 6-ply and one 8-ply) were tested in addition to a single AA2024-T3 aluminum sheet.

From the results of this experiment, the team was able to conclude in part if CFRPs are feasible for cryogenic tank construction, and compare its viability to aluminum's. If the laminates adequately mitigate permeability of hydrogen gas, then CFRPs can be considered a viable material choice for tank construction due to their increased strength, lighter weight, and reduced cost.

3.1.2 Venting Test of Simplified CVS Model

The venting test is designed to create a simplified model of the CVS and emergency venting valve. The team researched several types of venting systems, and among those, the CVS stood out its effectiveness in venting boil-off, contributing to the reduction of boil off, and allowing the assumption that the fluid in the tanks settles at the bottom of the tanks for the duration of the coast periods. Although this system is commonly used aboard spacecrafts, the team created a model to validate the fixed sized orifice calculations. If the boil off rate equals the

exit mass flow rate, a system in which pressurized air is added to the vessel can accurately model the real system.

Additionally, any spacecraft using a CVS needs an emergency relief valve in case the spacecraft experiences unexpected heat flux. Using a similar model to that shown in Figure 11, the team was able to test a simple code that can open and close the valve based on the pressure in the tank. These two tests allowed the team to prove that any boiled off fuel can safely and effectively be removed from the tank.

3.1.3 Heat Transfer Analysis of Tank Wall Layups

To help validate the design of our theoretical spacecraft, and to validate models produced in COMSOL, the team decided a physical test was required to see which tank wall layups managed the thermal load produced by radiation from the sun the best, which in turn would affect boil-off rates. Physical testing would be based on the simplified models created in COMSOL, of a small section of tank in which solar flux is applied to one side of the specimen, the temperature of the opposing side is held constant, and all other physical boundaries are insulated. This setup allowed the team to see how heat transferred through the material in a situation like a wall of a cryogenic tank. This came with some challenges, as the team had to come up with ways to create these boundary conditions in an experimental setup, so physical testing could be an accurate representation of the computational models, and analogous to the conditions experienced by propellant tanks containing cryogenic fluids in the vacuum of space.

3.1.4 Computational Determination of Boil-Off Rates

While not a physical experiment, a MATLAB script was built to numerically determine the amount of fuel and oxidizer lost to boil-off in each configuration. This was done by iteratively solving the model and ODE presented in section 2.3.2.2 with the design choices and corresponding specifications and formulas in section 2.2. Using these relationships, the team was able to use the known properties of our chosen propellants and tank materials to determine the amount of propellant lost to boil-off, and how each factor affected the boil-off rate. The setup and method for solving this process is described in detail in section 3.2.5.

3.2 Methods and Procedure

The following sections discuss the methods used to perform each experiment. Further detailed methods and instructions can be found in the appendix. Each experiment was conducted following proper safety precautions and wearing appropriate protective equipment.

3.2.1 Methods and Procedures for Composite Curing

Prior to testing, the Grafil 34-700 carbon fiber prepreg was cured. This process begins with preparing the prepreg before it is placed in an oven for curing. Since the prepreg was manufactured as a roll, it must be cut into appropriate measurements and then stacked together according to the lamina layup sequence chosen. Once this is complete, the laminate will be placed on an aluminum plate, which will act as the mold plate, since the team is currently interested in creating a flat composite plate. This plate, with the prepreg, will then be placed in a vacuumed bag.

Figure 35 and Figure 36 illustrate the vacuum bag apparatus.

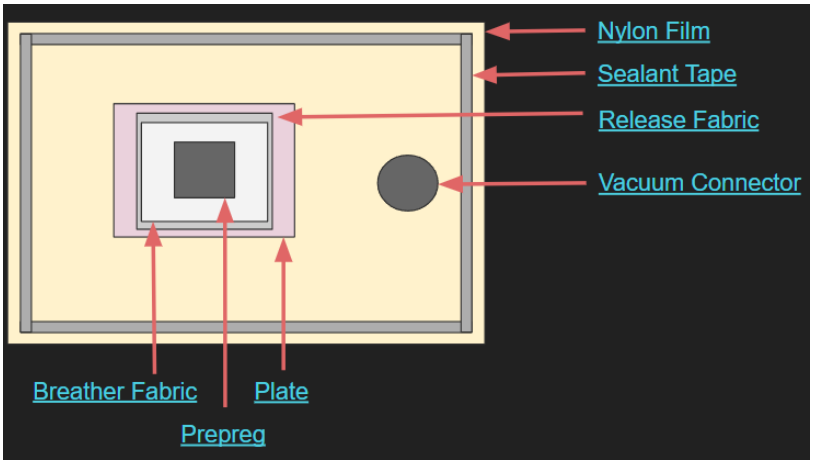

Figure 35: Top view of vacuum bag apparatus. Note these dimensions are not to scale.

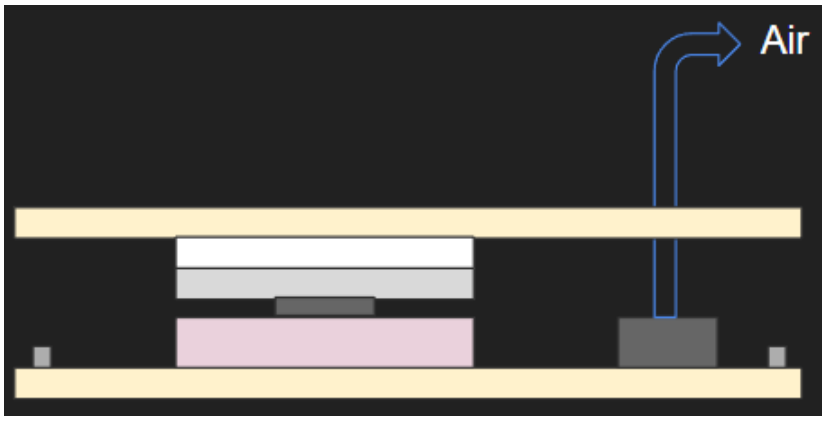

Figure 36: Side view of vacuum bag apparatus. Note these dimensions are not to scale.

The process continues with placing the vacuumed bag apparatus into a curing oven where the composite will be cured. According to manufacture curing instructions, this is a standard 250°F cure profile. The curing instructions are as follow:

1. Full Vacuum bag pressure for entire cure cycle. Autoclave, if possible, up to 100 psi, min 40 psi
2. $5^{\circ F}$ per minute ramp rate (do not pre-heat the oven)
3. $250^{\circ F}$ hold for 120 mins after part reaches $250^{\circ F}$ (sometimes the part lags the oven temperature)
4. $5^{\circ F}$ per minute cool down rate (leave in oven and let it cool down slowly)
5. Keep under vacuum until part temp reaches $130^{\circ F}$ min.

Once the composite is fully cured, it is ready for the permeability testing which will be discussed in the next section. See section 6.1 for complete, step-by-step instructions for the composite preparation and curing which were discussed in this section. A picture of the vacuum sealed composite is shown below

Figure 37: Vacuum sealed bag of 6-ply composite material prior to being oven-cured.

3.2.1.1 Safety Practices

Composite materials should be handled with utmost caution, as there are hazards associated when handling these types of materials. Microfibers from the composite and resin being used in this experiment can cause irritation and abrasion internally and externally if they come into contact with skin, eyes, and lungs. Repeated contact with the resin in the prepreg may cause dermatitis. Cured composites are likely to contain fiber splinters around the edges, which can cause lacerations. Additionally, dust can be generated from composites, typically from manufacturing cure components, which may have severe consequences if ingested.

Due to the risk of handling composite materials, standard OSHA protocols were in place and followed by all team members. Safety measures include utilization of personal protective equipment (long clothing to mitigate skin exposure, thick gloves, eye protection, respiratory protection) and using the oven in an isolated, well-ventilated area. Additionally, a minimum of two team members were present when working with the composite as an extra safety precaution. For a more detailed explanation of OSHA safety information and guidelines, please reference OSHA Section III: Chapter 1 and OHS, 2021, or section 6.1.

3.2.2 Methods and Procedures for Permeability

Once the composite laminates are cured, they are ready for testing. There were three individual sets of permeability tests done on three separate specimens. Gaskets will be put on the

inside surfaces of the metal sheets which will be in contact with the specimen to ensure a tight seal for testing. Eight ¼-inch bolts and nuts will be used to secure the specimen between the two plates. Two male NPT nipple fittings will be secured to the center of the top and bottom aluminum plates. A Teflon tube from a compressed air supply tank will then be connected to the inlet of a pressure regulator with a pressure gauge secured to it which reads the downstream pressure of the pressure regulator. A Teflon tube will be connected to the outlet of the pressure regulator to the NPT fitting on the bottom plate to supply pressure to the specimen.

A liquid water slug will then be introduced into a "U" shaped Teflon tube with both ends of the tube open to the atmosphere and will settle at the bottom of the "U" shape. It is best to use a syringe to inject the water into the tube to prevent bubbles being trapped in the fluid. The height of the water on either side of the tube should be the same. The tube will be taped to a board to keep it in place. A ruler will be placed next to the tube to measure the water displacement in the tube. One end of the tube will be left open to atmospheric pressure while the other will be connected to the NPT nipple fitting on the top aluminum plate. This setup will function as a monometer for the permeability experiment. Figure 38 illustrates the general concept of the permeability testing apparatus.

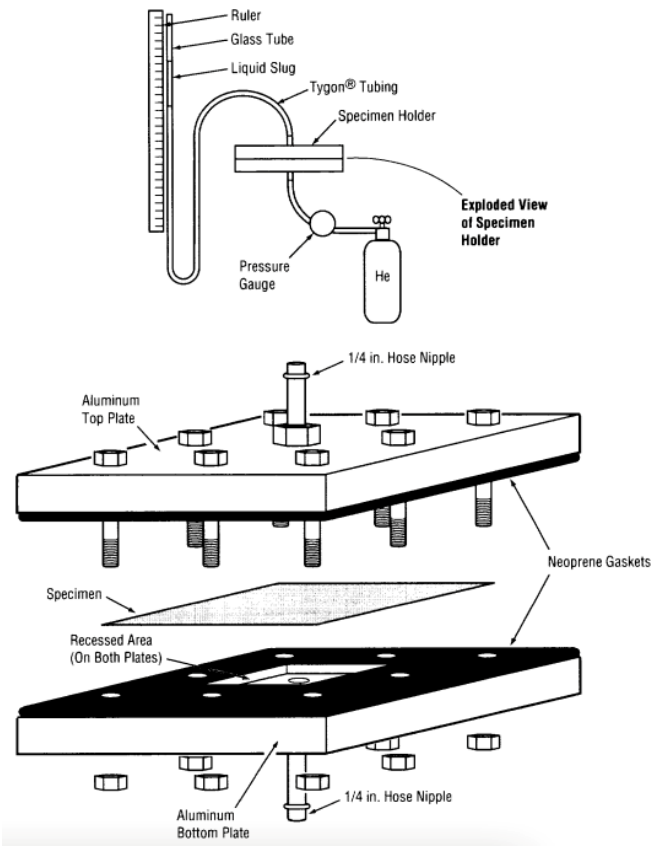

Figure 38: Permeability testing apparatus (NASA, 2001)

The best way to connect the apparatus with compressed air was using a ball valve, a pressure regulator, and a pressure gauge. The pressure gauge and pressure regulator were used to vary the pressure being tested against each specimen, and to read what that pressure was. Therefore, mass flow rate data that was collected was able to be analyzed depending on specific pressures. The ball valve was used to facilitate the setting of the pressure, and the starting and ending of data recording. Figure 39 shows the complete permeability testing apparatus.

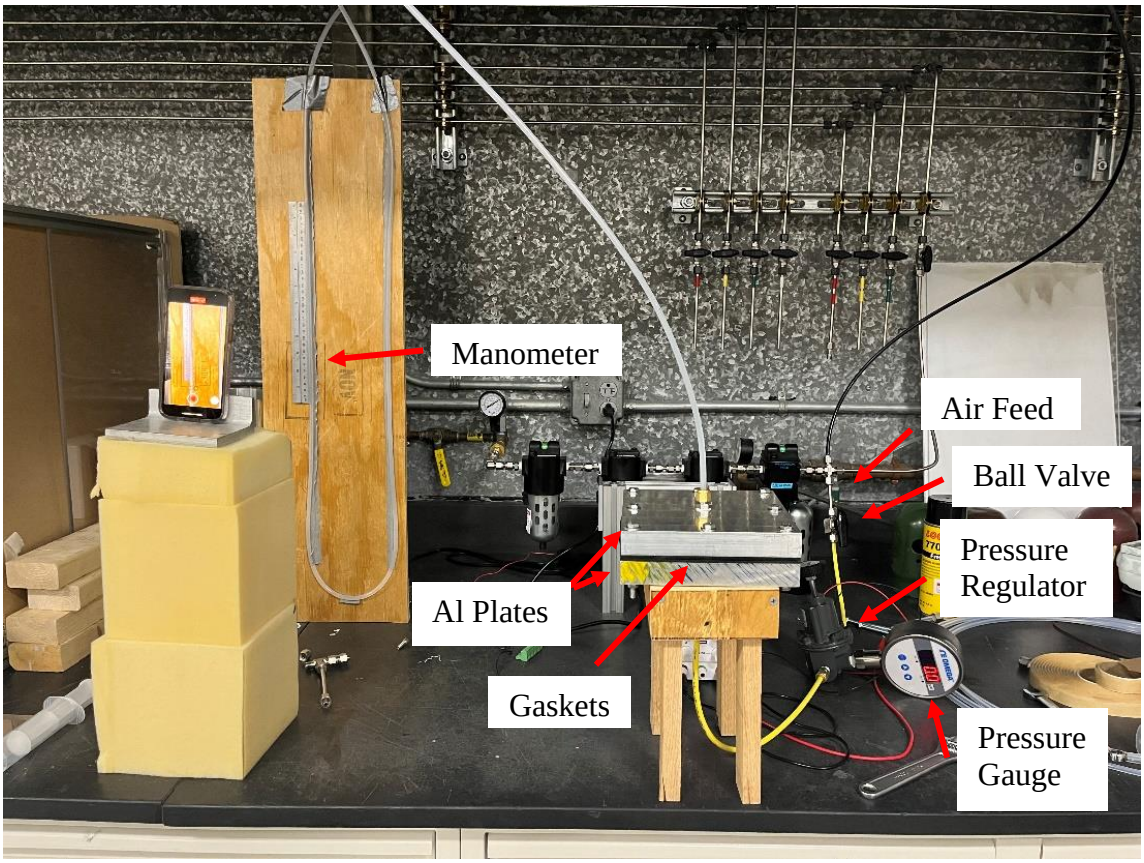

Figure 39: Permeability experimental testing apparatus.

3.2.2.1 Mass Flow Rate Derivation

This testing procedure is designed to determine how much gas passes through the specimen. This was done by measuring the displacement of the water in the manometer when gas pressure is applied on one end of the specimen. This causes a pressure differential on each side of the water in the manometer as gas permeates the specimen, resulting in displacement of the fluid. Since the pressure difference across the specimen is too large to be balanced by the liquid column height in the current apparatus, the balancing of the pressure forces on either side of the manometer was not observed (i.e. the liquid column was continuously displaced throughout the data collection period). The data was collected via video recording and was used to determine mass flow rate of the gas through the specimen (permeability). The derivation is as follows.

Beginning with known equations of force, pressure density, and volume of a cylinder, the pressure can be related in terms of fluid displacement in the manometer.

$$F = mg \tag{31}$$

where m is mass of the gas permeating through the fluid, and g is acceleration due to gravity

$$P = \frac{F}{A_{cricle}} \tag{32}$$

Where A is the area of a circle,

$$\rho = \frac{m}{V_{cylinder}} \tag{33}$$

Where $V_{cylinder}$ is the volume of a cylinder,

$$V_{cylinder} = A_{circle}h = \pi r^2 h \tag{34}$$

Where h is the fluid displacement in manometer. Combining equations (31)-(34), pressure was determined from the fluid displacement in the manometer as:

$$P = \frac{mg}{A} = \frac{\rho V_{cylinder} g}{A} = \frac{\rho A_{circle} hg}{A} = \rho hg \tag{35}$$

Simplifying equation (35) further:

$$\frac{mg}{A} = \rho hg \tag{36}$$

Which can be rearranged as:

$$m = \rho Ah \tag{37}$$

However, to determine mass flow rate, both sides of equation (37) were divided by the time, t, over which the data was collected. This can be seen in equation (44) below:

$$\dot{m} = \rho Av = \rho(\pi r^2)\left(\frac{h}{t}\right) \tag{38}$$

From equation (38)**Error! Reference source not found.**, it can be interpreted that the factors that will affect the mass flow rate of the gas through the specimen are the density of the fluid and the inner radius of the Teflon tube. A visual of the displacement of the fluid in the manometer is illustrated in Figure 40.

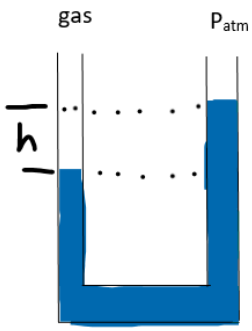

Figure 40: Displacement of a fluid in a manometer.

3.2.2.2 Henry's Law Calculations

Another factor relevant to the manometer is Henry's Law, which states the amount of gas dissolved in a liquid is directly proportional to the partial pressure of the gas above the liquid when temperature is kept constant. Since either side of the fluid in the manometer is exposed to gas pressure Henry's Law must be considered. Henry's law is only applicable when molecules are in equilibrium at low pressures, which is why it was accounted for in this project. To determine how much O_2 gas would dissolve in 20 mL of water at 20°C the mole fraction of O_2 gas dissolved in water the following equation is used:

$$P_{O2} = X * K_{H,O2} \tag{39}$$

where X is the concentration of the dissolved gas, and $K_{H,O2}$ is Henry's law constant of the gas. It is known that the partial pressure of O_2 at 20°C is 0.00023 kbar, and Henry's law constant is 34.86 kbar. Substituting these values into equation (39), the concentration of the dissolved gas is found to be $6.1102 * 10^{-6}$. Next, the volume of water must be converted to moles. It is known that $20\ \text{mL} = 20\ \text{g}$. Dividing this mass by the molar mass of H_2O (18.016 g/mol), the moles of water are found to be 1.1101 moles. Finally, by multiplying the concentration of the dissolved gas by moles of water, the amount of gas that would dissolve in water at the given conditions is found to be $6.78 * 10^{-6}$ moles. Following the same procedure, the amount of N_2 gas that would dissolve in water at the same conditions can be found. Knowing that $P_{N2} = 0.001013$ kbar and $K_{H,N2} = 76.48$ kbar, the amount of N_2 gas that would dissolve in water is $1.47 * 10^{-5}$ moles.

3.2.3 Methods and Procedures for Venting

This test was a proof-of-concept experiment designed to validate our chosen venting system. The system was designed to vent the gas at the same rate it boils off, so an orifice had to be properly sized and designed to allow the pressure to remain constant in the tank. This experiment was used to determine whether our calculation method was effective in determining orifice size. The tank was modeled by a three-gallon pressure vessel and the boil-off was modeled by pressurized air from an input valve. A sonic nozzle and a pressure regulator were used to control the mass flow rate into the tank. This allowed the mass flow rate to remain constant, which provided an accurate representation of the boil-off expected in an actual tank. The flow out of the tank was through a fixed-size orifice, with the area calculated using the tank pressure and input mass flow rate. A pressure sensor was also attached to the tank to monitor the pressure throughout the experiment. The expected result was that there will be no change in the tank pressure throughout the experiment. The experimental setup is shown below:

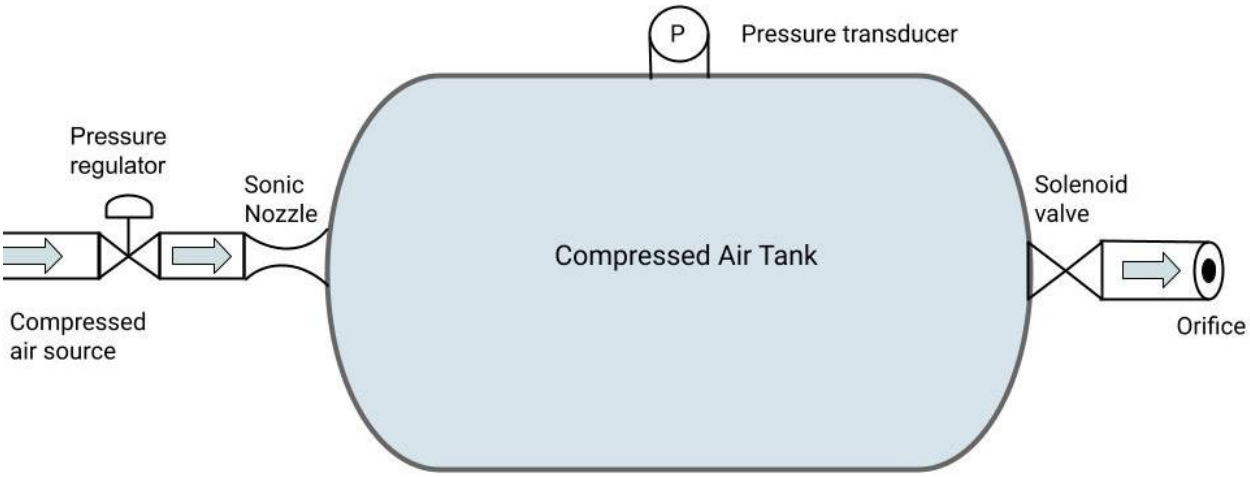

Figure 41: Diagram of the venintg system experimental setup

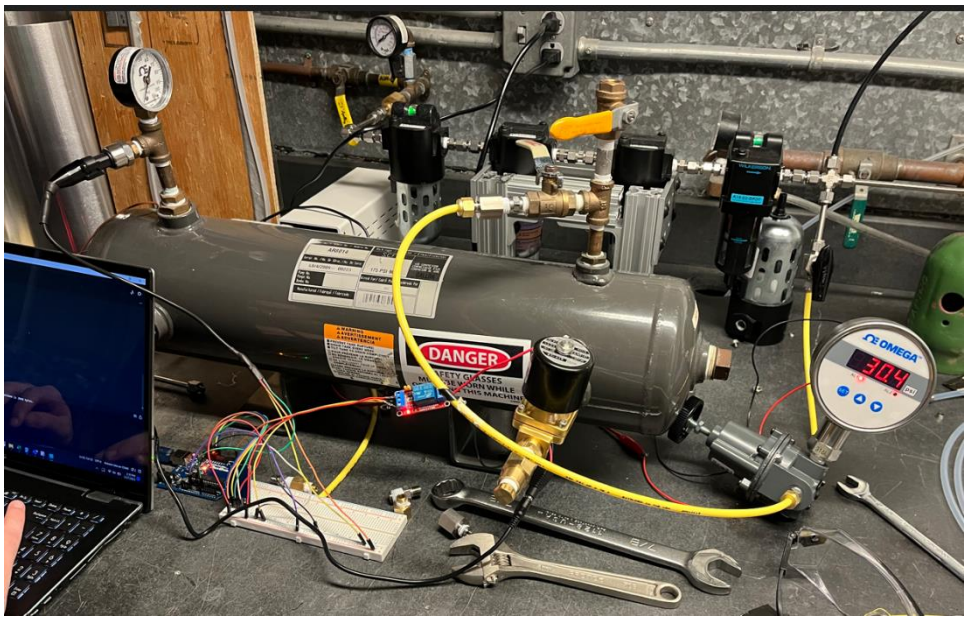

Figure 42: Venting system experimental setup

We designed the experimental setup to maintain a pressure of 30 psia (15 psig) in the compressed air tank. The tank vented into standard atmospheric conditions resulting in a ratio of back pressure to tank pressure of approximately 0.4899. Based on tabulated isentropic flow data, for a pressure ratio less than 0.5283, the flow will be sonic, so we can assume that there will be choked conditions at the orifice during the CVS experiment. Similarly, since a cryogenic spacecraft tank vents into the vacuum of space, the pressure ratio will be low enough for choked flow at the orifice. Because of this, we could use the following equation to calculate the orifice area, or A*, given the fixed mass flow rate of the sonic nozzle, the properties within the tank and the properties of air.

$$\frac{\dot{m}}{A^*} = \frac{P\gamma}{\sqrt{\gamma RT}}\sqrt{\left(\frac{2}{\gamma+1}\right)^{\frac{\gamma+1}{\gamma-1}}} \tag{40}$$

Using this equation (where γ is the ratio of specific heats, R is the specific gas constant, P is the tank pressure and T is the tank temperature) the team calculated an orifice diameter of 0.038 inches from the A* value. We then purchased the correct orifice size from a commercial supplier. The equation above was also used to calculate the mass flow rate into the tank through the sonic nozzle.

A secondary experiment was conducted with the same setup as the previous test, except with a solenoid valve in between the tank and the orifice. To control this valve, an Arduino microcontroller was used. This microcontroller took readings from the pressure transducer and simply opened and closed the valve based on a preset pressure parameter. To ensure the pressure transducer output proper values, it had to be calibrated, through using an analog pressure gauge to set the pressure at known values and reading the voltage output by the sensor. Lastly, a relay would be used as a digital switch to control the state of the valve. The script created to run this is shown in Appendix 6.6. All these aspects would come together to serve as a proof-of-concept experiment to test the emergency venting system.

3.2.4 Methods and Procedures for Heat Transfer

To set up the apparatus for thermal testing, each subsystem was constructed outside the vacuum chamber individually, to allow for easy implementation when the team began testing. The following pieces were constructed, a cooling plate, a heat lamp apparatus, feedthroughs were wired, and a surface plate was made to set all needed items onto inside the chamber. These items together created the boundary conditions the team sought to achieve when modeling cryogenic tanks.

3.2.4.1 Cold Plate Design and Assembly

The first boundary condition worked on was the requirement for a constant temperature on the cold side of the specimen. The team went through multiple iterations on this, but the finalized design used a Peltier cooling device. This device is a component that runs on a 12-volt D.C. current, and when applied moves heat from the “cold side” of the device to the “hot side”. Figure 43 shows a typical Peltier cooler.

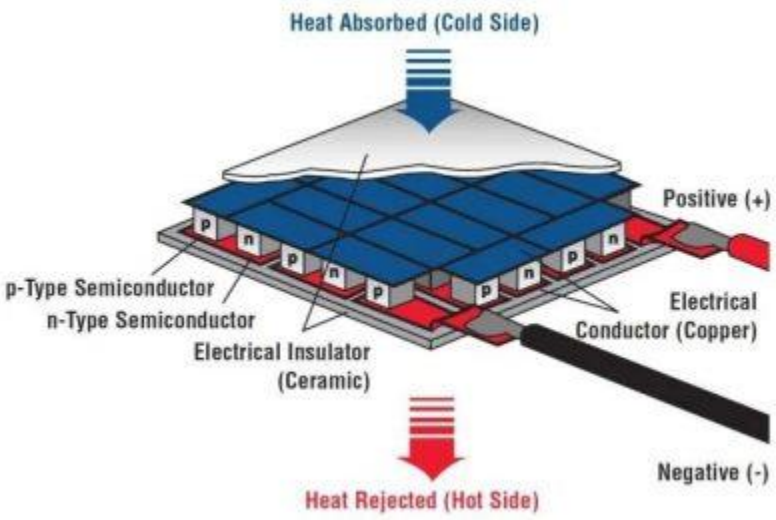

Figure 43: Diagram of a Peltier cooler and its parts (Wellen Tech, n.d.)

This creates a temperature differential across the device and using a type K thermocouple attached to the cold side of the Peltier cooler, the voltage applied can be controlled (code used is in Appendix 6.4) to keep the temperature constant. The team also had to consider how to keep the device from overheating, as if the excess heat on the hot side is not taken away in some manner, the effect of the Peltier would be significantly diminished. A CPU radiative cooler was used to mitigate this issue. By attaching a piece of aluminum to the top of the device and using the mounting system of the cooler, a cold plate was created to allow for a surface for the specimens to rest on during experimentation. The complete apparatus is shown in Figure 44.

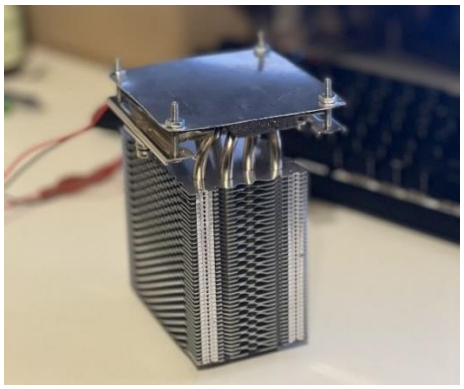

Figure 44: Complete cold plate apparatus

3.2.4.2 Heat Lamp Apparatus

The next boundary condition designed was in relation to creating a source of radiation that would impart a flux onto the hot side of the specimen itself. This is accomplished by using heat lamps, which would use an applied electrical current to create a traditional source that could be controlled. Fortunately, a previous MQP, Design and Analysis of an Interplanetary SmallSat ((Mayer et al., 2021), had built something similar, allowing us to use the same components. The bulb used was a 250R40 bulb. An apparatus of extruded aluminum would be used to hold the lamp in place above the specimen. Figure 45 shows the completed lamp apparatus. These lamps would be controlled by a variable potentiometer that would allow for the bulbs to be dimmed to a certain percentage of their full capability at 500 watts total.

Figure 45: Heat lamp apparatus

3.2.4.3 Heat Lamp Bulb Calibration and Verification

Fundamentally, a radiation source has multiple characteristics, which can change how the given radiation can interact with matter. Flux is a topic of much discussion in this paper, and in thermal testing, the goal was to heat lamps to create this flux. Heat lamps can generate flux at a variety of wavelengths. Documentation on the bulbs used in our apparatus was limited, so any spectral output was not known. Also, the team originally had to estimate the thermal power of the bulbs as a fraction of its electrical input, based on the fact that a typical halogen bulb (the type of bulb used) converts about 90% of its electrical input into thermal energy. To characterize the bulb, the team used a FLA5000 spectrometer. This showed the wavelengths produced by the bulb and the flux at said wavelengths. Then the area under the curve made by this spectral graph represents the total flux.

This opportunity also gave the team the ability to see how the flux changes with varying distances between the bulb and the specimen, along with how the angle of the bulb affected the total flux as well. In the figure below, the testing apparatus is shown.

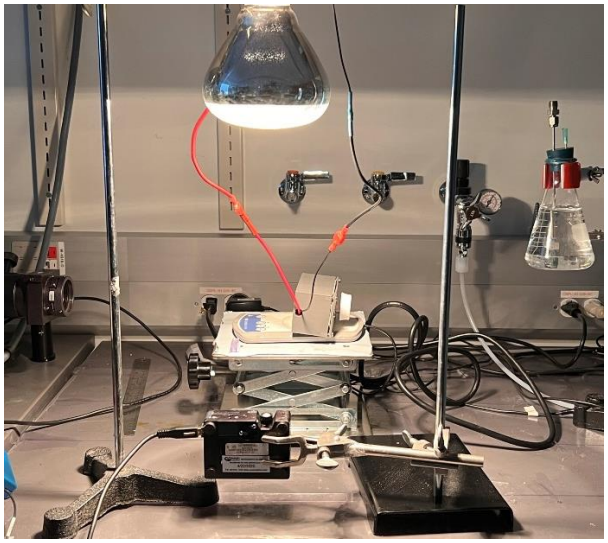

Figure 46: Spectrometer testing apparatus

3.2.4.4 Vacuum Chamber Feedthroughs

To exclude all effects of convection, and recreate an environment similar to that in space, this apparatus created above would be installed in a vacuum chamber. This would only allow for heat transfer to occur through radiation and conduction, as would be the same in a space

environment. This created some challenges for the team to overcome. The biggest being the supply and acquisition of power and data. A power source or data acquisition unit could not be put inside the vacuum chamber, so a set of pass-throughs were needed. These would allow for power and thermocouple data to be sent in and out of the chamber as it was under a vacuum. These were sourced from Kurt J. Lesker and the two acquired are shown in the figures below.

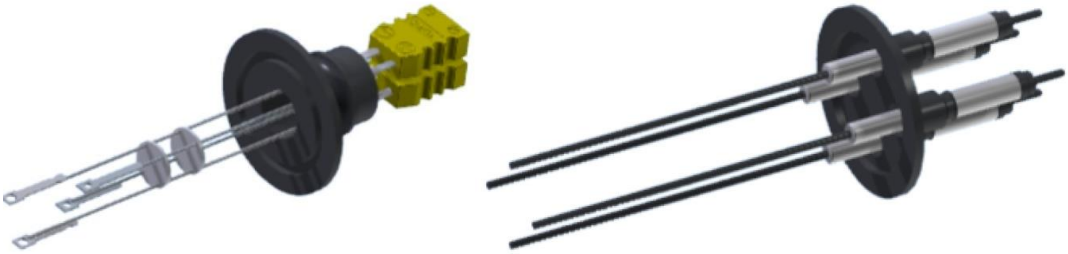

Figure 47: Thermocouple and power feedthroughs (Lesker, 2023)

This would also allow for the heat lamps to be connected to the required external power source, and an Arduino microcontroller would be able to display and record temperature data collected inside the chamber.

3.2.4.5 Data Acquisition and Wiring

As stated above, an Arduino microcontroller was used to collect temperature readings. This was done by using multiple different modules. An Arduino Nano was used as the main microcontroller. To read values from the thermocouple properly two MAX6675 thermocouple modules. These would allow the Arduino to properly interface and read the voltages created by the temperature of the probes. The final module was an SD card module. This would simply allow for the Arduino to write the two measured temperature values and the time when these values were recorded. Bringing all this hardware together was a script created to accomplish the outcomes needed. This script can be found in section 6.4. Figure 48 shows a diagram of the wiring of the entire apparatus.

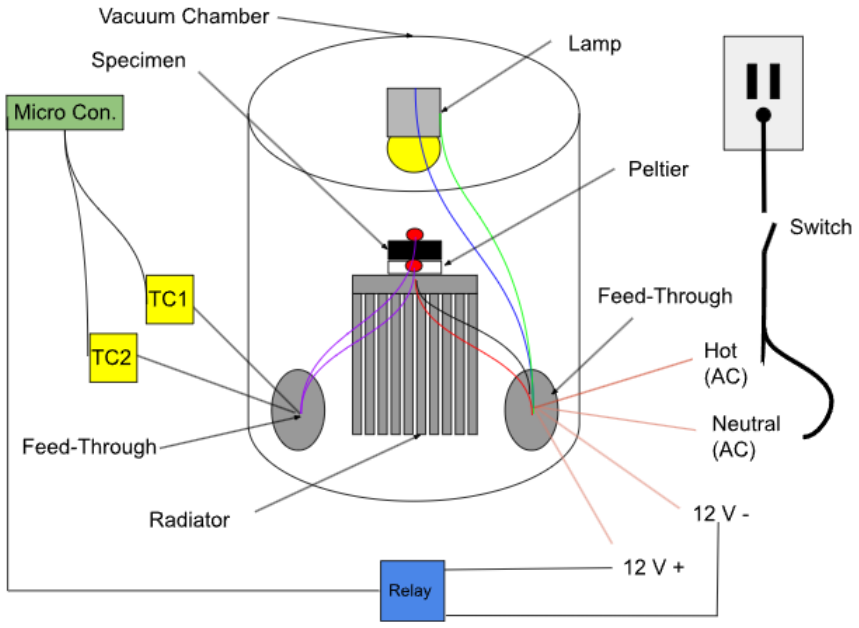

Figure 48: Thermal testing apparatus wiring diagram

With the apparatus setup complete, the team was now ready to conduct experiments. The procedure used is outlined in section 6.3. In summary, specimens would be put onto the cold plate and into the vacuum chamber. A vacuum would then be pulled, heat lamps and cold plate would be turned on, and data collection would begin. The team monitored the temperatures of the hot and cold sides of the specimen, ensuring the cold side stayed at a constant temperature and waited for the temperature of the hot side to equalize. Once this was done, the test could be concluded.

3.2.4.6 Thermal Testing Analysis

With the data collected on hot side and cold side temperatures, for AA-Mylar and AA-Foam-Mylar specimens, the team was able to determine if these values were accurately represented in comparable COMSOL simulations. This was done by comparing the difference in temperature between each side and seeing if the trends and magnitudes of the experimental data were comparable.

3.2.5 Methods and Procedure for Computational Determination of Boil-Off Rates

To determine the boil-off rates of LH_2, LCH_4, and LOx in each configuration the team compared the amount of energy remaining in each tank after the execution of the trans-earth

injection. This provided a consistent and fair baseline to compare all propellant and tank material combinations to, and showed how the team's choices in propellant and tank material affected the boil-off rates of said propellants.

The trans-earth injection was chosen as, at this point, no more propellant is required to send the spacecraft back to Earth. As a result, there should be zero fuel and oxidizer left in each tank. However, having no propellant left leaves no room for error, and Apollo-style missions require contingency upon contingency to ensure the safety of the crew and onboard supplies. Therefore, the baseline energy was chosen to be $\Delta V = 100 \frac{m}{s}$ and a fuel mass equal to 1% of the initial fuel mass to strike a balance between minimizing the onboard propellant, and therefore mass, after the final burn, while ensuring enough propellant is left over as a contingency factor.

To numerically compare the energy in each tank at the baseline criterion, a MATLAB script (detailed in section 6.7) was created, which iteratively solved the model and ODE presented in section 2.3.2.2**Error! Reference source not found.** with the design choices, corresponding chemical and material properties, and formulas described in section 2.2, given a propellant mass and oxidizer to fuel (O:F) mass ratio.

The specific details of the MATLAB script can be found in section 6.7, which includes numerous comments on the setup and workings of the script. To obtain meaningful outputs from the script, all that needs to be controlled are the initial propellant mass range and O:F mass ratio – these inputs control the amount of propellant and corresponding chemical energy left in the cryogenic tanks. While both inputs affect both outputs, changes in the propellant mass have the greatest effect on the total amount of ΔV remaining, and changes in the O:F ratio have the greatest effect on the percentage of fuel and oxidizer remaining in the tank. Therefore, one should iteratively tune these parameters to find an initial propellant mass and O:F ratio that meet the baseline criterion. This process is visualized below in Figure 49.

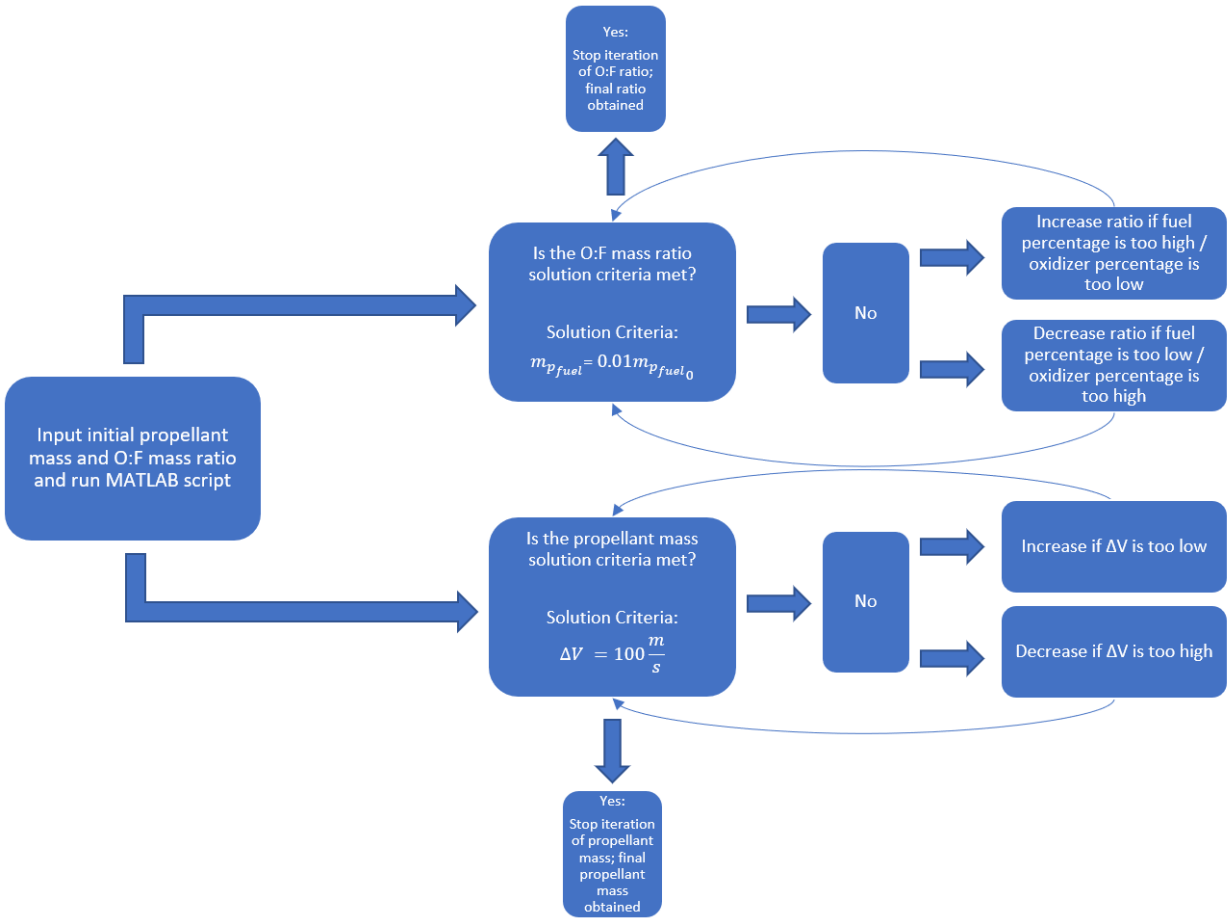

Figure 49: Flow chart for numerical determination of boil-off rates

3.3 Experimental Results

This section details the results of the experiments and their implications in constructing cryogenic fuel tanks capable of effectively mitigating boil-off.

3.3.1 Permeability Test Results

The permeability of three specimens were tested using the permeability set-up described in section 3.2.2, see Figure 39 for reference. The first specimen tested was a sheet of Al 2024. The second was a CFRP composite with 6 sheets stacked in alternating 0º and 90º fiber orientations (CFRP-6). The third was another CFRP composite stacked in alternating 0º and 90º fiber orientations, but with 8 sheets instead (CFRP-8). A table of the parameters for the specimens is shown below in Table 14. Note the three specimens have different dimensions. In

order to compare these parameters more accurately, the length and width of the CFRP-6 and CFRP-8 specimens were scaled to match the Al 2024 test specimen using simple ratios. The mass for the composites were scaled correspondingly as well. The scaled values can be seen in Table 15. These measured values will be compared with the mass flow rate results at the end of this section.

Table 14: Mass and dimensions for the respective composite and aluminum specimens.

	CFRP-6	CFRP-8	Al 2024
Mass (g)	9.716	25.973	28.675
Dimensions (mm)	90 x 90 x 1.02	120 x 120 x 1.3	103 x 103 x 1.15

Table 15: Mass and dimensions for the respective composite and aluminum specimens with constant lengths and widths.

	CFRP-6	CFRP-8	Al 2024
Mass (g)	12.726	19.135	28.675
Dimensions (mm)	103 x 103 x 1.02	103 x 103 x 1.3	103 x 103 x 1.15

It is important to consider the size of these sheets when considering their respective mass. The CFRP-8 was larger than the aluminum specimen, still with a reduced weight. A picture comparing the two specimens is shown in Figure 50; the shiny aluminum plate is laid on top of the black CFRP-8 to show the difference between the two sizes. Also note the square shape on the aluminum plate, this was from the gasket that the plate was sandwich between in the permeability apparatus.

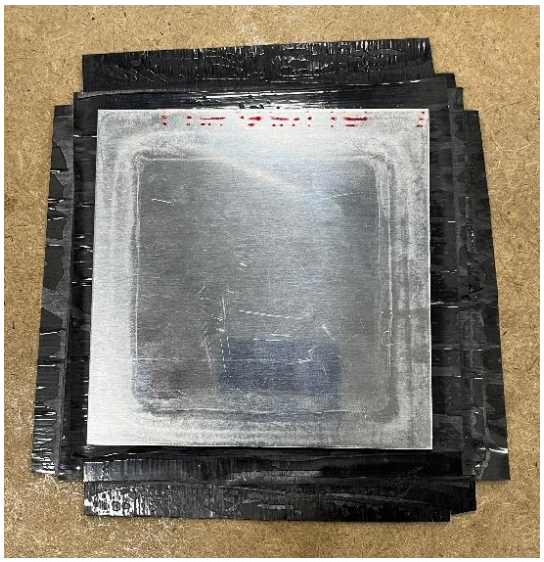

Figure 50: Comparison between CFRP-8 and AL 2024 test specimens sizes.

The method for data analysis followed the steps used in section 3.2.2.1 in order to find a mass flow rate. First, a pressure was set, and a camera was used to record the height of the liquid in the manometer for over 10 minutes. The height data points were recorded in 1-minute intervals and recorded in a table. The total change over 10 minutes was found. Using equation (38), the mass flow rate for each pressure test was found. The manometer height data collected for the Al 2024 test specimen is summarized in

Figure 51 and Figure 52. It can be seen in

Figure 51 that there is an initial spike in fluid height within just a few seconds after testing begins, after which the fluid height increases at a very slow rate. The spike in the manometer height is depicted by the second zero on the x-axis; zero was chosen since the time for the spike was very small, but not that this is not negligible. This spike was seen during testing of all specimens at all tested pressures. It is possible that the spike was caused by the deformation of the specimen when pressure is applied to one side, which could have decreased the volume on the other size of the manometer. The height after the spike increases at a slow rate, as shown in the plots below.

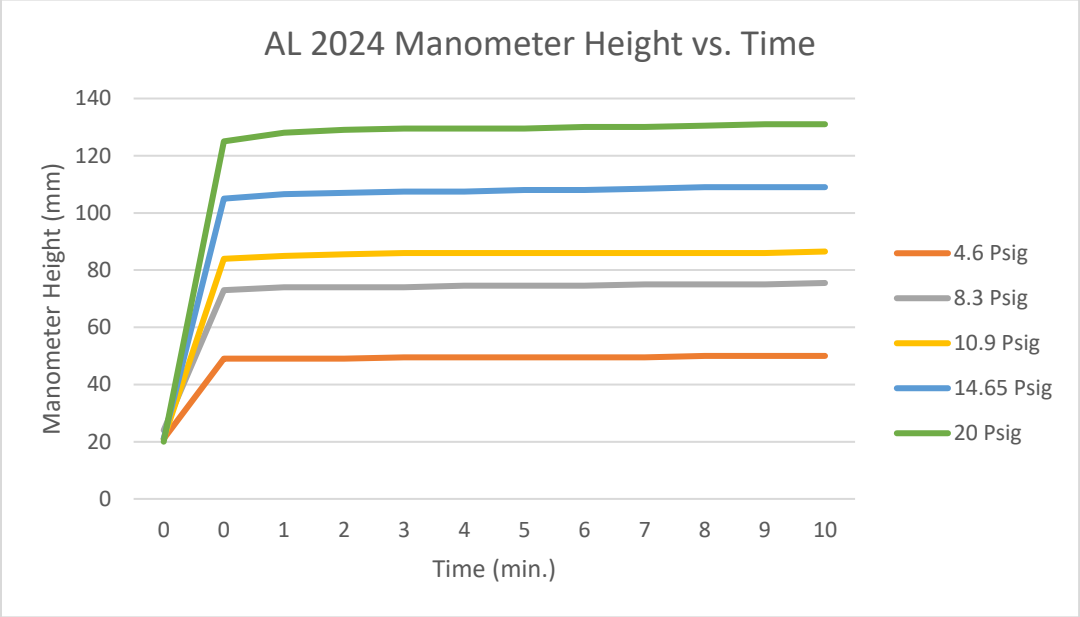

Figure 51: Displacement in manometer fluid height during Al 2024 permeability testing. Note the initial spike in the fluid height.

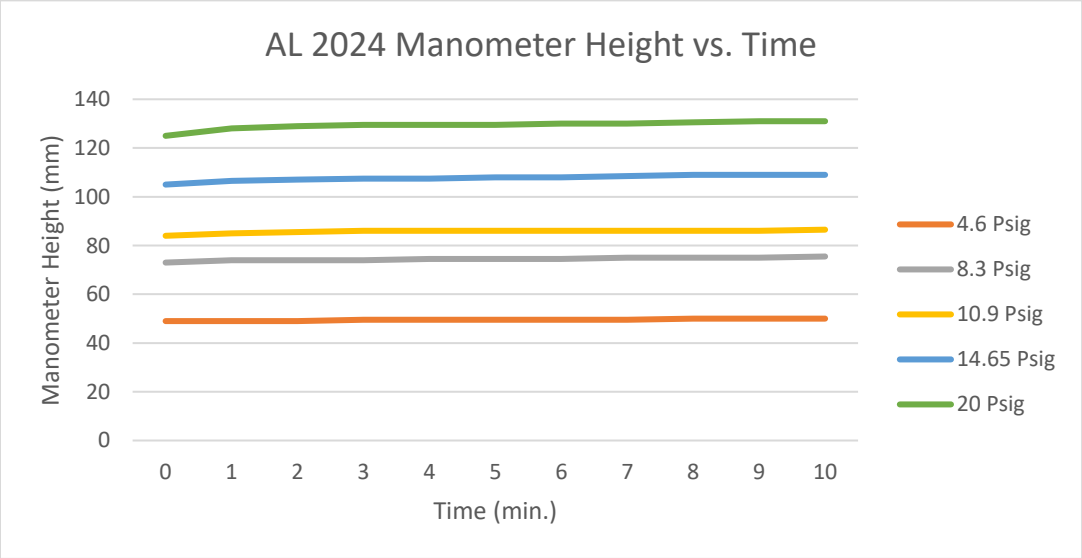

Figure 52: Displacement in manometer fluid height during Al 2024 permeability testing after the initial spike in the fluid height.

Using the manometer data collected and determining the density of the air for the various pressures the Al 2024 was tested at using tabulated values from engineeringtoolbox.com for 70ºF (temperature of the lab), the data was inputted into equation (38) to determine the mass flow rate of compressed air through the specimen at each tested pressure. Note that only the data collected

after the initial transient was used for the calculations (i.e. data shown in Figure 52). The inner radius of the tube was 4.25 mm (about 0.17 in). The results are presented in Figure 53. From the dotted trendline plotted, the mass flow rate of air increases at a rate of 0.0037 kg/min. with increasing pressure. There is also a strong correlation between the data collected and the trendline which suggests reasonable data was collected from our experiment. From equation (38) it can be understood if the inner radius of the manometer tube is kept constant then the mass flow rate should increase linearly with pressure, which is what is observed in the experiment as well.

The average permeability of hydrogen in alloys is to the magnitude of 10^{-4} kg/s (Marchi, 2006). Seeing as how the density of compressed air is greater than that of hydrogen, one can conclude that the permeability of compressed air through a specimen would be less than hydrogen. Our data supports this assumption, with a mass flow rate to the magnitude of 10^{-5} kg/min.

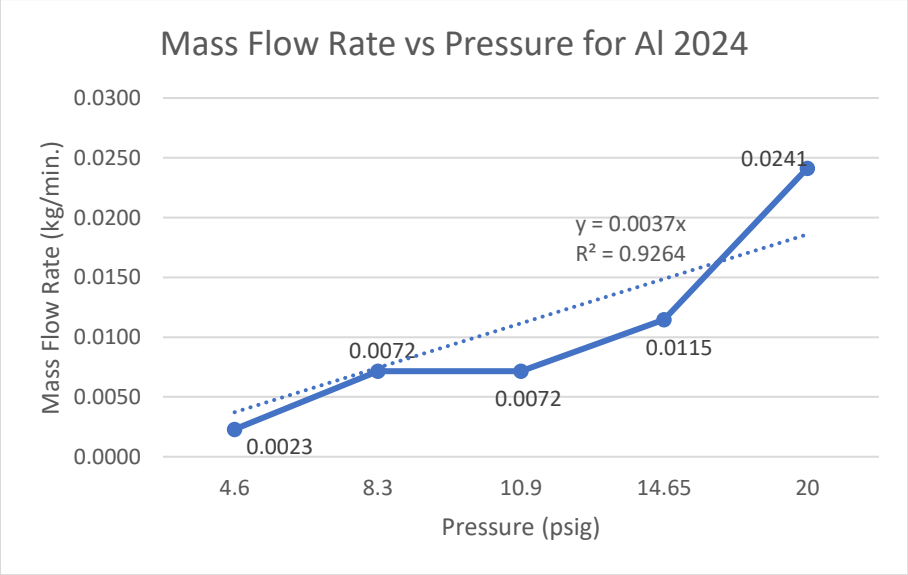

Figure 53: Mass flow rate of compressed air permeating through the Al2024 test speciment at various pressures.

Like the Al 2024 specimen,

Figure 54 and

Figure 55 show the manometer fluid height over time for each different pressure test of the CFRP-6 laminate. An initial spike in the fluid height is observed when data collection begins,

after which the fluid height increases at a decreasing rate. This trend would occur until the pressures in the manometer balance out, which can be seen for 0.4-, 0.7-, and 0.9-gauge pressures. Note that when the specimen was tested at 1.2-, 1.5-, and 1.6-gauge pressures, the manometer fluid height exceeded the length of the ruler used for measurement which is why there is no data for the full 10 minutes.

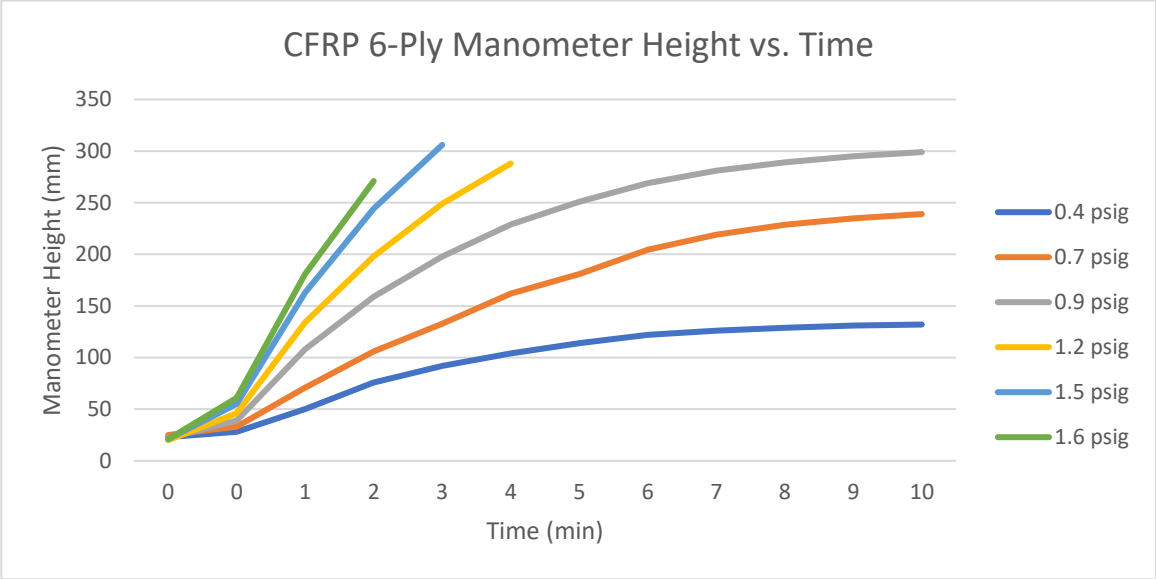

Figure 54: Displacement in manometer fluid height during CFRP-6 permeability testing. Note the initial spike in the fluid height.

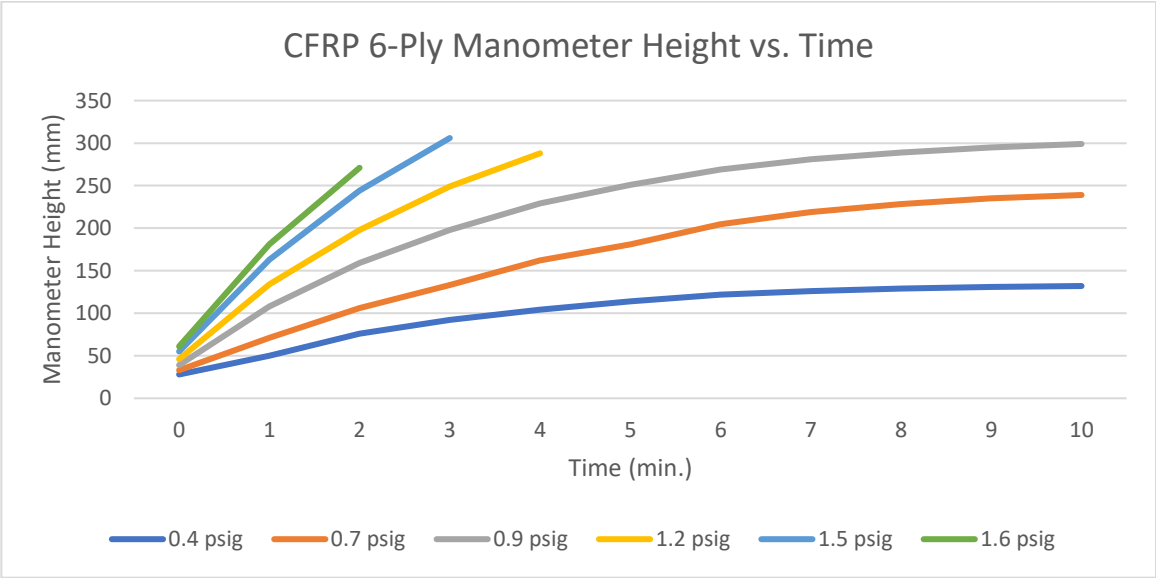

Figure 55: Displacement in manometer fluid height during CFRP-6 permeability testing after the initial spike in the fluid height.

From the manometer data collecting and following the same method as the Al 2024 specimen, the mass flow rate for the CFRP-6 was calculated at the various test pressures. The results are presented in

Figure 56. From the trendline, the mass flow rate increases by 0.3692 kg/min. with increasing pressure, and there is a stronger correlation between the data collected compared to the Al 2024 specimen. This is a significantly higher mass flow rate compared to the Al 2024 test specimen, which is expected.

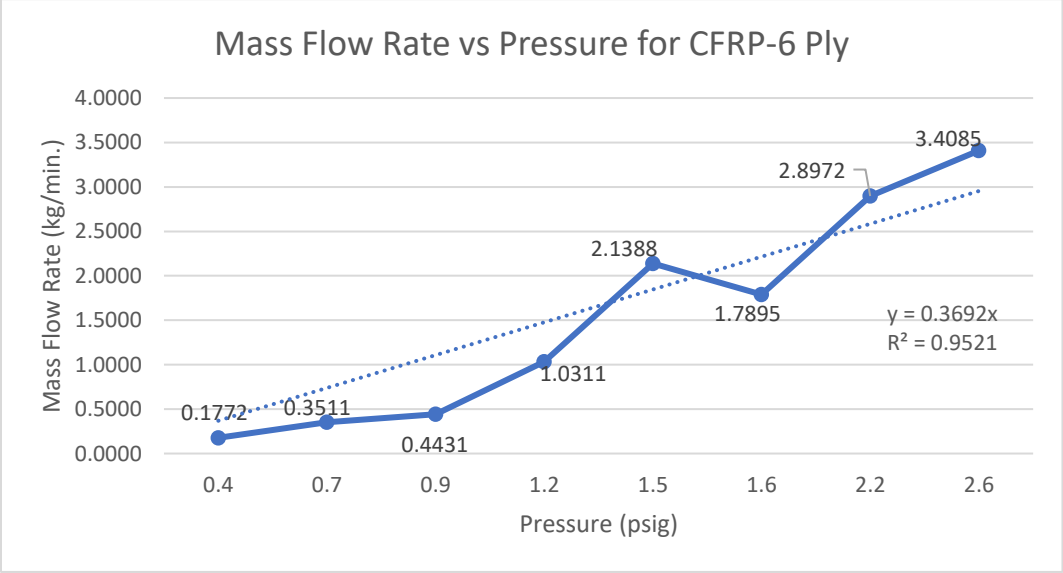

Figure 56: Mass flow rate of compressed air permeating through the CFRP-6 test specimen at various pressures.

The final test was performed for the CFRP-8 test specimen. The collected data are summarized in Figure 57 and Figure 58. As seen with the Al 2024 and CFRP-6 test specimens, an initial spike was also observed during the CFRP-8 tests. Note that the manometer heights recorded at various pressures for the CFRP-8 are much lower than for the CFRP-6 which was seen in

Figure 54. However, these values were still higher than the Al 2024 as seen in

Figure 51.

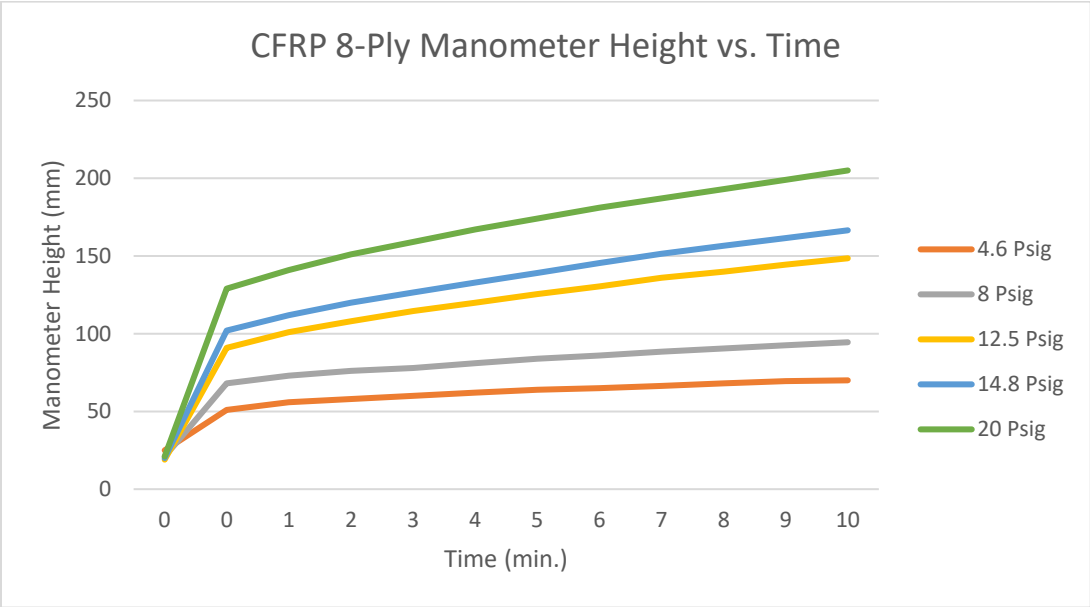

Figure 57: Displacement in manometer fluid height during CFRP-6 permeability testing. Note the initial spike in the fluid height.

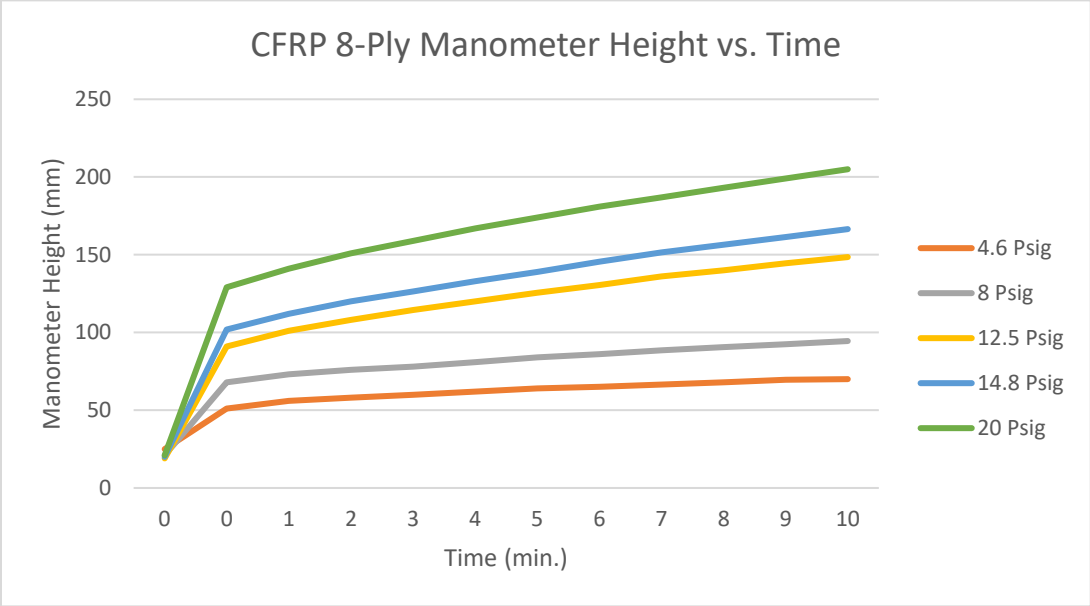

Figure 58: Displacement in manometer fluid height during Al 2024 permeability testing after the initial spike in the fluid height.

From the CFRP-8 data collected the mass flow rates at each tested pressure was calculated and plotted as shown in Figure 59. From the trendline, the mass flow rate increases by 0.0538 kg/min, which is almost 7 times less than the CFRP-6 test specimen. However, this mass

flow rate is still about 14.5 times more than for the Al 2024. There is also a very strong correlation between the data collected for the CFRP-8.

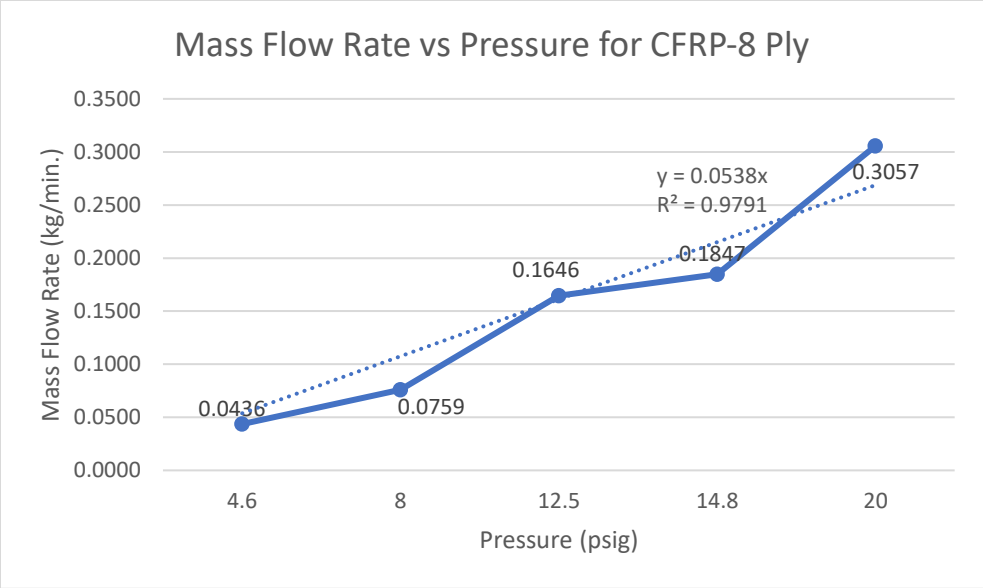

Figure 59: Mass flow rate of compressed air permeating through the CFRP-8 test specimen at various pressures.

Based on the graphs and table shown above, one can draw many conclusions, and point out some possible sources of error. It's apparent that an increase in laminas greatly decreases permeability through a laminate. The CFRP-6 slope (change in mass flow rate per pressure) was roughly 0.3692 kg/min., whereas the CFRP-8 slope was roughly 0.0538 kg/min. While the slope of CFRP-8 is very low and therefore shows this laminate does well at preventing permeability, the slope of the Al 2024 specimen was roughly 0.0037 kg/min. This shows a drastic decrease in permeability when using Al 2024 over carbon fiber. This trend follows the group's hypothesis. The R^2 value of all these slopes is greater than 0.92, meaning there is some error, but not enough to make the data collected invalid. Figure 60 combines the curves from Figure 53, Figure 56 and Figure 59 to further illustrate the differences in mass flow rates across each specimen.

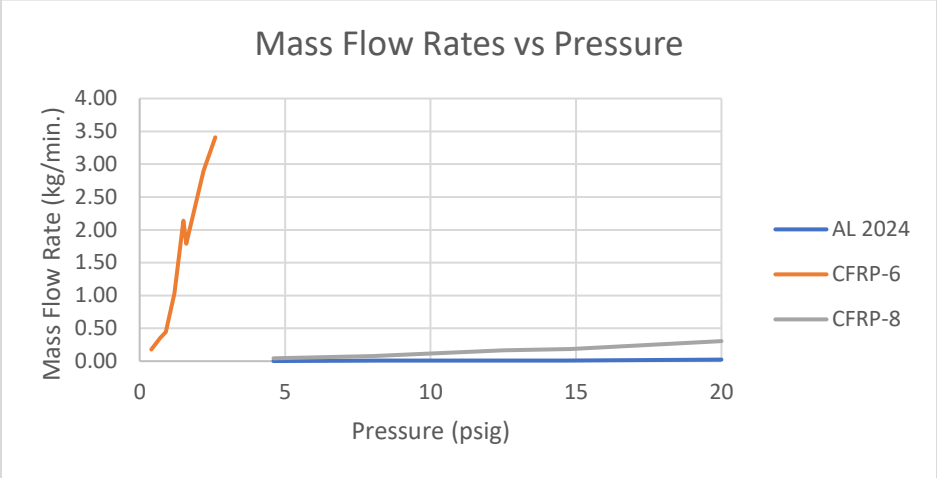

Figure 60: Mass flow rate of compressed air permeating through the AL 2024, CFRP-6 and CFRP-8 test specimen at various pressures.

One can assume there is some initial error when the ball valve is turned and gas begins flowing in the system, due to the before spike and after spike data. This leads to further errors in the first minute or so. A possible source of this error is the air flow around the gaskets and specimen, however this is unlikely since the team made sure this did not happen by modifying how the gaskets were cut.. There were likely small leaks of air in and around these points which might have resulted in a pressure gradient causing the spike seen in the plots above, which might result in possibly invalid data.

Additionally, the CFRP-6 data was very erroneous compared to the data of the other two specimens. There were only 3 pressures, all below 1 psig, that allowed for a 10-minute test to be conducted using our 300 mm ruler. All pressures above 1 psig took under 5 minutes to reach 300 mm and all pressures over 2 psig took less than 2 minutes to reach 300 mm. Overall, the data matches expected trends, with minor errors due to unexpected air leaks and an imprecise setup.

3.3.2 Venting Test Results

The venting tests were performed as discussed in section 3.2.3. The CVS was tested at four different tank pressure values which resulted in different mass flow rates through the sonic nozzle for each case. The pressure upstream of the sonic nozzle was controlled using a pressure regulator. The tank was filled with compressed air through a source upstream of the sonic nozzle and the pressure regulator. The solenoid valve was left open, so the tank pressure could reach

equilibrium with the input mass flow rate remaining constant. The team collected data by recording the pressure of the tank throughout the duration of the experiment. After equilibrium was maintained for an extended amount of time, the air flow into the tank was cut off and the tank pressure decreased to 0 psig.

Additionally, the emergency valve was tested by an Arduino script that opened and closed based on the pressure in the tank. These tests validated the research done into each of these systems.

Prior to starting the main experiments, the team calibrated the sonic nozzle using a pressure regulator to control the upstream pressure and recording the downstream flow rate using a volumetric flow meter. Several upstream pressures were used and the relationship between upstream pressure and flow rate is demonstrated in Figure 61.

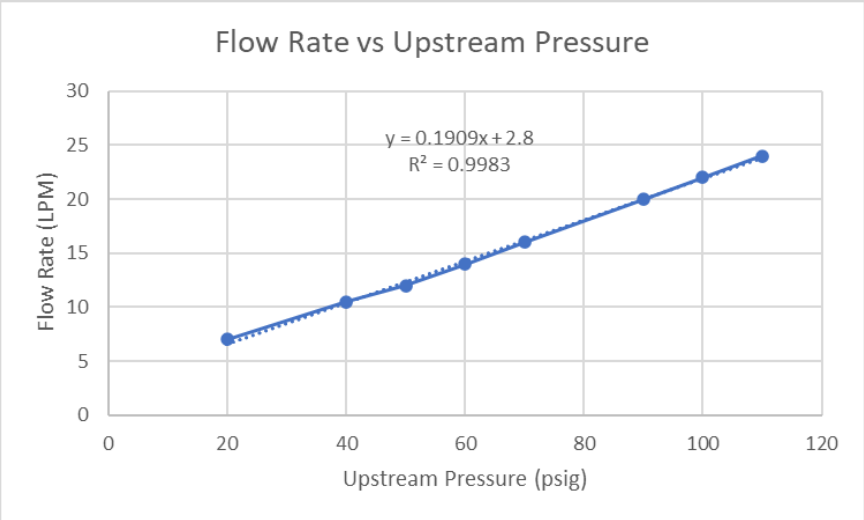

Figure 61: Flow rate versus upstream pressure for sonic nozzle validation

As shown in Figure 61, the data can be approximated by a linear model. This confirmed the expected results and allowed the team to continue with testing. The results shown here match the specifications of the sonic nozzle's manufacturer and the results of a previous MQP that used the same device (Davis et al., 2022).

Once the sonic nozzle was validated, the team was able to move forward with the CVS test. As seen in Figure 62, a pattern emerged for all four trials. For each case, the pressure initially rose, but leveled off after approaching a certain value. These values match the ones calculated and demonstrated the effectiveness of the system.

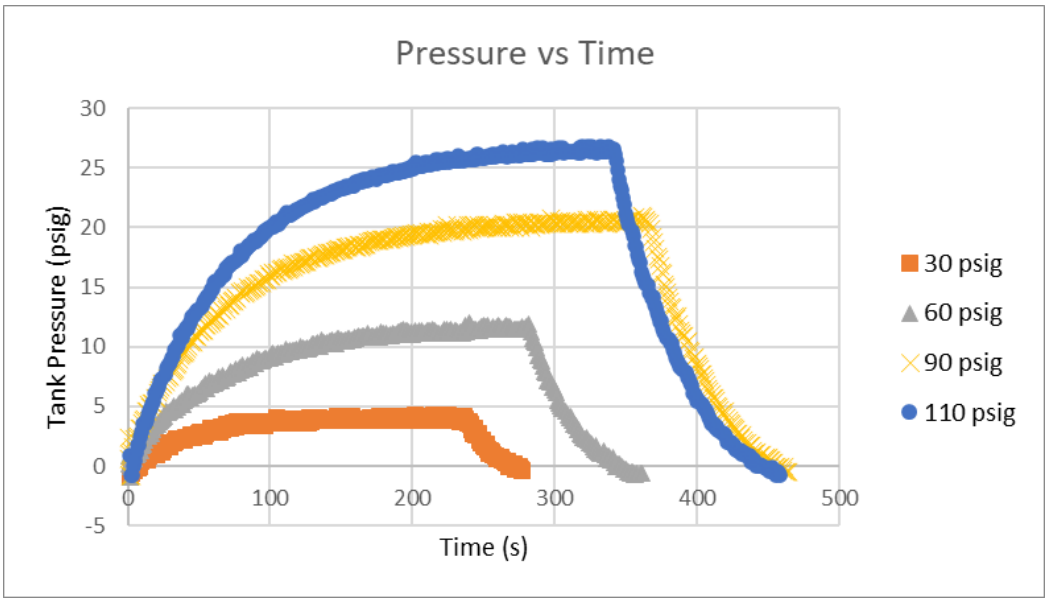

Figure 62: Tank pressures over time for CVS testing

From this data, the upstream pressure was graphed and compared to the equilibrium pressure of each trial, and we found a linear relationship between the two values, demonstrated by Figure 63. This was expected but confirmed through testing. This allowed the team to determine the settling value of the tank pressure based on either the upstream pressure or the flow rate into the tank calculated using the data in Figure 61. The theoretical equilibrium pressure for each case was also verified using equation (19) where the mass flow into the tank could be calculated and tank pressure could be solved for by setting the mass flow rate in equal to the mass flow rate out. These calculations correlated closely to experimental data where each experimental pressure value was within one psi of the theoretical result. These tests confirmed the results predicted by literature review and theoretical calculations.

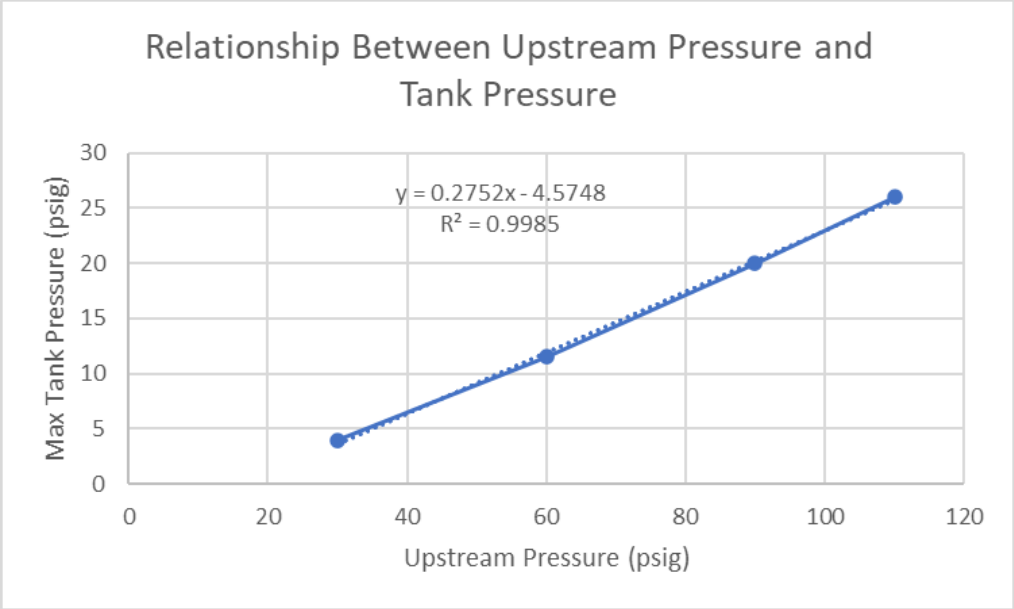

Figure 63: Relationship between upstream and tank pressure for CVS testing

The section of Figure 62 showing the equilibrium pressure for an upstream pressure of 110 psig during steady state has been plotted in Figure 64. The mean pressure during this period was about 26.4 psig while the standard deviation was approximately 0.2 psig. These results demonstrate the ability to maintain tank pressure within a small deviation from equilibrium for an extended amount of time, proving that this crucial aspect of a CVS design is feasible to achieve using the methods described by the team.

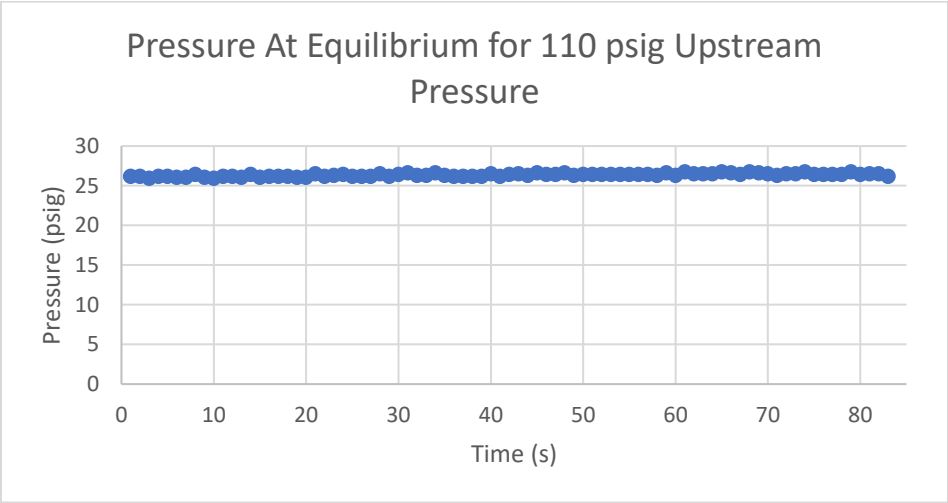

Figure 64: Pressure at equilibrium for 110 psig upstream pressure

To theoretically model the expected unsteady pressure drop in the compressed air tank, we numerically integrated equation (20). This involved substituting the equation for density as a function of time into the isentropic relations. These were then plugged into equation (20), so mass was the only time dependent variable. We then used the MATLAB function ode45 to find the mass of the fluid inside the tank at discrete time steps. The script can be found in section 6.6. Using the solution, the change in pressure over time could be found using the corresponding isentropic relation. The results only apply to the choked flow regime. Since the cryogenic spacecraft tank would vent into a vacuum during the mission, only choked flow would need to be analyzed to achieve our goal of creating a proof of concept for spacecraft propellant venting. Therefore, only the results for sufficient tank pressure to sustain choked flow are presented, as shown in Figure 65.

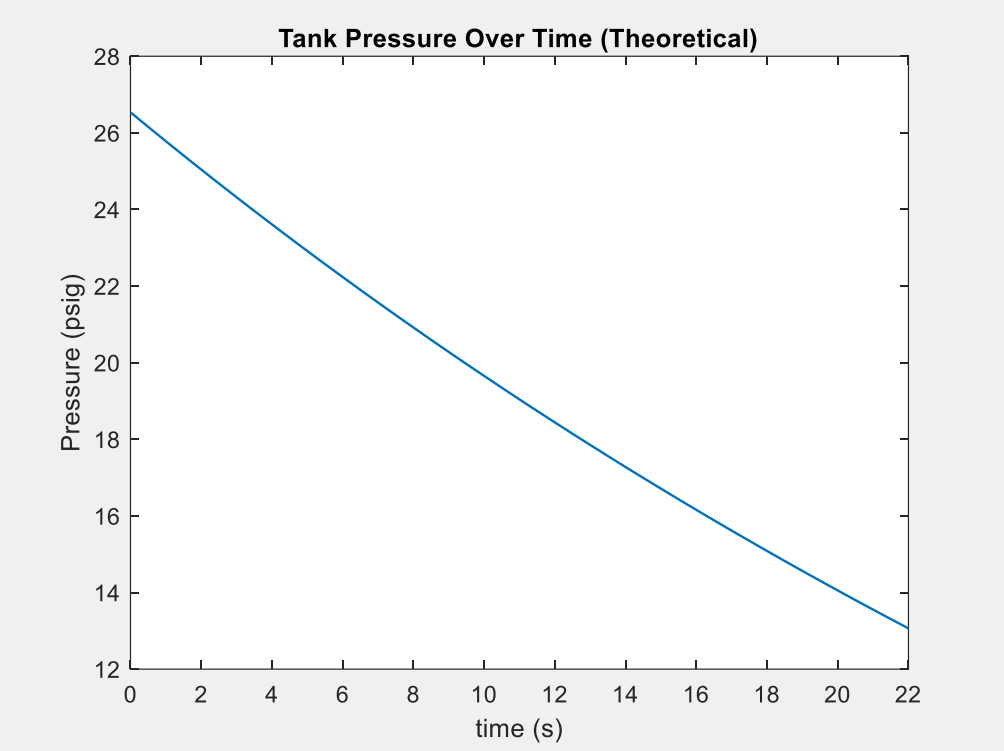

Figure 65: Theoretical compressed air tank pressure over time

The team conducted two trials to test the venting system over the same pressure range as the theoretical findings. The experimental results are presented in the Figure 66 and Figure 67.

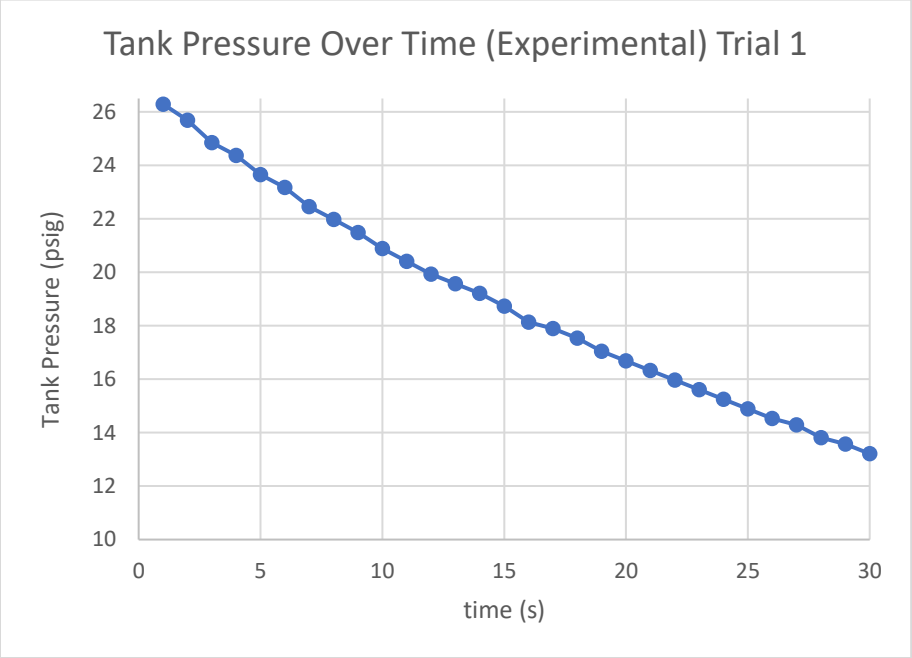

Figure 66: Experimental compressed air tank pressure over time trial 1

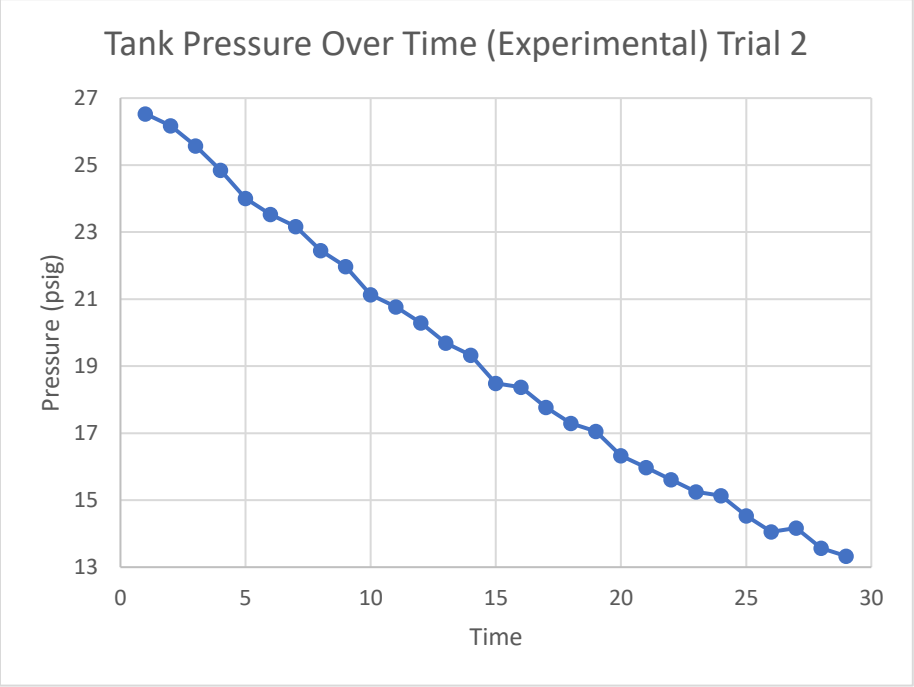

Figure 67: Experimental compressed air tank pressure over time for trial 2

The plots follow the same trend and cover a similar range as seen in the figures above and in

Figure 68 which indicates the validity of the theoretical model, and the applicability of the experiment. However, the theoretical and experimental results differ slightly. Figure 69 shows a comparison of the second experimental trial results to the theoretical results just during the choked portion of the flow.

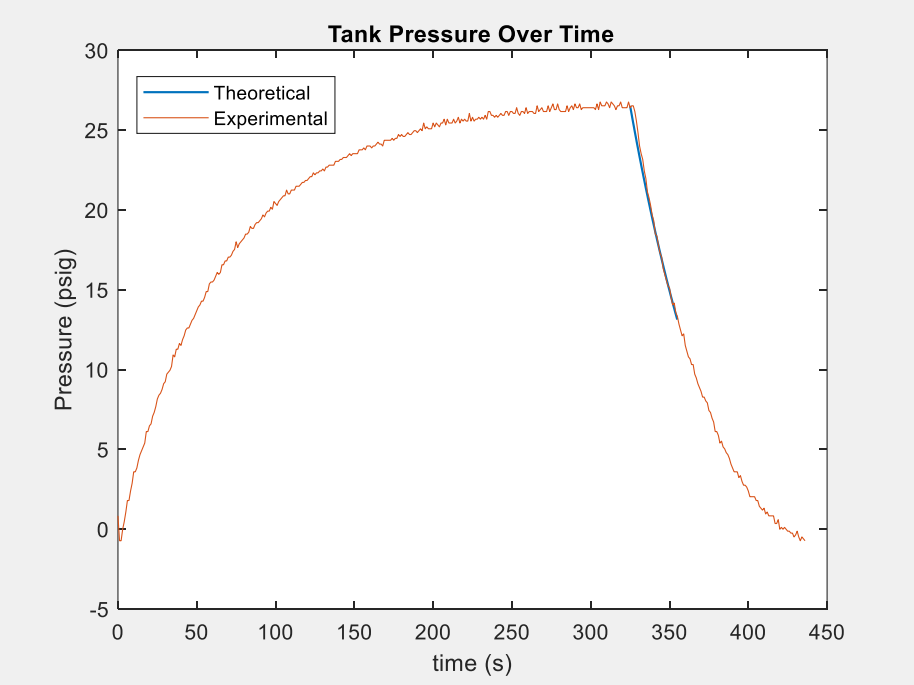

Figure 68: Theoretical vs experimental venting results for entire experiment

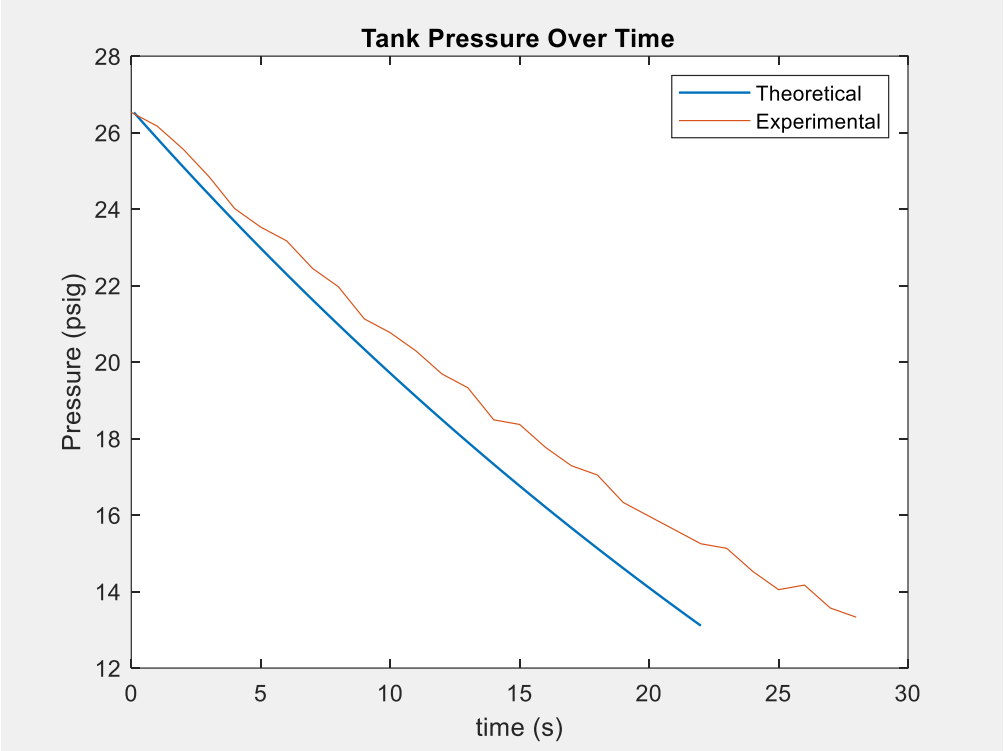

Figure 69: Theoretical vs experimental venting results for choked flow regime

It took 22 seconds to reach about 13.1 psig (the lowest pressure in the choked regime for venting into atmospheric conditions) for the theoretical model, while it took 30 seconds and 28 seconds to reach this pressure during the first and second trials respectively. This shows inaccuracy in the model. This inspired a comparison between the differential equation function results to the results of another model developed at the University of Illinois. This model was derived by substituting isentropic flow equations into the integral equation for conservation of mass and integrating with respect to time, assuming adiabatic thermodynamic conditions and a perfect gas (Dutton & Coverdill, 1997). The resultant equation is shown below. Where P_0 and T_0 represent the initial pressure and temperature respectively.

$$P = P_0 \left[1 + \frac{\gamma - 1}{2} \left(\frac{\gamma + 1}{2} \right)^{\frac{-2\gamma}{\gamma - 1}} \left(\frac{A\sqrt{\gamma R T_0}\, t}{V} \right) \right]^{\frac{-2\gamma}{\gamma - 1}} \tag{41}$$

We compared this model to the results of the numerical integration of equation (20) using the same initial conditions. Both models resulted in a similar pressure function as seen in Figure

70. This served as an effective verification of the theoretical model due to the low error between the results.

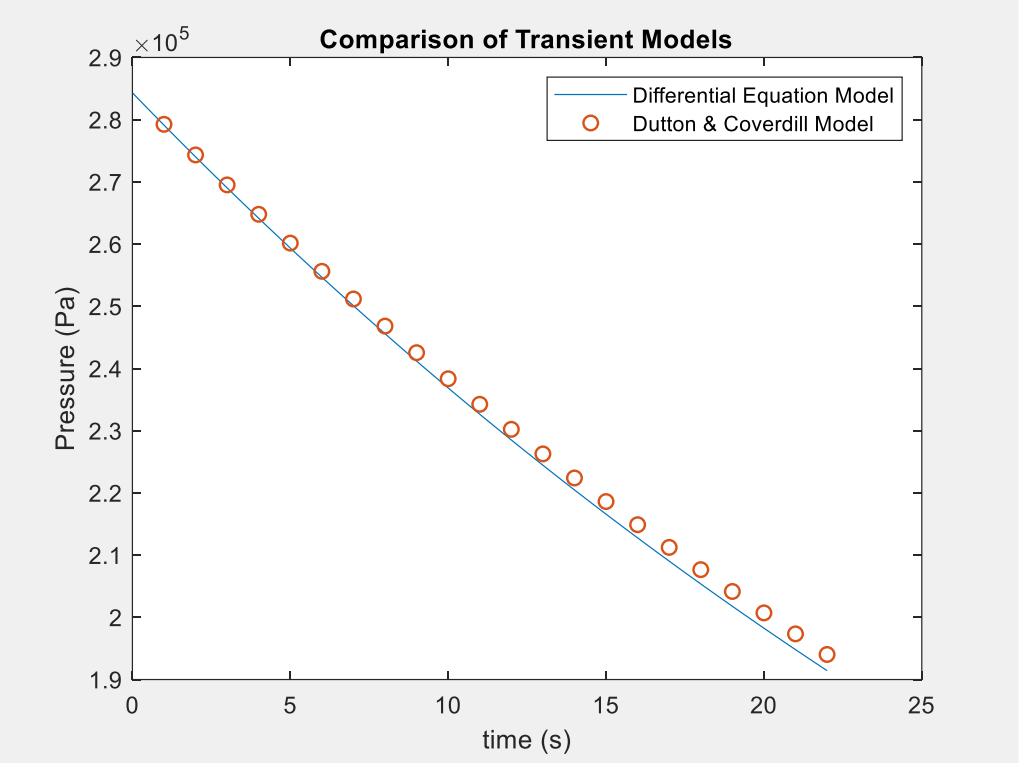

Figure 70: Comparison of models to predict change in tank pressure over time

Therefore, the team has concluded that the discrepancy in the results is due to other factors. A likely possibility is that viscous forces in the tank and associated plumbing resulted in a lower mass flow rate out of the tank during the experiment. Viscosity was not considered in the theoretical model so the mass flow rate would be greater in this ideal scenario. Other possible sources include human error during experimentation or inaccurate initial conditions such as temperature, or orifice exit area. These could be verified by measuring tank temperature experimentally and by repeating the experiment. The flow out of the fixed sized orifice could also be calibrated using a flow meter, the same method used to calibrate the sonic nozzle, and these results could be used to model the expected flow.

Additionally, the team tested an emergency venting valve. Using the code in section 6.6, the tank was allowed to pressurize until it reached 25 psig. At this point, the solenoid valve opened, and the pressure was allowed to reduce to 20 psig. Then, the valve closed again, and the

cycle repeated. The pressure in the tank was recorded during the entire process, and is shown in Figure 71.

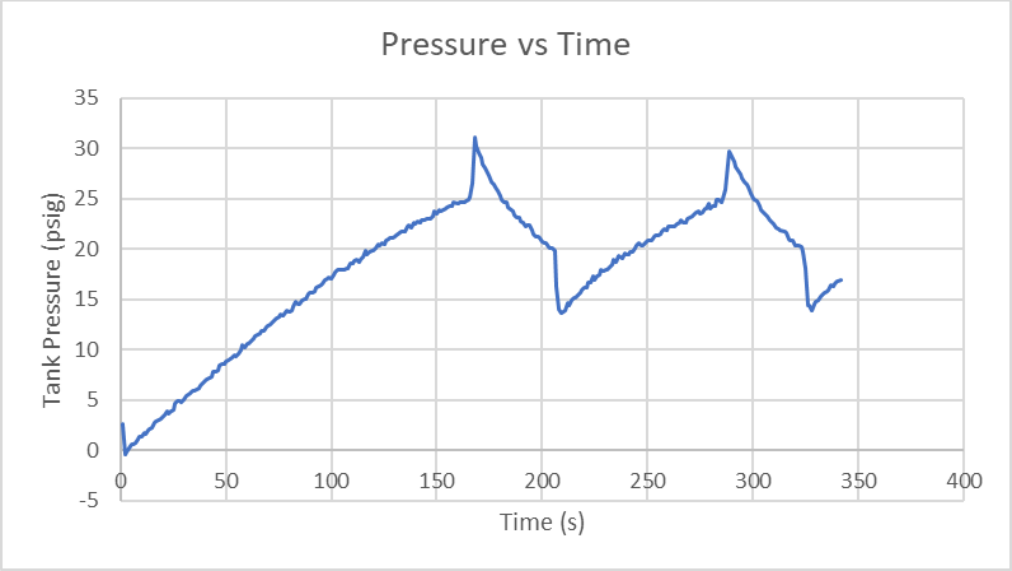

Figure 71: Tank pressure versus time for emergency venting valve

This experiment went mostly as expected; however, the plot shows spikes in data whenever the valve was opened or closed. This is likely due to the space between the solenoid valve and the orifice, which changes the volume of the tank when opened and closed, resulting in instability. Despite this, the pressure still stabilized and proved that a program can be written to successfully control an unexpected pressure increase.

We decided to compare the rise in pressure during the emergency venting test to a model developed using our sonic nozzle calibration. The pressure increase in the tank before the valve was opened was linear because the pressure upstream of the sonic nozzle was kept constant using a pressure regulator. Because of this, we could interpolate between volume flow rates using the function shown in Figure 71. We then derived an expression for pressure change over time using the ideal gas law and equation (42), which describes mass conservation for fluid flow over a control volume.

$$\frac{\partial}{\partial x}\iiint \rho \, dv + \iint \rho V dA = 0 \tag{42}$$

Figure 72 compares the results of the emergency venting experiment to the model developed using the method described above for the flow into the tank through the sonic nozzle.

The MATLAB script used can be found in section 6.11. The figure closely matches the experimental results which validate the theoretical model and the calibration results.

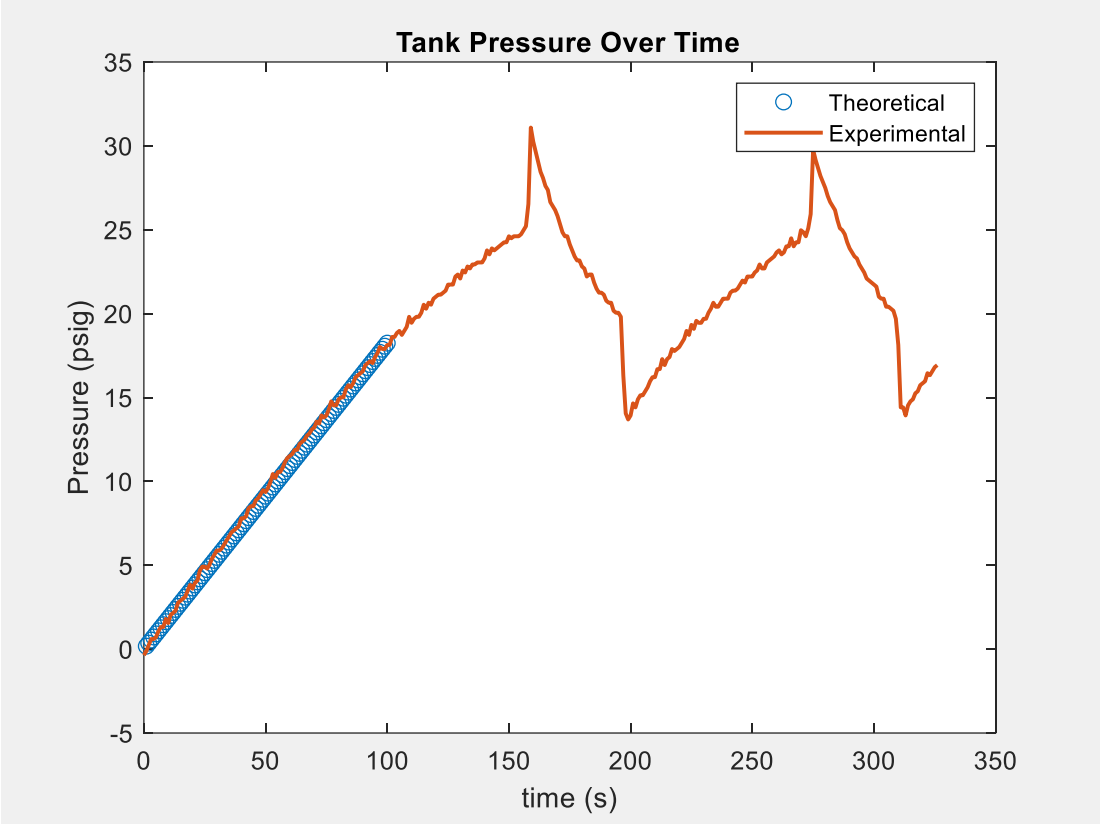

Figure 72: Emergency venting experiment vs calibrated mass Ffow model

3.3.3 Thermal Test Results

In this section, three experiments were conducted, all in pursuit of validating the team's COMSOL models of the boundary conditions a cryogenic propellant tank would experience in space. These tests would include spectrometry results, validating that the heat lamps used to replicate solar flux on the spacecraft were an accurate representation. Further testing was done in the vacuum chamber, with thermal analysis being run without vacuum being pulled and with a hard vacuum in place. The team was able to analyze tank layups made of aluminum 2024, mylar, and polyethylene rigid foam insulation. These results would then be compared to COMSOL simulations using the same boundary conditions produced and compared to simple hand calculations to see if these models were accurate in their results and that they could be used to produce accurate results for other tank layups.

3.3.3.1 Spectrometer Results and Discussion

As discussed in the previous section relating to the procedure for spectrometer testing, the team decided to examine different distances and angles to see how total flux and wavelength changed. Three setups were used, one with a twelve-inch distance between sensor and bulb, one with an eight-inch distance, and finally one with an eight-inch distance, but put slightly off center with a 25 degree angle. The figure below shows the luminosity produced at each wavelength in all cases.

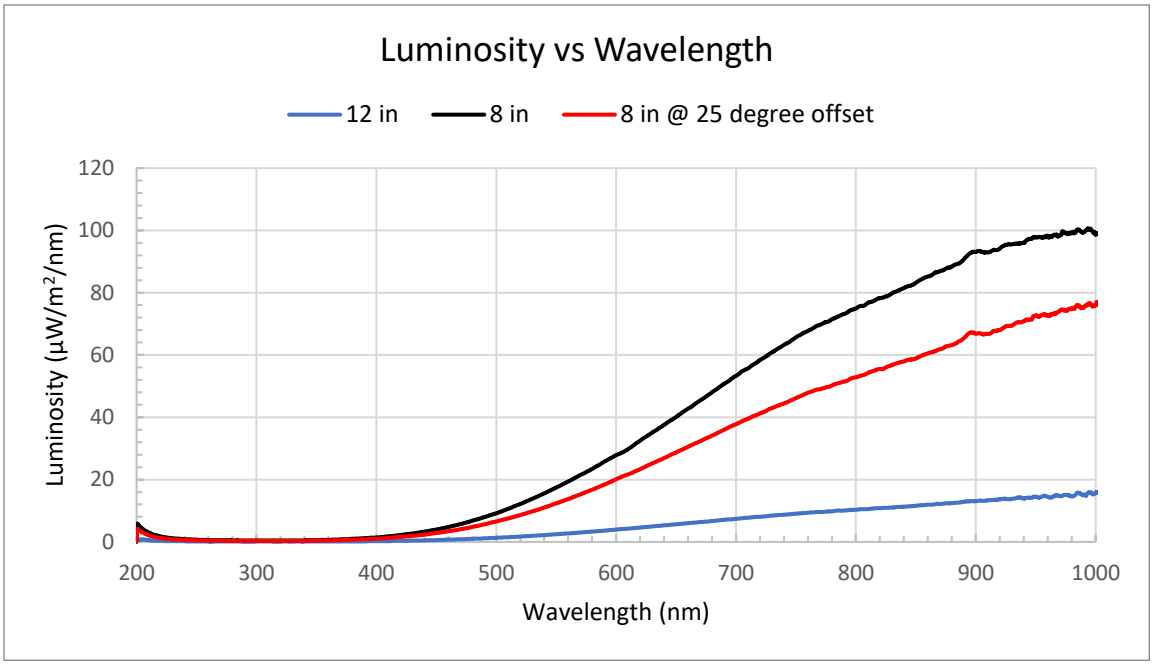

Figure 73: Luminosity vs wavelength of heat lamp bulb

As seen in the figure above, each trial shows a gradual increase in luminosity, starting at about 400 nm, and peaking at about 1000 nm. This data is not comprehensive though, as it does not show the luminosity produced at higher wavelengths than 1000 nm. These results can be compared to two other figures, one representing the luminosity produced by the Sun at Earth, and the typical luminosity of a halogen lamp, the same type tested in these trials.

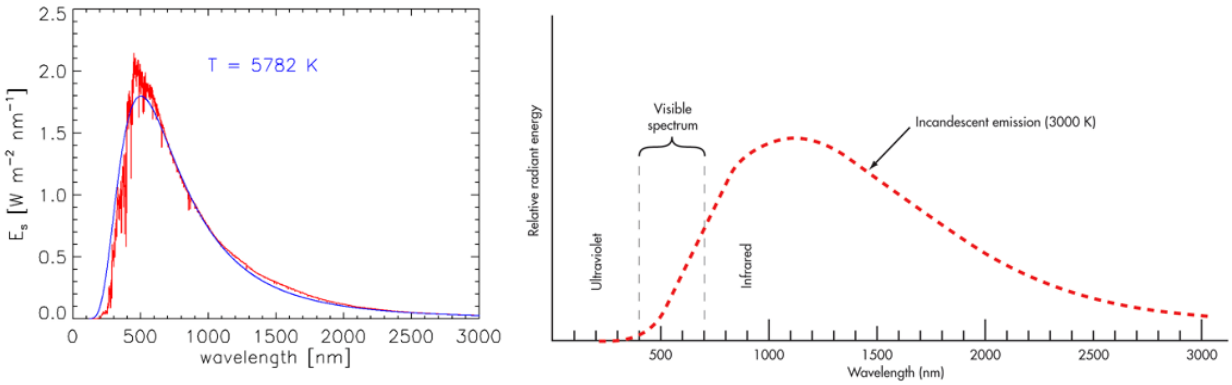

Figure 74: Luminosity vs wavelength of sun in space at Earth's distance and for typical halogen-tungsten bulb (Davidson, n.d.).

Comparing the measured flux from the bulb to the sun, the team saw how much higher its peak is, along with the fact that its peak wavelength is at roughly 700 nm, whereas the measured peak was at around 1000 nm. This also showed how solar flux is continually produced at lower levels past 1000 nm all the way to at least 3000 nm, showing how the measurements taken from the bulb were most likely not showing the full picture, and any estimates on total flux were conservative.

Comparing the team's measured results to a typical output from the same style of bulb, the similarities up to 1000 nm were clear. Compared to a solar flux, the rise to its peak was somewhat more gradual and smoother. The team assumed the rest of the profile would follow the same path as shown in the comparison to the typical output, but that could not be confirmed with the current collected results.

Regarding the thermal testing apparatus, it was clear that the wavelengths and corresponding flux produced at said wavelengths were not a perfect match to a solar output. To mitigate this, future teams could source bulbs with defined outputs, such as ones specially built to act as solar simulators. But as an approximation, the team felt confident that these bulbs used would work under the given constraints and requirements to continue thermal testing without much adjustment.

3.3.3.2 Heat Lamp Flux Calculations

Since the data collected from the spectrometer experiments was incomplete, the team had to rely on other methods to calculate the flux produced by the heat lamp bulbs. Hand calculations could be done to give a reasonable estimate.

The first thing that was found was the power of the bulbs themselves. The electrical power required to run the bulbs at full capacity was easy to find, as it was 250 watts per bulb. All this electrical energy is not completely converted to thermal energy though, thus an efficiency factor had to be introduced. For a typical Tungsten-halogen bulb, 90% of the electrical energy is converted to heat. Thus, the true thermal power produced is found through the following.

$$P_{bulb} = 250\ w * .9 = 225\ W \tag{43}$$

With the true power of the bulb, a flux at the distance of the specimen was found. This was found simply through the following calculation.

$$q = \frac{2(225\ W)}{4\pi(0.127\ m)^2} = 2220\ w/m^2 \tag{44}$$

This value was used in COMSOL simulations to verify the results found in the following sections.

3.3.3.3 Thermal Testing Results Without Vacuum

To help gain a better understanding of the apparatus and how all the different components would act under testing conditions, the team decided to conduct trials runs without any vacuum. This would allow for any issues to be corrected easily and provide insight into how closely this setup compares to COMSOL models and hand calculations, even if convection with the air could affect results.

The team first looked at the case of just aluminum, placing a thermocouple on the direct hot side of the specimen and cold side, while heat the hot side with the bulbs. The figure below shows the results compared to simulated values.

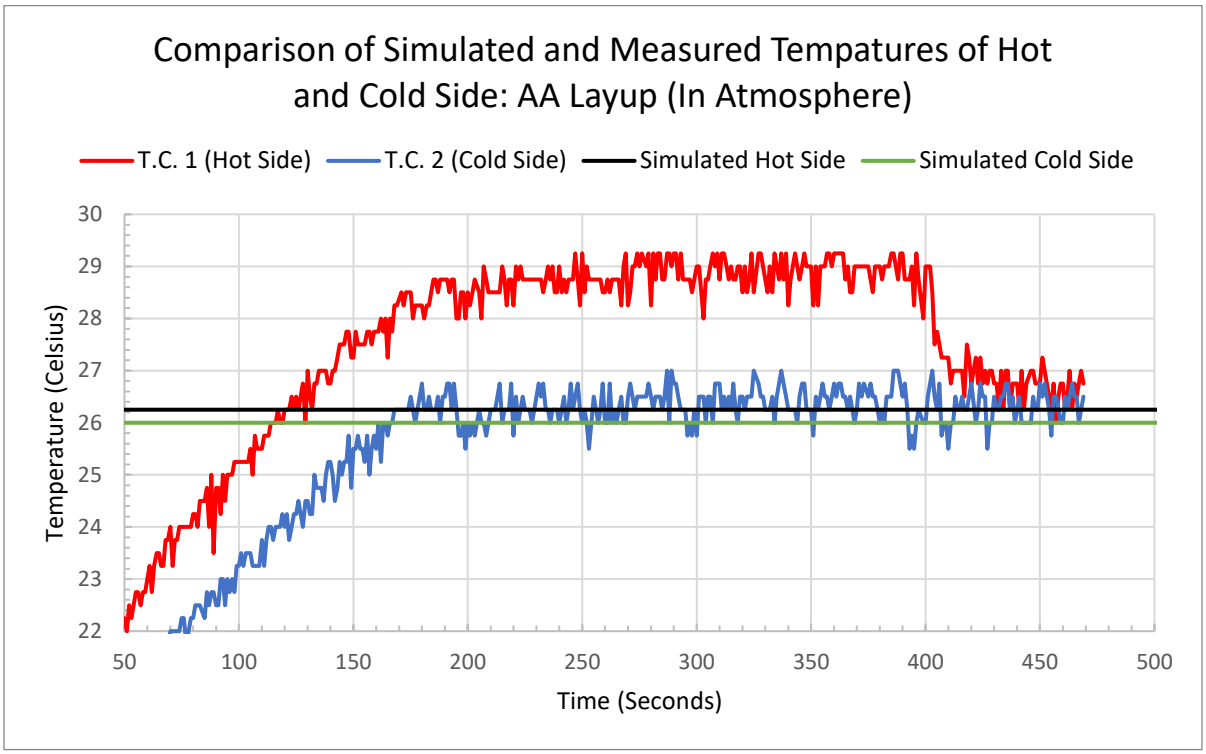

Figure 75: Thermal data of AA-2024

As seen above, the collected data shows a considerable differential between the hot side and cold side, whereas the simulated values are almost identical to each other. The average temperature differential for the measured values was 2.4 degrees Celsius. This discrepancy was caused by the setup of the apparatus. For this trial, the hot side thermocouple was placed directly in the view of the heat lamps. This caused it to heat up more than the aluminum around it, as the thermocouples are covered in a Kapton film, which had a much higher emissivity than aluminum. To mitigate this, every sample needed a layer of mylar on the hot side, and the thermocouple was placed in between the mylar and rest of specimen. This kept the thermocouple from being directly exposed to the flux and allowed it to only measure the temperature through conduction. This was also modeled in COMSOL, keeping the team's comparisons accurate.

With lessons learned from the first trial, the team decided to conduct the same experiment, but with the mitigations shown above. The figure below shows the data collected, and how it compared to COMSOL data simulated with the same conditions.

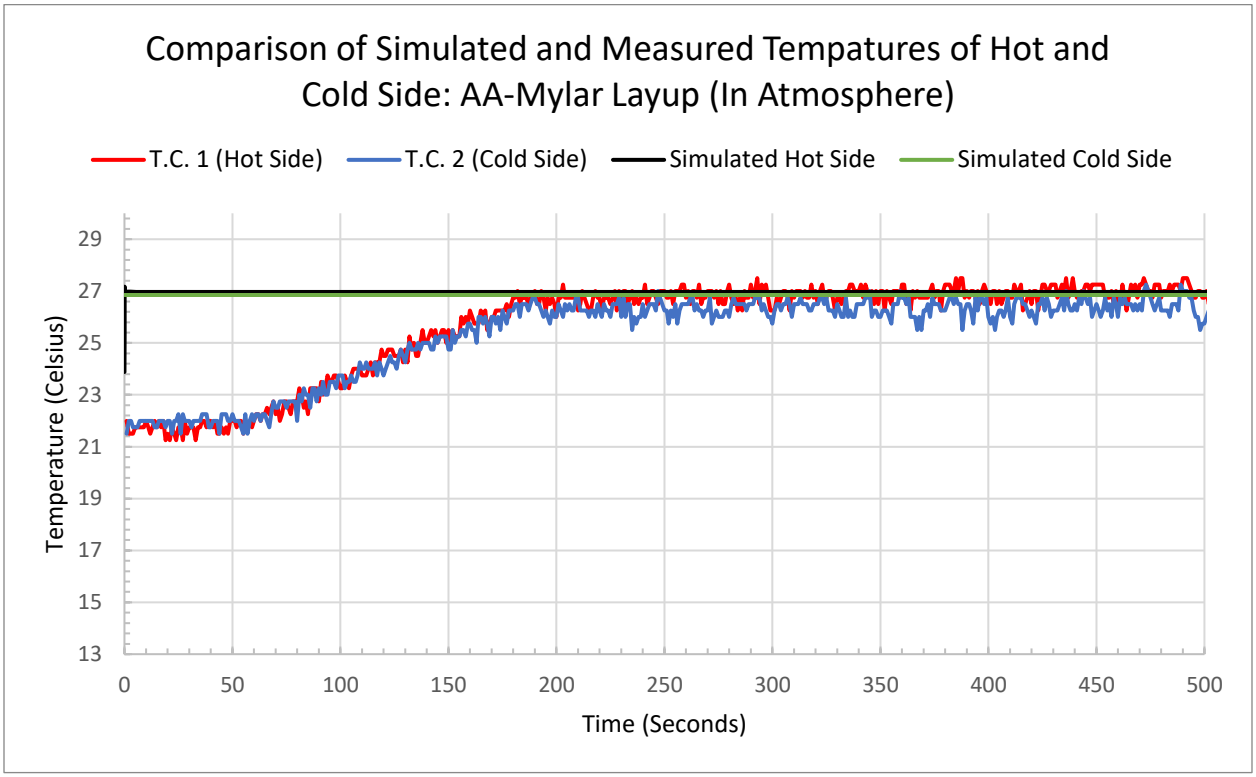

Figure 76: Second trial of thermal data of AA-2024

The results above showed a much closer relation between the simulated and measured values. In this trial, the average temperature differential was 0.25 degree Celsius at equilibrium. This can be approximated as zero, as the limit for resolution of the thermocouples used was 0.25 degrees Celsius. The rise seen by the measured data comes from the cold plate's activation temperature, as it was set to 26.5 degrees Celsius, and ambient temperatures were lower at the beginning of the experiment, thus causing the rise until the threshold was reached.

For a final test in atmosphere conditions, the team produced a specimen layered with mylar, polyethylene foam, and aluminum. This layup was expected to have a more substantial temperature differential, allowing for better comparisons between the model and simulations. The below figure shows the results.

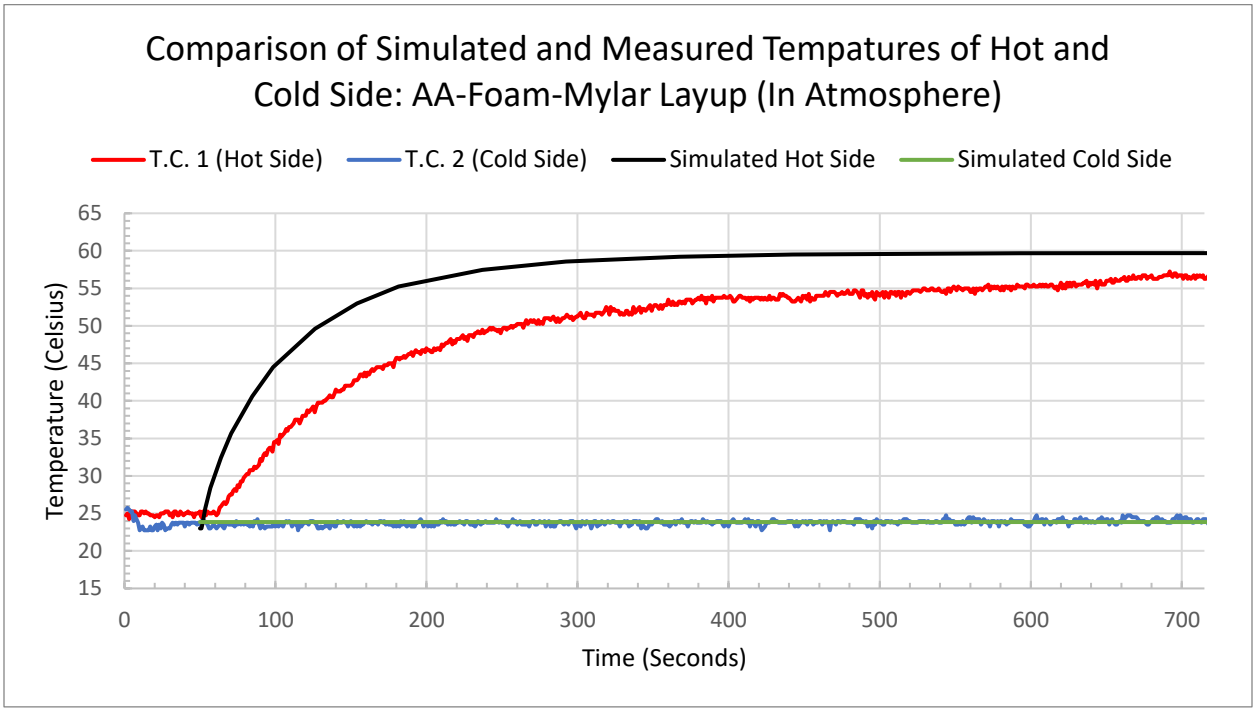

Figure 77: Thermal data of AA-Foam-Mylar

The data above shows a strong relation between the values found in COMSOL and measured through the apparatus. At equilibrium the difference between the hot side temperature measured and simulated was 2.6 degrees Celsius. This small difference could be related to inconsistencies with the material properties used in the COMSOL simulations. There is also a difference in the time taken to reach equilibrium, as the simulated values reached equilibrium much quicker than in real life. This could be due to convection taking away thermal energy from the specimen, causing it to take longer to become fully "heat soaked" and reaching a final temperature, which was lower than simulated. Overall, this data shows even with the effect of convection, COMSOL has given accurate results when the real-life conditions are well represented in the simulations.

3.3.3.4 Thermal Testing Results with Vacuum

As a final trial for thermal experimentation, the team ran an experiment on the AA-foam-mylar specimen, but this time under a hard vacuum. This required pulling the vacuum chamber to $3.0*10^{-5}$ Torr. The process took approximately four hours to complete and was done by Professor Taillefer. With the apparatus under vacuum, some unknowns were answered. One

being how the foam layer would react, as it's a porous material. Due to its rigid nature, the foam kept its shape quite well, showing little to no expansion under vacuum. The Peltier cooler also still operated in these conditions. Issues arose with increasing temperatures, as the excess heat caused outgassing of materials in the chamber, causing the pressure to rise slightly. The high temperatures affected the foam, as when specimen hot side temperature reached around 100 degrees Celsius, the foam lost it shape, and evaporated slightly creating a small pressure increase to about $5.5*10^{-5}$ Torr. The figure below shows the collected data collected after 75 seconds, when the heat lamps were turned on.

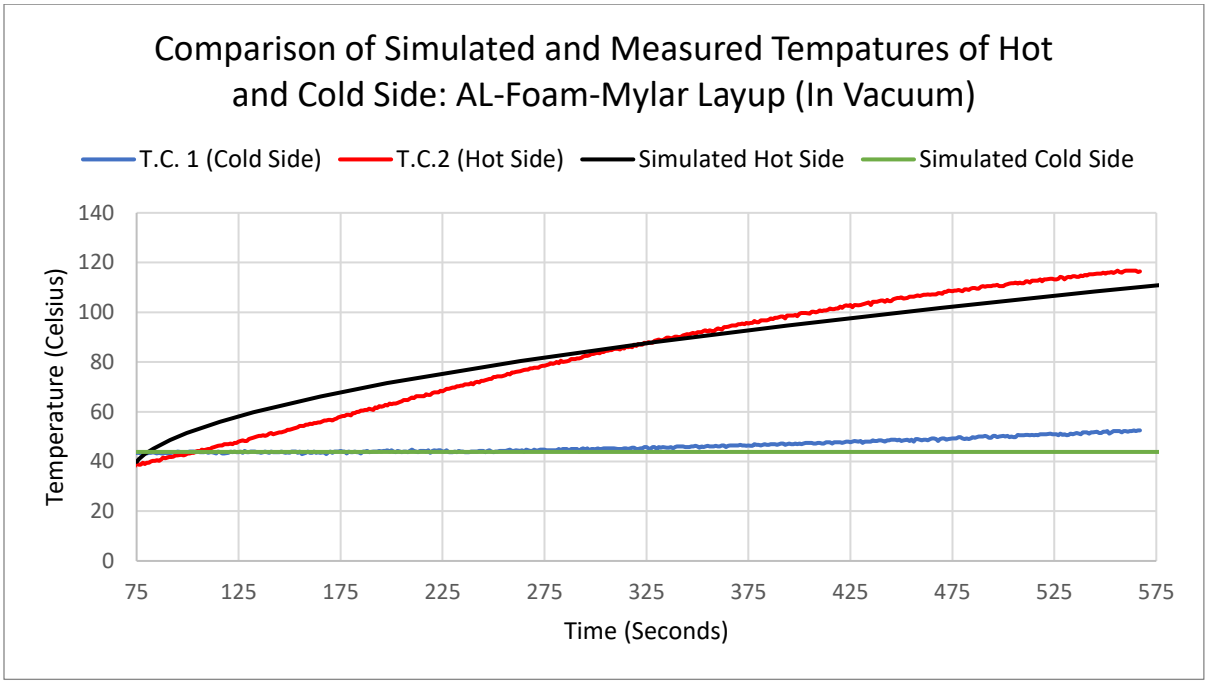

Figure 78: Thermal data of AA-Foam-Mylar in vacuum

The team compared this data to the previous trial with no vacuum, and two immediate things were seen. One being the magnitude of temperatures reached by the hot side, as temperatures of over 120 degrees Celsius were reached before the experiment was ended. The rate of temperature increase was also much more gradual. The team has two hypotheses for these differences. For the higher temperatures, the team believes that with the vacuum in place, and no air in the chamber, the heat absorbed by the specimen is not being taken away by convection. Thus, the temperature rose to much higher values. For the slower temperature rate of increase, the team concluded that with a vacuum pulled, the thermal conductivity of the foam had been changed. The reason behind this is that the foam used (Rigid Foam Board Polystyrene) is porous

in nature and gets much of its insulative abilities from the air that fills the small voids in the material. With a vacuum pulled, this air was removed, making the insulation more effective. This is a type of insulation used in industry, called V.I.P. (Vacuum Insulated Panel) and has a typical thermal conductivity of 0.003 W/(m*K). Although this value is most likely not the true value of our specimen's foam under vacuum, the team deemed it to be a good enough representation and was used for the COMSOL simulation to compare.

With adjusted simulations using the thermal conductivity value stated above, the measured values seemed to trend quite closely with the simulated values. Unfortunately, the team was not able to run the experiment till equilibrium, due to the issue of the foam outgassing explained previously. In addition, this trial was one of the last after a few calibration trials, thus temperatures were much higher initially. This caused the cooler to become slightly overworked, as shown by the slight temperature rise of the cold side at the end of the experiment.

3.3.4 Computational Determination of Boil-Off Rates Results

Upon executing the procedure described in section 3.2.5, the optimal propellant masses and O:F ratios were found for each propellant and material combination, which in turn yielded the amount of fuel and oxidizer lost to boil-off throughout the mission. The boil-off losses for the AA 2024 LH_2/LOx and LCH_4/LOx spacecraft are shown in Table 16, and the boil-off losses for the Grafil 34-700 CFRP LH_2/LOx and LCH_4/LOx spacecraft are shown in Table 17. Each table includes the optimal inputs (propellant mass and O:F ratio), overall spacecraft mass, baseline criterion (fuel remaining and ΔV remaining), and the amount of fuel and oxidizer in each configuration lost to boil-off.

Table 16: Boil-off losses for AA 2024 tank

	LH_2/LOx		LCH_4/LOx	
O:F Ratio	2.464 : 1		3.856 : 1	
Propellant Mass (kg)	873		852	
Spacecraft Wet Mass (kg)	1817.22		1697.25	
ΔV Remaining (m/s)	101.089		100.707	
Fuel Remaining (% initial fuel)	1.001		1.02	
Fuel and Oxidizer lost to boil-off (kg)	166.356	135.972	24.396	145.733

Table 17: Boil-off losses for Grafil 34-700 CFRP tank

	LH_2/LOx		LCH_4/LOx	
O:F Ratio	2.448 : 1		3.857 : 1	
Propellant Mass (kg)	852		844	
Spacecraft Wet Mass (kg)	1769.91		1681.13	
ΔV Remaining (m/s)	100.874		100.14	
Fuel Remaining (% initial fuel)	0.992		0.995	
Fuel and Oxidizer lost to boil-off (kg)	163.811	133.47	24.222	144.746

From these results it is apparent that differences in tank material had negligible effects in changing the spacecraft mass and boil-off rates of all fluids. The Grafil 34-700 spacecraft were only 15 to 45 kilograms lighter than their AA 2024 counterparts, yet the amount of fuel and oxidizer lost due to boil-off was nearly identical. Given the complexities in creating carbon fiber composites (as described in section 3.2.1), the added difficulties in their manufacturing over aluminum do not outweigh the minor decrease in mass they offer. It became clear then, that fuel selection was significantly more impactful in altering the weight and boil-off rates of the spacecraft.

The LH_2/LOx spacecraft were approximately 100 kilograms heavier and required 10-20 kilograms more propellant than their LCH_4/LOx counterparts. This was likely due to the differences in fuel densities and O:F ratios. Methane is denser than hydrogen; given the same mass requirement a smaller volume is required to store methane than hydrogen, resulting in smaller, and therefore lighter tanks (the opposite is also true; since hydrogen is less dense than methane, a larger volume, and therefore more massive tank, is required to hold a given mass requirement). However, methane requires more oxygen to react with than hydrogen to combust, therefore leading to a 1.6x increase in oxidizer, as shown by the O:F ratios.

Conversely, the LCH_4/LOx spacecraft experienced significantly less boil-off than the LH_2/LOx spacecraft, namely in the amount of fuel lost. The LCH_4/LOx spacecraft lost 24 kilograms of fuel (a total of ~170 kilograms of propellant), whereas the LH_2/LOx spacecraft lost ~165 kilograms of fuel (a total of ~300 kilograms). This is likely due to the chemical properties

of methane. Its higher boiling point, lower density, and higher enthalpy of vaporization than those of hydrogen work together to make methane more resistant to boiling over hydrogen (as previously discussed in section 1.1.1). However, more LOx boiled off in the LCH_4 spacecraft than in the LH_2 spacecraft, likely due to the increased amount of oxygen. This amount was small though – only a difference of approximately 10 kilograms.

Finally, these results differed from those in section 2.2.2 likely due to the inclusion of the MLI, which added non-negligible mass to all configurations, and the methods used to size the propellant tanks. In section 2.2.2 each tank was sized based on the mission parameters, material properties of the tank, and the densities of the fuel and oxidizers. While this approach is correct when constructing propellant tanks, it did not provide a consistent and fair baseline to compare each configuration to. This aspect was crucial in this project for accurately measuring how boil-off rates are affected by differences in propellant and tank material, and the method described in section 3.2.5 fulfilled this aspect.

Overall, the use of LCH_4 over LH_2 appeared to effectively minimize losses due to boil-off and decrease the overall mass of the spacecraft. Since the spacecraft in this project was small, the difference in mass between LH_2 and LCH_4 maybe be outweighed by the desire to use LH_2, with its more efficient and flight-proven technology since it's been reliably used since the 1960s. However, as these results are scaled up, the difference in mass will become more apparent, leaving LCH_4 as the clear choice in mitigating boil-off and minimizing mass.

3.4 Discussion of Design Results and Overall Conclusions

Overall, for the designed mission, a LCH_4/LOx spacecraft with AA 2024-T3 tanks equipped with MLI and a CVS mitigated the effects of boil-off best among the four spacecraft configurations. From the results of the computational determination of boil-off rates, the LCH_4/LOx spacecraft experienced significantly less boil-off than the LH_2/LOx spacecraft. Only 24 kilograms of LCH_4 was lost to boil-off, whereas 165 kilograms of LH_2 was lost to boil-off. Additionally, the LH_2/LOx spacecraft were heavier and required more propellant than their LCH_4/LOx counterparts.

Furthermore, tank material had a negligible effect in mitigating the effects of boil-off. Results from section 3.3.4 showed that propellant losses due to boil-off barely changed across differences in tank material. This was further corroborated by the thermal and permeability

testing results. Experimental values obtained from thermal analysis testing correlated well to COMSOL simulations, validating these results which showed that the AA 2024-T3 tank with MLI best mitigated the flux incident on the propellant tanks. Additionally, experimental results from permeability testing showed that CFRPs with higher layer counts demonstrate comparable permeability to that of aluminum. However, given the minimal differences in weight and boil-off rates, aluminum should be used as it is easier to work with due to the complexities of curing CFRPs. Based on the results of the permeability testing, however, more complex CFPRs (i.e., CFRPs with more layers and different fiber orientations) would likely have lower permeability and mass than that of aluminum. However, for the specimens tested in this project for the designed mission, aluminum is the preferrable choice.

Finally, the experimental results of the venting testing showed that a CVS and emergency value would work in effectively reducing boil-off. Further venting tests would need to be conducted to validate the results of the CVS and the emergency venting valve and their implementation on a lunar mission. However, results obtained in the conducted tests matched expected results, and CVS' have been used in the past as part of upper stage vehicles with coast times of a few hours, in which it has been effective, showing that this system is effective in reducing boil-off.

Despite these results, it is important to note that cryogenic propellants are not the gold standard for spacecraft propulsion. While they are extremely efficient (i.e., have high I_{sp}'s), they also require extremely complex and costly systems to implement and maintain. Therefore, simpler mono-prop and EP systems can achieve mission objectives just as well as cryogenic bi-prop systems for less money, as cryogenics would be overkill and unnecessarily complex.

Additionally, most missions to space currently involve satellites that orbit Earth, and not human crews on interplanetary voyages. As a result, the only onboard propellant needed are mono-props or EP systems for attitude control and adjustment in orbit, which are not cryogenic. Furthermore, if the payload is small enough, it can be launched on a small mono-prop rather than a large bi-prop, simplifying mission requirements and saving money. As a result, most bi-prop cryogenic systems are currently used to put a payload into orbit, after which they burn most of their fuel and are discarded, reducing the time needed to mitigate boil-off from a week to mere minutes. However, with the rise in interest in planetary missions, especially NASA's lunar exploration with the LH_2-fueled SLS and SpaceX's Starship, which will be powered by LCH_4

created on Mars, the implications of the results garnered from this project could help pave a new path in the history of space exploration.

4 Challenges and Future Improvements

The complexity of this project required numerous simplifications and assumptions to be made to our boil-off model and experiments for the team to achieve the desired objectives while completing the project on time, within budget, and in tandem with other required courses. Additionally, given the iterative nature of this project, the team was continuously learning and deepening our understanding of the problem at hand while performing our experiments and developing our model. Therefore, oversights were made during the project and recommendations for further work by future groups are discussed.

4.1 External Factors

Throughout the duration of the project, the team dealt with several factors outside of the group's control. To start, the team had a budget of $2000 to purchase all materials needed to conduct experiments. This led to the team simplifying experiments to keep costs down. Additionally, the team had approximately six months to complete the project. More time would have allowed the team to perform more in-depth experiments and analysis as well as allow follow-up research and testing at a larger capacity than what was done.

The team also experienced issues acquiring materials needed for composite curing, as there were significant delays between placing the initial order and shipping due to miscommunication with the vendor, Rock West Composites. The purchase order put in by the team had not been received by the Rock West team. The order was supposed to arrive within a week, so when it did not a follow up was made to the Rock West team, and the purchase order was placed through email instead of over the website. This delayed the start of composite curing and the permeability experiment.

Furthermore, the team used a vacuum chamber to perform thermal testing experiments and ran into issues with its usage. While setting up and testing the vacuum chamber, there was an electrical issue which prevented the bell jar from rising and lowering. This delayed the thermal testing timeline. Additionally, the team had to wait for the vacuum chamber to be available and work around the schedule of the professor in charge.

4.2 Oversights

Valuable research and experiments were conducted throughout the duration of this project; however, some key oversights were identified that must be noted. In concluding the analysis of the boil off model results, an oversight in the values used for heat transfer through the MLI was discovered along with an oversight in the simplification of ignoring convection at the gas-liquid saturated surface boundary layer.

Firstly, the value used for the average thermal conductivity of the MLI for the calculations in this project is 0.155 W/mK, which is an approximation based on the thermal conductivity of a single sheet of aluminized Mylar. This number does not accurately represent the performance of a MLI blanket, because it represents 1 layer of the 30 commonly used in deep space applications. The actual thermal conductivity of this MLI blanket should be $3.21*10^{-5}$ W/mK, which is significantly lower than the figure used in this project (Sutheesh & Chollackal, 2018). Confirming the thermal conductivity value of MLI was a major focus in the last few weeks of the project and calculations and research papers began to indicate that the approximation used was significantly larger than the true value. The team was unable to perform associated calculations with the new thermal conductivity values due to project time constraints.

To determine the average thermal conductivity of the MLI with a certain number of layers, the team used the Lockheed equation for flux through the blanket. For an MLI with polyester separator layers, the heat flux is given by the equation $q = ((C_s N^{2.63})/n)(T_H - T_C)$, where C_s represents the constant of solid conduction through the MLI based on the maximum outer temperature of the MLI, n represents the number of layers of reflector, N represents the number of layers of MLI per centimeter, and T_H and T_C represent the temperatures of the hot and cold sides of the MLI (Ross, 2015). This system consists of 30 layers of reflector, and 13.33 layers per centimeter of MLI. The outer temperature of the MLI is determined by the Stefan-Boltzmann law, with the equation $T = \sqrt[4]{\frac{(1-\alpha)E}{4\varepsilon\sigma}}$, in which $\propto$ represents the absorptance of the MLI's outer layer, E represents solar flux in space near Earth, ε represents the emissivity of the MLI's outer layer, and σ represents the Stefan-Boltzmann constant. This equation gives an outer temperature of 495.76 K. This can be used in the following equation to find the constant of solid conduction: $C_s = 2.4 * 10^{-4}\left(0.017 * 7 * 10^{-6}(800 - T)\right) + 0.0228\ln(T)$. This gives a constant of 0.14128, and using this in the Lockheed equation, one finds the flux through the MLI

to be 2.0138 W/m^2. With the equation $K = \frac{qd}{A\Delta T}$, the thermal conductivity was found to be 3.21*10^{-5} W/mK. This value lies within the order typical for an MLI of this type (M & Chollackal, 2018).

Based on the same underlying assumptions and calculations in this paper, if the thermal conductivity listed above is correct, this would mean heat flux into the cryogenic propellant tank would be approximately 0.3 W/m^2. Based on the current model of this system, the boil-off would be minimal, which cannot be the case. A preliminary simulation with this value was ran in COMSOL which indicated that the steady state condition would be reached over a period of time of months in direct sunlight rather than days, indicating that a simple broad approximation of MLI as a solid material with one thermal conductivity likely is an inaccurate simplification.

Secondly, the simplified boil-off model was constructed by the team to estimate the rate of boil-off within the cryogenic tanks and was a major component of the project. Significant research, discussion, and justifications were made for the steps taken in carrying out the project, but it must be noted that time was the main constraint in the accuracy of the results. Convective heat transfer is a significant physical phenomenon that governs the heat transfer in fluids based on their flow. The team was aware of this fact but mis-interpreted initial research and testing that seemed to imply convection at the gas-liquid layer could be easily ignored without major affects in the numerical accuracy of the results. The largest factor that led to the team choosing to move forward with neglecting convection was the added complexity it introduced to the simplified boil-off model and the time constraints to solve the new system. Calculating comparative boil-off estimates was deemed more important than potentially not finishing the model before the end of the project.

Ignoring the effects of convection is a common simplification made in thermodynamics problems to simplify calculations and often is a valid assumption based on the properties considered. The team initially planned to support this assumption through approximating the heat flux across the surface, s, based on the convective heat transfer formula at different orders of magnitude of the convective heat coefficient, h. The result of these approximations would have been that, within a margin of reason, the flux across the surface due to convection is negligible compared to the flux across the wall-liquid contact layer, and therefore the values of $\dot{q}_{ls}$ and $\dot{q}_{gs}$ are equal to 0 in the boil off model. For example, applying the convection equation $\dot{q}'' = h(T_s - T_\infty)$ to magnitudes of h at 10, 100, and 1000 assuming a temperature gradient across the

surface of 0.1 K yields $\dot{q}''$ in the order of magnitude of 1, 10, and 100 $[W/m^2]$. The assumption that the convective $\dot{q}''$ is negligible to compared to the $q_{ex}'' \approx 31\ [W/m^2]$ may only be valid for the single digit order of magnitude of h. Additional research was done to corroborate these 'back of the envelope' calculations. Shown below are two figures displaying the total heat flux through cryogenic hydrogen and oxygen (Richards et al., 1962).

These two oversights are intrinsically linked to one another. In the context of this study, ignoring convection would be valid if, and only if, the thermal load on the spacecraft does not reach the liquid or the gas. If the flux imparts any significant energy on the fluids, there will be a source of a temperature gradient at the surface node to generate convective heat transfer. Furthermore, for energy to be imparted on the fluids, the tank must experience a significant enough external thermal flux. Therefore, the relationship can be observed that one of the two oversights must be incorrect in this project. If the thermal conductivity of MLI is in-fact as low as referenced above, then an insignificant amount of heat will enter the fluid and the assumption to ignore convection at the surface node is substantially more grounded. If the thermal conductivity is on the order of magnitude of that used in this project, the convective heat transfer at the surface node is a noticeable contribution to the overall boil off problem and must be further researched. Additionally, it is possible evaporation, condensation or some other process has more impact on the tank than was anticipated, but these factors were not able to be considered for this project.

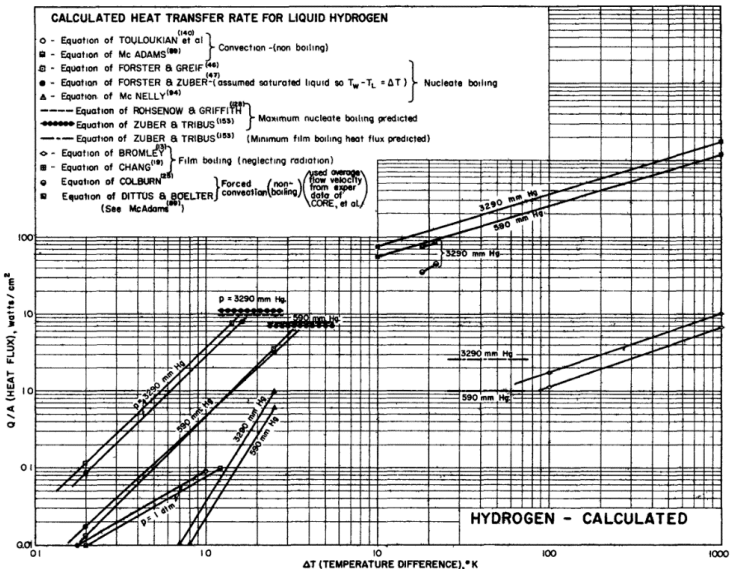

Figure 79: Heat transfer rate for liquid hydrogen at varying temperature gradients (Richards et al., 1962)

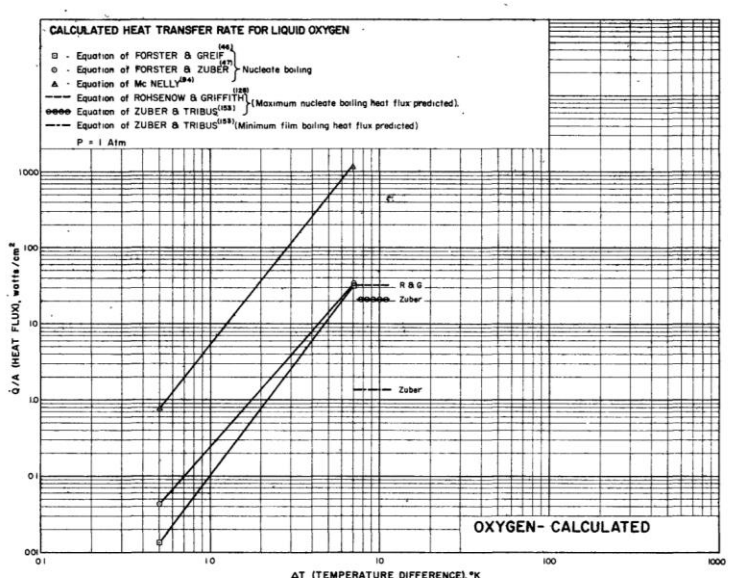

Figure 80: Heat transfer rate for liquid oxygen at varying temperature gradients (Richards et al., 1962)

Figure 79 and Figure 80 display the relationship of heat transfer and a temperature gradient for liquid hydrogen and liquid oxygen. At a small temperature gradient of 0.1 – 1 K, the magnitude of heat transfer varies on the scale of 100 - 10000 $[W/m^2]$. The values suggested by this source refute the assumption that was made in the paper, however, more research into this

source and related testing on the convective heat transfer coefficients would be needed to draw an accurate conclusion on this topic.

4.3 Project Broader Impacts

Some additional factors that would normally be considered by a company undertaking a project such as this are environmental, economic, global, and safety concerns. Liquid hydrogen and liquid oxygen produce little environmental effect, since no carbon is being released during the burning of this fuel, however, methane does negatively impact the climate because the reaction produces carbon dioxide. Cost is a factor when determining what types of systems the team would use; the aim is to reduce costs while ensuring all materials meet the design requirements and can keep the system safe. Additionally, other nations are improving their space programs at a level that could eventually compete with the United States. Even scientific missions could potentially influence global politics and the space programs of other nations.

Another factor is that cryogenic propellants are significantly harder to handle and store. All the aspects that contribute to the handling, storage, and transport of these fluids are more expensive and require a higher degree of safety. Hydrogen is especially difficult because its atomic size makes it more prone to leaks.

Lastly, the safety of the people working in and around the rocket would be the most important factor. Hazardous materials and safe fabrication practices would be used to avoid putting the people and mission at risk. Due to time, financial, and computational constraints, however, the team did not focus on these factors as heavily compared to the technical aspect of this project.

4.4 Recommendations

To guide future teams working on this project, the team has evaluated the best courses of action for further research and experimentation. In the following sections, recommendations for each experiment and area of study are provided.

Composite Curing and Permeability Testing

There were several modifications that could be made for the curing of the composite laminates. After creating the curing apparatus, the team observed gas leaking into the vacuum sealed bag during the curing process. To address this issue, one solution would be to keep the

vacuum bag under constant vacuum for the entirety of the curing process. Another solution would be to modify the current procedure to create a proper seal between the nylon film and the sealant tape when creating the vacuum bag. A third option would be to try buying a vacuum bag from a company that works with curing composites. Creating a proper seal and having the composite layup fully vacuumed would result in a properly cured composite compared to what was produced for this project.

In addition to addressing the leakage issue in the vacuum bag, future teams should create CFRP-6 and CFRP-8 specimens of their own to validate results presented in this report. A CFRP-10 and thicker specimens should be cured and tested to determine if the data collected follows the trends seen from the CFRP-6 and CFRP-8 specimens. Different fiber orientations as well as different CFRP materials should also be tested to see what trends arise during permeability testing. The team did not cut the cured CFRP-6 and CFRP-8 specimens, however, if this is required by future teams, proper safety protocols must be followed according to OSHA guidelines.

To model the composites, future teams are recommended to use CLT which was briefly described in section 1.1.4.4. By using CLT, future teams can understand under what stresses each lamina in their chosen composite material will fail and model it with different fiber orientations. MATLAB might be the preferred software of choice to perform the calculations. The team did not have enough time to work on this, which is why this could be an area of focus for future teams.

For permeability testing, analysis should be performed to determine the true cause of the spikes observed in the data presented in section 3.3.1. The team was not able to identify/address this issue, and this should be a priority for future teams for more accurate data collection. The team also recommends using different slugs in the manometer during testing other than water. Consider using a denser fluid for testing at higher pressures for a slower increase in slug height so more data can be collected. Future teams are also recommended to test different gases other than compressed air, more specifically, methane and hydrogen gas. Note that the testing of these gases will require modification of the current testing apparatus for data collection and safety reasons. One possible modification would be to test under a fume hood.

Venting Test of Simplified CVS Model

To successfully implement a CVS on a spacecraft, further experiments must be conducted. Due to budget and time constraints, the team tested a simplified model of this system with pressurized air. The next step would be to evaluate this system using GH_2. This would more closely model a real-life system but would require a more advanced ventilation system and a tighter seal between all connections. It would also need a ball valve as opposed to a solenoid valve. An additional test would use LH_2 in a storage vessel with a constant heat flux imparted on the tank. This would be significantly more complicated to model and determine the orifice size as well as require more advanced and expensive equipment. To start, all the parts would need to be rated to manage cryogenic material, otherwise the valves and ducts could freeze and break. In order to prevent rapid boil-off, the experiment would need to be conducted in a controlled environment, one in which a known heat flux is introduced with no external heat sources. A proper ventilation system is paramount since LH_2 expands significantly once it boils off. Lastly, safety procedures would be much stricter as improper handling of cryogenic liquids can lead to serious accidents. A potential step in between could be to use a different cryogenic liquid such as liquid nitrogen.

Heat Transfer Experiments

If it is decided that future teams would like to conduct more thermal testing in the vacuum chamber, there are a few areas of study that could be expanded on. For this project, the team only evaluated one specimen under vacuum, so to gain more data future teams could look into testing more types of materials, with various layups. This could include using new types of insulation layers that could withstand the heat imparted on them by the apparatus, different tank materials such as the CFRPs, and the use of MLIs created through mylar and netting.

The team also recommends that more research and investment should be put into characterizing and possibly buying already characterized heat lamp bulbs for the vacuum chamber. With well-defined values for heat flux produced by the lamps, comparing simulations and hand calculations to experimentally found results would be much more accurate and remove complexity.

Computational Determination of Boil-Off Rates

As discussed in 4.2, while preliminary results were gathered from the boil-off MATALB model, some key adjustments need to be made to the analysis of the system for more accurate calculations. A more refined analysis of the thermodynamic system inside the propellant tanks is needed to consider the effects of liquid-gas phase change occurring at the tank-liquid contact layer. This effect was not directly addressed in the mass transfer analysis which broke the problem into the three sections of condensation, evaporation, and bulk boiling.

Next, given the team's oversight on the true value of the thermal conductivity of the MLI, further research into the heat transfer properties of this material is needed to confirm what value for the heat flux in to the fluid can be assumed constant throughout the duration of the mission and if the value should even be considered constant. The team recommends that a higher fidelity COMSOL model of MLI is tested with both conductive and surface-surface radiative heat transfer correctly accounted for as a key design element of MLI is the reflection of radiation at each layer.

Based on the team's current understanding, the importance of convective heat transfer at the gas-liquid surface layer currently appears too important to the problem to be ignored for accurate results. The contribution of convection needs to be accounted for in the thermodynamic analysis and MATLAB script (section 6.7). Lastly, the MATLAB script should be revised so that the optimal O:F ratios and propellant mass are automatically calculated, rather than having the user manually input and find these values as was done in this project.

5 References

Aeronautics Guide. (2020, July). *Description of Composite Structures*. Retrieved from Aircraft Systems Tech: https://www.aircraftsystemstech.com/2020/07/laminated-structures-fiber-forms-and.html

Arnold, S. M., Bednarcyk, B. A., Collier, C. S., & Yarrington, P. W. (2007). *Spherical Cryogenic Hydrogen Tank Preliminary Design Trade Studies.* Cleveland: NASA.

ASHRAE Terminology. (n.d.). Retrieved from ASHRAE Terminology - Terminology Presentation: https://terminology.ashrae.org/?term=cryogenic

Atkinson, N. (2020, April 20). *Even More Things That Saved Apollo 13, part 1: The Barbecue Roll*. Retrieved from Universe Today: https://www.universetoday.com/145636/even-more-things-that-saved-apollo-13-part-1-the-barbecue-roll/#:~:text=Flights%20to%20the%20Moon%20on,to%20even%20out%20solar%20heating

AVIO. (2022, September 9). *FIRST HALF 2022 RESULTS*. Retrieved from AVIO: https://www.avio.com/press-release/first-half-2022-results

AVIO. (n.d.). *M10 ENGINE*. Retrieved from AVIO: https://www.avio.com/m-10

Barsi, S. (2011). *Ventless Pressure Control of Cryogenic Storage Tanks.* Cleveland: Case Western Reserve University .

Bergman, T. L., Lavine, A. S., Incropera, P. F., & Dewitt, D. P. (2011). *Fundamentals of Heat and Mass Transfer, Seventh Edition.* John Wiley & Sons.

Biesbroek, R., & Janin, G. (2000). Retrieved from https://www.esa.int/esapub/bulletin/bullet103/biesbroek103.pdf

Birkland, J. O., Dillon, A. K., Guzman, J. C., Jackson, J. R., & McCarville, D. A. (2017). *Design, Manufacture and Test of Cryotank Components.* NASA.

Boen, B. (2013, October 30). *Cryogenic Propellant Storage & Transfer (CPST)*. Retrieved from NASA: https://www.nasa.gov/mission_pages/tdm/cpst/cpst_overview.html

Britannica, T. E. (2022, December 9). *helium*. Retrieved from Encyclopaedia Britannica : https://www.britannica.com/science/helium-chemical-element

Burge, G., & Blackmon, J. (1972). Retrieved from https://core.ac.uk/download/pdf/42892576.pdf

Concept Group. (2019, July 31). *Vacuum Super Insulation with High Temperature MLI*. Retrieved from Concept Group LLC: https://conceptgroupllc.com/mli-takes-our-high-temp-vacuum-insulation-to-the-next-level/

Corpening, J. H. (2010). *Analytic Modeling of Pressurization and Cryogenic Propellant - NASA Technical Reports Server (NTRS).* Hunstville: Teledyne Brown Engineering.

Davidson, M. W. (n.d.). *Education in Microscopy and Digital Imaging*. Retrieved from Zeiss: https://zeiss-campus.magnet.fsu.edu/articles/lightsources/tungstenhalogen.html

Davis, E., Sirois, J., Stern, J., & Kodali, M. (2022). *Design, Implementation,and Testing of Apparatus to Investigate Combustion Phenomena Relevant to High-Altitude Relight.* Worcester: Worcester Polytechnic Institute.

Desert, C. o. (2001, December). *Hydrogen Fuel Cell Engines and Related Technologies.* Energy.gov. Retrieved from https://www.energy.gov/sites/prod/files/2014/03/f12/fcm01r0.pdf

Dexcraft. (2015, October 7). *Aluminium vs carbon fiber – comparison of materials*. Retrieved from Dexcraft: http://www.dexcraft.com/articles/carbon-fiber-composites/aluminium-vs-carbon-fiber-comparison-of-materials/

Domen, S. R. (1991). Emissivity of Aluminized Mylar. *International Journal of Radiation Applications and Instrumentation. Part C. Radiation Physics and Chemistry, vol. 37,* 199-201.

Dunbar, B. (2008, April 12). *Advanced Space Transportation Program: Paving the Highway to Space*. Retrieved from NASA: https://www.nasa.gov/centers/marshall/news/background/facts/astp.html#:~:text=Today%2C%20it%20costs%20%2410%2C000%20to,per%20pound%20within%2040%20years.

Dutton, J. C., & Coverdill, R. E. (1997). Experiments to study the gaseous discharge and filling of vessels. *International Journal of Engineering Education*, 123-134.

Erwin, S. (2019, May 14). *Cost of Delta 4 Heavy launches is down but the real price is a secret*. Retrieved from Space News: https://spacenews.com/cost-of-delta-4-heavy-launches-is-down-but-the-real-price-is-a-secret/

Finckenor, M. M., & Dooling, D. (1999). Multilayer Insulation Material Guidelines. *NASA*, 44.

Fragoudakis, R. (2019). *Strengths and Limitations of Traditional Theoretical Approaches to FRP Laminate Design against Failure.* IntechOpen.

Furter, J., Halfrey, S., Handy, M., Legere, V., Farias, N., Murphy, C., . . . Tavares, J. (2019). *Design and Integration of a High Powered Model Rocket.* Worcester: Worcester Polytechnic Institute .

Groh, K. K., & Banks, B. A. (1994). Atomic-Oxygen Undercutting of Long Duration Exposure Facility Aluminized-Kapton Multilayer Insulation. *Journal of Spacecraft and Rockets*.

Harbaugh, J. (2022). *A single RL10 Engine will provide nearly 25000 pounds of thrust and serve as the main propulsion for ICPS that will fly atop the SLS rocket Block 1 in support of each of the first three Artemis missions*. Retrieved from Nasa: https://www.nasa.gov/exploration/systems/sls/fs/rl10engine.html

Hastings, L. J. (2003). *Spray bar zero-gravity vent system for on-orbit liquid.* NASA.

Heaney, J. B. (1998). *Efficiency of Aluminized Mylar Insulation at Cryogenic Temperatures.* SPIE Proceedings.

Hexcel. (2020). *HexTow IM7 Carbon Fiber Data Sheet.* Retrieved from https://www.hexcel.com/user_area/content_media/raw/IM7_HexTow_DataSheet.pdf

Hexcel HexTow IM7 Carbon Fiber - Epoxy Composite. (n.d.). Retrieved from MatWeb Material Property Data: https://www.matweb.com/search/datasheet.aspx?matguid=0a2c4758da1a4e45a7b0750924cf3ce2&n=1&ckck=1

Jianpeng. (n.d.). *Experimental Study on Composite Insulation System of Spray Foam Insulation and Variable Denisty Multilayer Insulation.* Applied Thermal Engineering.

Jones, H. W. (2018, July 7). *The Recent Large Reduction in Space Launch Cost*. Retrieved from Wayback Machine: https://web.archive.org/web/20210801024432/https://ntrs.nasa.gov/citations/2020000109

Kanable, K. (2022, August 5). *Artemis: What you need to know about returning to the moon*. Retrieved from News 19: https://whnt.com/news/technology-and-space/artemis/artemis-what-you-need-to-know-about-returning-to-the-moon/

Krarajgokar, N. (2022). Retrieved from AE 5383 Composite Materials Homework 2.

Krishnan, S. (2010). *Hydrogen Peroxide / Kerosene, Liquid-Oxygen / Kerosene, and Liquid-Oxygen / Liquid Methane for Upper Stage Propulsion* . Skudai: Universiti Teknologi Malaysia.

Lesker, K. J. (2023, Feburary 5). *Thermocouple and Power Feedthroughs* . Retrieved from Kurt J. Lesker Company : https://www.lesker.com/feedthroughs/thermocouple-feedthroughs-typek-miniplug-singleend/part/tft3ky00008a

Li, & Junlan. (2013). Thermal Analysis of Composite Solar Array Subjected to Space Heat Flux. *Aerosapce Science and Technology, Vol. 27*, 84-94.

Liu, N., Ma, B., Liu, F., Huang, W., Xu, B., Qu, L., & Yang, Y. (2021). Progress in research on composite cryogenic propellant tank for large aerospace vehciles. *Composites Part A: Applied Science and Manufacturing*.

M, S. P., & Chollackal, A. (2018). Thermal performance of multilayer insulation: A review. *IOP Conference Series: Materials Science and Engineering*, 9.

Majer, V., & Svoboda, V. (1985). *Enthalpies of Vaporization of Organic Compounds: A Critical Review and Data Compilation.* United Kingdom: Blackwell Scientific.

Marchi, S. C. (2006). Permeability, Solubility, and Diffusivity of ydrogen Isotopes. *International Journal of Hyrdrogen Energy* .

Mayer, I., Lodge-McIntire, G., Levi, E., Kirejczyk, M., LaGrasse, B., Edwards, S., & Zollinger, P. (2021). *Design and Analysis of an Interplanetary SmallSat.* Worcester, MA.

Maynard, O. E. (1966). *Service Module Reaction Control System Propellant Management* . Houston : NASA.

McCarty, R. D. (1975). *Hydrogen Technology Survey: Thermophysical Properties.* NASA NTRS.

McCarville, D. A., Guzman, J. C., Dillon, A. K., Jackson, J. R., & Birkland, J. O. (2019). *Design, Manufacture and Test of Cryotank Components.* NASA.

McCutcheon, K. D. (2022, Aug 3). *U.S. Manned Rocket Propulsion Evolution*. Retrieved from Engine History: https://www.enginehistory.org/Rockets/RPE08.10/RPE08.10.shtml

Meng, J., Zheng, H., Wei, Y., Liu, D., Shi, H., Wang, P., . . . Fang, D. (2022). Leakage Performance of CFRP Laminate Under Cryogenic Temperature: Experimental and Simulation Study. *Composites Science and Technology*, p. 109550–.

Mer, S., Fernandez, D., Thibault, J.-P., & Corre, C. (2016). Optimal design of a Thermodynamic Vent System for cryogenic propellant storage. *Cryogenics*, 127-137.

Mohon, L. (2015, December 7). Retrieved from https://www.nasa.gov/exploration/systems/sls/multimedia/operation-insulation-nasa-marshall-prepares-for-sls-foam-testing.html

Mohon, L. (2017, Aug 7). *Getting to Know You, Rocket Edition: Interim Cryogenic Propulsion Stage*. Retrieved from NASA: https://www.nasa.gov/sls/interim_cryogenic_propulsion_stage_141030.html

NASA. (1969). *Apollo 8 Misison Report* . Houston : NASA.

NASA. (1974). *Introduction to Liquid Helium.* Goddard Space Flight Center.

NASA. (2021, May 13). *Isentropic Flow*. Retrieved from NASA.gov: https://www.grc.nasa.gov/www/k-12/airplane/isentrop.html

NASA Goddard Space Flight Center. (2022, January 5). *Sunshield Successfully Deploys on NASA's James Webb Space Telescope*. Retrieved from Lab Manager: https://www.labmanager.com/news/sunshield-successfully-deploys-on-nasas-james-webb-space-telescope-27327

NASA. (n.d.). *https://cryo.gsfc.nasa.gov/introduction/liquid_helium.html* . Retrieved from Introduction to Liquid Helium.

NASA Johnson Space Center. (2013). *In-Situ Resource Utilization – Mars Atmosphere/Gas Chemical Processing.* . Small Business Innovation Research (SBIR) & Small Business Technology Transfer (STTR) Program.

NASA. (n.d.). Retrieved from Cryogenic Propellant Storage and Transfer Project: https://www.nasa.gov/sites/default/files/files/CPST_Fact_Sheet(1).pdf

Native Dynamics. (2014, March). *Specific Energy and Energy Density of Fuels*. Retrieved from Neutrium: https://neutrium.net/properties/specific-energy-and-energy-density-of-fuels/

Native Dynamics. (2015). *Specific Energy and Energy Density of Fuels.* 26: March.

Neher, R. T. (1971). *Scholarly Commons*. Retrieved from https://commons.erau.edu/space-congress-proceedings/proceedings-1971-8th/session-4/1

NPTEL. (n.d.). *Module 5: Laminate Theory / Lecture 16: Introduction to Classical Plate Theory*. Retrieved from archive.nptel.ac.in: https://archive.nptel.ac.in/content/storage2/courses/101104010/lecture16/16_1.htm

Olliges, R. (2019, January 17). *Carbon Fiber Weaves: What they are and why to use them*. Retrieved from Elevated Materials: https://www.elevatedmaterials.com/carbon-fiber-weaves-what-they-are-and-why-to-use-them/

OnlineMetals. (n.d.). *Aluminum 2024-O/T3/T4/351/851 Product Guide*. Retrieved from OnlineMetals.com: https://www.onlinemetals.com/en/product-guide/alloy/2024#specs

OnlineMetals. (n.d.). *Aluminum 2024-O/T3/T4/351/851 Product Guide*. Retrieved from OnlineMetals.com: https://www.onlinemetals.com/en/product-guide/alloy/2024#specs

Ortega, & Juan. (2017). Analysis of the Temperature of a 1U CubeSat Due to Radiation in Space. *Advances in Structural Engineering and Mechanics (ASEM17)*.

PMD Tanks. (n.d.). Retrieved from Northrop Grumman: https://www.northropgrumman.com/space/pmd-tanks/

Prasad, N. E., & Wanhill, R. H. (2017). *Aerospace Materials and Material Technologies.* Springer.

Richards, R. J., Jacobs, R. B., & Steward, W. G. (1962). *A SURVEY OF THE LITERATURE ON HEAT TRANSFER FROM SOLID SURFACES TO CRYOGENIC FLUIDS.* Washington, D. C.: UNITED STATES DEPARTMENT OF COMMERCE OFFICE OF TECHNICAL SERVICES.

Ring, E. (1964). *Rocket Propellant and Pressurization Systems.* New Jersey: Prentice-Hall Inc.

Rockwest Composites. (n.d.). *14077-D-Group*. Retrieved from Rock West Composites: https://www.rockwestcomposites.com/14077-d-group

Roder, H. M., & Weber, L. A. (1972). *ASRDI Oxygen Technology Survey Volume I: Thermophysical Properties.* Washington D.C.: NASA.

Ross Jr, R. G. (2015). Quantifying MLI Thermal Conduction in Cryogenic Applications from Experimental Data. *Jet Propulsion Laboratory*, 8.

Ross, R. G. (2015). Quantifying MLI Thermal Conduction in Cryogenic Applications from Experimental Data. *IOP Conference Series: Material Science and Engineering, Vol 101*, (pp. 012-017).

Rudman, T. J., & Austad, K. (2002). *Alternate Wars*. Retrieved from https://www.alternatewars.com/BBOW/Boosters/Centaur/TheCentaurUpperStageVehicleHistory.pdf

Rule, D. L. (1996). Thermal Conductivity of Polypyromellitimide Film with Alumina Filler Particles from 4.2 to 300 K. *Cryogenics, Vol 36*, 283-290.

S-2 Glass Fiber. (n.d.). Retrieved from MatWeb Material Property Data: https://www.matweb.com/search/DataSheet.aspx?MatGUID=881df8cd9bde4344820202eb6d1e7a39&ckck=1

Stefansson, G. (2014, September 29). *MLI Blankets*. Retrieved from Pennsylvania State University : https://hpf.psu.edu/2014/09/29/mli-blankets/

Sutheesh, P. M., & Chollackal, A. (2018). *Thermal performace of multilayer insulation: A review*. IOP Conf. Series: Material Science and Engineering .

Sutton, G., & Biblarz, O. (2017). *Rocket Propulsion Elements.* Hoboken: John Wiley & Sons Inc.

TOPOLOCFRT. (n.d.). *UD Tapes*. Retrieved from TOPOLO: https://topolocfrt.com/ud-tapes/

University of Wisconsin-Stevens Point. (n.d.). *Energy Education: Concepts and Practices*. Retrieved from UWSP: https://www3.uwsp.edu/cnr-ap/KEEP/nres633/Pages/Unit2/Section-B-Energy-Transfer.aspx

Wang, B., & Lantz, D. (2021, April 26). *Delta IV Heavy Retiring and the Vulcan Replacement*. Retrieved from Next Big Future: https://www.nextbigfuture.com/2021/04/delta-iv-heavy-retiring-and-the-vulcan-rep

Wellen Tech. (n.d.). *Peltier Technology*. Retrieved from http://www.wellentech.com/peliter-tech.html

Werner, E., & Bolt, H. (2006). Thermomechanics of Fibre Reinforced Epoxies for. https://doi.org/https://d-nb.info/985154608/34

Wertz, J. R., Everett, D. F., & Puschell, J. J. (2011). *Space Mission Engineering: The New Smad.* Microcosm Pres.

Wittry. (2009, May 20). *Hubble's New Covers Provide Blanket of Protection*. Retrieved from NASA: https://www.nasa.gov/mission_pages/hubble/servicing/series/hubble_blanket.html.

Zona, K. (2010). *Liquid Hydrogen--the Fuel of Choice for Space Exploration.* https://www.nasa.gov/topics/technology/hydrogen/hydrogen_fuel_of_choice.html: NASA.

6 Appendix

6.1 Composite Curing Procedure

Safety Hazards Associated with Composite Curing

Irritant

R-phrases: R36 Irritate to eyes.
R-38 Irritating to skin

SKIN: May cause skin irritation. Mechanical irritation may occur from carbon fiber abrading or becoming imbedded in the skin. Chemical irritation may occur from exposure to sizing present on the carbon fiber.

EYES: Fragments of this product may cause mechanical eye irritation. Chemical irritation may occur from exposure to sizing present on the carbon fiber.

INHALATION: Inhalation exposure to respirable fibers of this product is not expected to occur under normal industrial conditions. Under very limited circumstances, however, exposure to respirable fibers of this product can occur and may result in respiratory tract irritation.

INGESTION: Not expected to occur during industrial activities since ingestion is not a relevant route of exposure.

CHRONIC EFFECTS/CARCINOGENICITY: Not regulated as a carcinogen. There are no chronic effects/carcinogenicity data are available on this product. Under very limited circumstances, exposure to respirable fibers of this product can occur and may result in respiratory tract irritation; prolonged exposure may result in more adverse effects. See Section 11 – *Toxicological Information* for information on subchronic toxicity.

NTP: *Not listed*
IARC: *Not listed*
OSHA: *Not listed*

MEDICAL CONDITIONS AGGRAVATED BY EXPOSURE: None known.

INCOMPATIBILITY: None known.

SIGNS AND SYMPTOMS OF EXPOSURE: May result in slight skin and eye irritation.

FIRST AID MEASURES

S-phrases: S24 Avoid contact with skin.
S25 Avoid contact with eyes.
S28 After contact with skin, wash immediately with plenty of soap-suds.
S33 Take precautionary measures against static discharges.

SKIN: Wash fibers off of skin with water and soap. If fibers are imbedded in the skin, remove with tweezers. Discard clothing that may contain imbedded fibers. Get medical attention if exposure results in adverse effects.

EYES: Immediately flush with a continuous water stream for at least 20 minutes. Washing immediately after exposure is expected to be effective in preventing damage to the eyes. Get medical attention.

INHALATION: If there is inhalation exposure to the fibers of this product, remove source of exposure and move victim to fresh air. If not breathing give artificial respiration. If there is breathing difficulty, give oxygen. Get immediate medical attention for any respiratory problems.

INGESTION/SWALLOWED: Not expected to occur since ingestion is not a likely route of exposure for this product. If ingestion does occur, do not induce vomiting. Nothing by mouth if unconscious. Get immediate medical attention.

Materials:

- Nylon Film Roll
- Breather Fabric Roll
- Release Fabric Roll
- Sealant Tape Roll
- Vacuum Connector
- Mold Plate (6x6 inches)
- Prepreg
- Plastic Wedge
- Vacuum
- Vacuum Tube
- Composite Curing Oven
- Mold Release Agent
- Isopropyl Alcohol
- Clean Microfiber Cloth
- Oven Mittens
- Compressed Air

1. Cut nylon film into one 32x12-inch sheet
2. Cut release fabric into one 7x7-inch sheet
3. Cut breather fabric into one 7x7-inch sheet
4. Clean the surface of the mold plate that the prepreg will be laid on with isopropyl alcohol and microfiber cloth
5. Apply 3-4 coats of a mold release agent to mold plate and buff off after each coat dries (5-10 minutes)
6. Lay up prepreg on the center of the mold plate in the following stacking sequence: $[0/90]_4$
    a. Laminate area should be 4x4 inches
7. Lay the 32x12 inch nylon film flat on a level table and place the mold plate, with the laminate, centered on top of one half of the nylon film. See apparatus for reference.
8. Place release fabric centered **over** the mold plate with composite laminate.
9. Apply breather fabric on top of the release fabric. If the prepreg is deemed to have too much resin, a second 7x7 inch breather fabric may be placed on top of the first one.
10. Place vacuum connector on top of the nylon film from Step 9. Offset it from the mold plate by 4 inches.
11. Lay the sealant tape on the inside perimeter of the nylon film, around the mold plate, offset inward by 1 inch. See apparatus for reference.
12. Fold the second half of the nylon film over materials laid out from Steps 7-11, lightly sealing the edge of it to the vacuum sealant tape as you work, so you can easily remove and re-position it, if necessary. Wait until the bag is fully in place before firmly pressing on the sealant tape. Ensure that there are no gaps between the bag and the sealant tape to prevent air leaking into the bag.
13. Cut a small hole or cross-section in the bag where the upper portion of the vacuum connector will attach to the vacuum tube.

14. Attach one end of the vacuum tube to the vacuum connector. Attach the other end to the vacuum pump.
15. Turn on the vacuum pump and slowly remove the air from the bag. Apply full vacuum pressure once you are satisfied with the placement of the bag.
16. When the bag is air-tight, twist the vacuum connector to lock it and prevent air from leaking into the bag.
17. Turn off the vacuum and disconnect the vacuum tube from the vacuum connector.
18. Check for air leaks.
19. If leaks are present, discard the nylon film and sealant tape, and repeat Steps 7-18 with a new 32x12 nylon film
20. If no leaks are present, place the sealed nylon bag into the curing oven.
21. The oven curing process is as follows:
    a. This is a standard 250°F cure profile.
    b. Full Vacuum bag pressure for entire cure cycle, Autoclave if possible up to 100 psi, min 40 psi.
    c. 5° per minute ramp rate (do not pre-heat the oven)
    d. 250° hold for 120 mins after part reaches 250° (sometimes the part lags the oven temperature)
    e. 5° per minute cool down rate (leave in oven and let it cool down slowly)
    f. Keep under vacuum until part temp reaches 130° minimum.
22. Discard the vacuum bagging materials.
    a. DO NOT discard the mold plate with the composite laminate or the vacuum connector!
23. Use a plastic wedge to remove the part from the mold. You may need the assistance of compressed air to remove the part from the mold plate.
24. Composite laminate is now ready to be tested for permeability.

6.2 Multilayer Insulation Construction Procedure

1. Cut Mylar sheet into 11 or more square pieces with side length near 100 mm each
2. Cut polyester netting into 10 or more square pieces of similar size to that of the Mylar pieces
3. Stack the Mylar and polyester pieces on top of one another, alternating which material is placed with each layer
    a. The completed MLI blanket should have a Mylar piece on each side of the blanket, such that both sides are covered by a reflective layer
4. Pin the MLI blanket into place and make sure the layers are all lined up
    a. This step is important if the MLI must be transported before completion of the next steps

5. Sew the MLI blanket together; this can be done either by hand or with a sewing machine, however if using a sewing machine, one must take extra care to ensure the layers do not shift during the process
6. After completion of the assembly steps, one must cut the MLI blanket to the size necessary for their experiment, ensuring the stitching does not impede over the surface for which the blanket is intended to insulate

6.3 Thermal Testing Procedure

1. The following specimens will be tested in the following procedure:
    - Single CFRP Sheet
    - Single Al-2024 sheet
    - CFRP sheet with mylar insulation
    - AL-2024 with mylar insulation
    - CFRP sheet with polyurethane insulation
    - AL-2024 with polyurethane insulation
    - CFRP sheet with polyurethane insulation and Mylar insulation
    - Al-2024 sheet with polyurethane insulation and Mylar insulation

2. For each specimen, a COMSOL analysis will be run with the same boundary conditions as provided by the testing apparatus. The following must be known,
    - The heat flux through the specimen
    - The time it takes for heat flux to reach equilibrium.
3. The specimen, with two thermocouples, adhering to each side, will be laid on top of the cold plate.
4. The apparatus will be placed under the heat lamp, then inserted into the vacuum chamber.
5. With the vacuum pulled, flux is applied to the heat lamp, and collate applying a constant temperature to the rear side of the specimen, all boundary conditions are met.
6. The test will run for a determined amount of time, defined by initial tests to see how long most specimens take to equalize.
7. The vacuum will be released and all data acquisition will conclude.

Analysis:

1. With the temperature data recorded for each experiment, the thermal conductivity can be found using the law of conduction, temperature data, flux applied, and physical geometry of the plate.
2. These results will be compared to the ones found in COMSOL to see if these models are accurate in calculating the amount of heat transfer through various types of tanks walls
3. If these measurements are representative of the simulations, they can then be used to model the amount of boiloff expected in a tank using similar types of materials.
    - These results will allow us to determine the best material and combinations to reduce or slow the heat flux through the tank walls.

6.4 Thermal Testing Microcontroller Script

```
#include "max6675.h"
#include <SPI.h>
#include <SD.h>



//SD Card
const int chipSelect = 10;

const int RELAY_PIN = 8;

// Temperature Sensor1
int thermo1D0 = 4; // so
int thermo1CS = 6;
int thermo1CLK = 5; // sck
MAX6675 thermocouple1(thermo1CLK, thermo1CS, thermo1D0);


// Temperature Sensor2

int thermo2CS = 7;
MAX6675 thermocouple2(thermo1CLK, thermo2CS, thermo1D0);


void setup()
{
  Serial.begin(9600);
  pinMode(RELAY_PIN, OUTPUT);


 while (!Serial) {
    ; // wait for serial port to connect. Needed for native USB
  }
  Serial.print(F("Initializing SD card..."));
  if (!SD.begin(chipSelect)) {
    Serial.println(F("initialization failed!"));
    return;
  }
  Serial.println(F("initialization done."));

}

void loop()
{

  String data = String(millis()/1000) + "," +
String(thermocouple1.readCelsius()) + "," +
String(thermocouple2.readCelsius());
  File dataFile = SD.open("data.csv", FILE_WRITE);
  if (dataFile) {
    dataFile.println(data);
    dataFile.close();
```

```
  } else {
    Serial.println(F("Error opening data file"));
  }
```

```
  Serial.print(thermocouple1.readFahrenheit());
  Serial.print(F(","));
  Serial.println(thermocouple2.readFahrenheit());
  delay(3000);

if (thermocouple2.readFahrenheit() <= 60)
  {digitalWrite(RELAY_PIN, LOW);}
  else if (thermocouple2.readFahrenheit() > 60)
   {digitalWrite(RELAY_PIN, HIGH);}
```

6.5 Permeability Testing Data

Al 2024 -

AL 2024		Before Spike	After Spike										
Time (min)		0	0	1	2	3	4	5	6	7	8	9	10
Upstream Pressure (psig)	4.6	21	49	49	49	49.5	49.5	49.5	49.5	49.5	50	50	50
	8.3	24	73	74	74	74	74.5	74.5	74.5	75	75	75	75.5
	10.9	21	84	85	85.5	86	86	86	86	86	86	86	86.5
	14.65	21	105	106.5	107	107.5	107.5	108	108	108.5	109	109	109
	20	20	125	128	129	129.5	129.5	129.5	130	130	130.5	131	131
		Height (mm)											

CFRP-6 -

CFRP (6 Ply)	Before Spike	After Spike										
Time (min)	0	0	1	2	3	4	5	6	7	8	9	10

Upstream Pressure (psig)	0.4	23	28	50	76	92	104	114	122	126	129	131	132
	0.7	25	33	71	106	133	162	181	204.5	219	228.5	235	239
	0.9	22	39	108	159	198	229	251	269	281	289	295	299
	1.2	20	46	134	198	249	288						
	1.5	21	55	163	244	306							
	1.6	21	61	181	271								
	2.2	21.5	86	256									
	2.6	20	95	295									

CFRP-8 -

CFRP (8 Ply)		**Before Spike**	**After Spike**										
Time (min)		0	0	1	2	3	4	5	6	7	8	9	10
Upstream Pressure (psig)	4.6	25	51	56	58	60	62	64	65	66.5	68	69.5	70
	8	21	68	73	76	78	81	84	86	88.5	90.5	92.5	94.5
	12.5	19	91	101	108	114.5	120	125.5	130.5	136	140	144.5	148.5
	14.8	20	102	112	120	126.5	133	139	145.5	151.5	156.5	161.5	166.5
	20	21	129	141	151	159	167	174	181	187	193	199	205

6.6 Valve Testing Script and Procedure

Materials:

- Pressurized air tank
- Sonic nozzle

- Air hose
- Nut connecter (x2)
- Pressurized air source
- Pressure transducer
- Arduino
- Power supply
- Solenoid valve
- Fixed size orifice
- Flow meter
- Pressure Regulator

CVS Test Procedure:

1. Set up the system as shown in Figure 41. Connect the air hose to the pressurized air hose. Connect the other end of the air hose to the sonic nozzle and screw into the pressurized air tank. Attach the solenoid valve to the tank and the orifice to the valve. Set up the pressure transducer and Arduino as shown in Figure 41.
2. Calibrate the pressure sensor by pressurizing the tank and recording the voltage that corresponds to the value on the pressure transducer.
3. Use the pressure regulator to set the back pressure to 30 psig.
4. Begin recording data, then with the solenoid valve open, begin to pressurize the tank until the pressure in the tank no longer increases.
5. Continue to record data for 1-2 minutes.
6. Close the input valve and allow the tank pressure to return to 0 psig.
7. Repeat with back pressures of 60, 90, and 110 psig.

Emergency Valve Test Procedure:

1. Set up the system the same as above without the orifice.
2. Write the code shown below.
3. Pressurize the tank and run the code.

```
#include "Wire.h" //allows communication over i2c devices

const int pressureInput = A0; //select the analog input pin for the
pressure transducer
const int pressureZero = 102; //analog reading of pressure transducer at
0psi
const int pressureMax = 935.5; //analog reading of pressure transducer at
100psi
const int pressuretransducermaxPSI = 100; //psi value of transducer being
used
const int baudRate = 9600; //constant integer to set the baud rate for
serial monitor
const int sensorreadDelay = 1000; //constant integer to set the sensor
read delay in milliseconds
const int RELAY_PIN = 3;  // the Arduino pin, which connects to the IN
pin of relay

//515 at 50 psig

float pressureValue = 0; //variable to store the value coming from the
pressure transducer


void setup() //setup routine, runs once when system turned on or reset
{
  Serial.begin(baudRate); //initializes serial communication at set baud
rate bits per second
   pinMode(RELAY_PIN, OUTPUT);
}

void loop() //loop routine runs over and over again forever
{

  pressureValue = analogRead(pressureInput); //reads value from input pin
and assigns to variable
  pressureValue = ((pressureValue-
pressureZero)*pressuretransducermaxPSI)/(pressureMax-pressureZero);
//conversion equation to convert analog reading to psi
  Serial.print(pressureValue, 1); //prints value from previous line to
serial
  Serial.println("psi"); //prints label to serial
  delay(sensorreadDelay); //delay in milliseconds between read values

   if (pressureValue > 0) {
    digitalWrite(RELAY_PIN, HIGH);
  }
  else {
    digitalWrite(RELAY_PIN, LOW);
  }



}
```

6.7 Boil-Off Model MATLAB Script

```
function BoilOffCalc()
% Clear command window and close all open figures
clc; close all;

% Open File for capturing output
% dfile ='Output.txt';
% if exist(dfile, 'file') ; delete(dfile); end
% diary(dfile)

% Set Fsolve options
options = optimset('Display','off');

% Turn to true to plot results
plot_true = false;

%%  Set Input Parameters
%--------------------------------------------------------------------------%
    % Propellant Mass Range (min, step, max)
    mp_ = [844, 1, 844];

    % Oxidizer : Fuel Mass Ratio (XX:1)
    prop_rat    = 3.857;
    % Select Fuel (1 == LH2, 2 == LCH4)
    FuelConfig  = 2;

    % Select Tank Material (1 == AA 2024 T3, 2 = Grafil 34-700)
    MatConfig   = 2;

%--------------------------------------------------------------------------%

%%   Governing Parameters
    fprintf('Oxidizer:Fuel mass Ratio -- %g:1',prop_rat)

    FuelProps   = get_fuel_properties(FuelConfig);              % [rho, hvap, ISP,
mixrat]
        %   Load Fluid Thermophysical Properties
        rho_fuel    = FuelProps(1); h_vap_fuel  = FuelProps(2);
        ISP         = FuelProps(3); mix_rat     = FuelProps(4);
        m_thruster  = FuelProps(5);


    rho_wall    = get_tank_material_properties(MatConfig);

%%   Mission Parameters

    %   Heat Flux incident on Fluid
    Q_in   = 34;            % Heat entering tank [W/m2]

    %   Delta V and mission times
    DV1     = 973.6;        % Delta-V for lunar capture [m/s]
    DV2     = 999.4;        % Delta-V for lunar escape [m/s]
    DVs     = [DV1, DV2];
```

```
    t_DV1   = 73*3600;      % Time of lunar capture burn [s]
    t_DV2   = 97*3600;      % Time of lunar escape burn [s]
    t_f     = 3600*149;     % Mission Duratation [s]
    t_init  = 0;            % Initial time for calculation [s]
    g = 9.81;               % Gravity

%%  ITERATE PROPELLANT MASS

for m_ptotal = mp_(1):mp_(2):mp_(3)

    do_final_calc = false;

%%   Fuel Tank Parameters

    %   Tank Parameters
    perFuel     = 1/(prop_rat + 1);     % Percent of propellant that is Fuel;
    mp0_fuel    = m_ptotal*perFuel;     % Initial fuel mass [kg]

    [m_fuel_tank, r_fuel] = tank_sizing(rho_wall, mp0_fuel, rho_fuel);


    %   Calculate Initial Height of Fuel and Boil Off Rate
    h0_guessF   = 1.5*r_fuel;   % Initial fluid height guess [m]
    h0_fuel     = fsolve(@(h)
calc_height(h,r_fuel,mp0_fuel,rho_fuel),h0_guessF,options);
    BOR0_fuel   = (Q_in*(2*pi*r_fuel*h0_fuel))/h_vap_fuel;


%%   Oxidizer [LOx] Tank Parameters

    %   Get Fluid Thermophysical Properties
    rho_LOx     = 1149;             % Propellent density [kg/m3]
    h_vap_LOx   = 214*1000;         % Enthalpy of vap [J/kg]

    rho_oxi     = rho_LOx; h_vap_oxi = h_vap_LOx;
    perOxi      = 1-1/(prop_rat + 1);       % Percept of propellant that is Oxidizer;
    mp0_oxi     = m_ptotal*perOxi;          % Initial oxidizer mass [kg]

    [m_oxi_tank, r_oxi]  = tank_sizing(rho_wall, mp0_oxi, rho_oxi);

    %   Calculate Initial Height of Fuel and Boil Off Rate
    h0_guessO   = 1.5*r_oxi;        % Initial fluid height guess [m]
    h0_oxi      = fsolve(@(h)
calc_height(h,r_oxi,mp0_oxi,rho_oxi),h0_guessO,options);
    BOR0_oxi    = (Q_in*(2*pi*r_oxi*h0_oxi))/h_vap_oxi;


%% Rocket Parameters

    % Thruster Propellant Mixture Ratio
    perburnFuel     = 1/(mix_rat + 1);   % Percent of propellant that is Fuel
    perburnOxi      = 1-1/(mix_rat + 1); % Percept of propellant that is Oxidizer

    % Additional Spacecraft Dry Mass
```

```
    m_extra     = 500;                  % Subsystem / Payload mass (assumed value)
[kg]

    m_wet0sc    = m_fuel_tank + m_oxi_tank + m_thruster + m_extra + m_ptotal;
% Initial Mass of S/C [kg]
    m_drysc     = m_wet0sc - m_ptotal;
    fprintf('\n-----------------------------------------------\n\n')
    fprintf('\nFor mp = %g [kg], S/C wet mass is %g [kg]', m_ptotal, m_wet0sc)


%%   Iterative ODE Solver

    % Allocate Memory for Data Collection
    dt          = 0.1;
    n_time_pts  = t_f / dt + 1;
    t_record    = zeros(1, n_time_pts); %   allocates memory for inputs times
    fuel_data   = zeros(3, n_time_pts); %   allocated memory for all states related
to the fuel tank
    oxi_data    = zeros(3, n_time_pts); %   allocated memory for all states related
to the oxidizer tank
    m_pburn     = zeros(1, length(DVs)); %  allocated memory for DV burn mass
    % such that (1) = height; (2) = mass; (3) = BOR

    %   Record Initial Data
    fuel_data(1:3, 1) = [h0_fuel   ;mp0_fuel   ;BOR0_fuel ];
    oxi_data(1:3, 1)  = [h0_oxi    ;mp0_oxi    ;BOR0_oxi  ];
    t_record(1, 1)  = t_init;
    column_number   = 1;

    %   Set inital values
    h_fuel  = h0_fuel;
    mp_fuel = mp0_fuel;
    h_oxi   = h0_oxi;
    mp_oxi  = mp0_oxi;

%     fprintf('\nInitial mp [Fuel, Oxidizer] = [%g, %g] [kg]', mp0_fuel, mp0_oxi)
%     fprintf('\nInitial BOR [Fuel, Oxidizer] = [%g, %g] [g/s]\n', BOR0_fuel*1000,
BOR0_oxi*1000)

for t = t_init:dt:t_f

        % Accounting for Delta-V Burns in fluid mass and height
        if (t == t_DV1)
           n = 1;
           [mp_fuel, mp_oxi, failcheck, m_burn, m_sc] = executeDeltaV(ISP, DVs(n),
m_drysc, mp_fuel, mp_oxi, perburnFuel, perburnOxi);
           failFuel = failcheck(1); failOxi = failcheck(2);
           m_pburn(n) = m_burn;
%            fprintf('\nExecuted burn %g',n);

           if (failFuel || failOxi == true)
               fprintf('\nFailed burn %g: m [Fuel, Oxidizer] = [%g, %g] [kg]', n,
mp_fuel, mp_oxi)
               break
           else
```

```
                fprintf('\nSuccessful Burn %g: m [Fuel, Oxidizer] = [%g, %g] [kg]', n,
mp_fuel, mp_oxi)
            end

             h_fuel     = fsolve(@(h)
calc_height(h,r_fuel,mp_fuel,rho_fuel),h0_guessF,options);
             h_oxi      = fsolve(@(h)
calc_height(h,r_oxi,mp_oxi,rho_oxi),h0_guessO,options);

        elseif (t == t_DV2)
            n = 2;
            [mp_fuel, mp_oxi, failcheck, m_burn, m_sc] = executeDeltaV(ISP, DVs(n),
m_drysc, mp_fuel, mp_oxi, perburnFuel, perburnOxi);
            failFuel = failcheck(1); failOxi = failcheck(2);
            m_pburn(n) = m_burn;
%             fprintf('\nExecuted burn %g',n);

            if (failFuel || failOxi == true)
                fprintf('\nFailed burn %g: [m_fuel = %g, m_oxi = %g]', n, mp_fuel,
mp_oxi)
                break
            else
                mp_fuel_req = mp_oxi/mix_rat;
                DVremain = -log((m_drysc + mp_fuel_req)/m_sc)*g*ISP;

                fprintf('\nSuccessful Burn %g: m [Fuel, Oxidizer] = [%g, %g] [kg]\n',
n, mp_fuel, mp_oxi)
                fprintf('                   m [Fuel, Oxidizer] = [%g : %g] \n',
mp_fuel/mp_fuel, mp_oxi/mp_fuel)
                fprintf('                   DeltaV Remaining = %g [m/s]\n', DVremain)
                fprintf('                   m Fuel Remaining = %g [kg] = %g%%
[mp_fuel_0]\n', mp_fuel_req,mp_fuel/(mp0_fuel)*100)
                do_final_calc = true;

            end

             h_fuel     = fsolve(@(h)
calc_height(h,r_fuel,mp_fuel,rho_fuel),h0_guessF,options);
             h_oxi      = fsolve(@(h)
calc_height(h,r_oxi,mp_oxi,rho_oxi),h0_guessO,options);

        else
            % Calculate instantaneous propellant mass based on height

            mp_fuel = rho_fuel*pi*r_fuel*h_fuel^2 - (1/3)*rho_fuel*pi*h_fuel^3 ;
            mp_oxi  = rho_oxi*pi*r_oxi*h_oxi^2 - (1/3)*rho_oxi*pi*h_oxi^3 ;

        end

    % Runge-Kutta Method ODE Solver for Fuel Tank
        k1f          = dt*ODE(h_fuel             ,r_fuel,h_vap_fuel,rho_fuel,Q_in);
        k2f          = dt*ODE(h_fuel + (1/2)*k1f ,r_fuel,h_vap_fuel,rho_fuel,Q_in);
        k3f          = dt*ODE(h_fuel + (1/2)*k2f ,r_fuel,h_vap_fuel,rho_fuel,Q_in);
        k4f          = dt*ODE(h_fuel +       k3f ,r_fuel,h_vap_fuel,rho_fuel,Q_in);
```

```
        h_fuel_plusdt   = h_fuel + (1/6)*k1f + (1/3)*k2f + (1/3)*k3f + (1/6)*k4f; %
Finite difference "step"

    % Runge-Kutta Method ODE Solver for Fuel Tank
        k1o          = dt*ODE(h_oxi             ,r_oxi,h_vap_oxi,rho_oxi,Q_in);
        k2o          = dt*ODE(h_oxi + (1/2)*k1o ,r_oxi,h_vap_oxi,rho_oxi,Q_in);
        k3o          = dt*ODE(h_oxi + (1/2)*k2o ,r_oxi,h_vap_oxi,rho_oxi,Q_in);
        k4o          = dt*ODE(h_oxi +       k3o ,r_oxi,h_vap_oxi,rho_oxi,Q_in);

        h_oxi_plusdt   = h_oxi + (1/6)*k1o + (1/3)*k2o + (1/3)*k3o + (1/6)*k4o; %
Finite difference "step"

    % Iterative Steps
        column_number   = column_number + 1;
        h_fuel  = h_fuel_plusdt;
        h_oxi   = h_oxi_plusdt;

        if h_oxi < 0
            h_oxi = 0;
            mp_oxi = 0;
            BOR_oxi = 0;
        else
            SA_oxi  = 2*pi*r_oxi*h_oxi;
            BOR_oxi   = Q_in*SA_oxi / h_vap_oxi;

        end

        if  h_fuel < 0
            h_fuel = 0;
            mp_fuel = 0;
            BOR_fuel = 0;
        else
            SA_fuel = 2*pi*r_fuel*h_fuel;
            BOR_fuel  = Q_in*SA_fuel / h_vap_fuel;

        end

    % Data Recording
        fuel_data(:, column_number) = [h_fuel   ;mp_fuel   ;BOR_fuel ];
        oxi_data(:, column_number)  = [h_oxi    ;mp_oxi    ;BOR_oxi  ];
        t_record(1, column_number)  = t;


end

if do_final_calc
    mfuelBO = mp0_fuel - fuel_data(2,end) - m_pburn(1)*perburnFuel -
m_pburn(2)*perburnFuel;
    moxiBO =  mp0_oxi - oxi_data(2,end) - m_pburn(1)*perburnOxi -
m_pburn(2)*perburnOxi;
    fprintf('\nBoil Off [Fuel, Oxidizer] = [%g, %g] [kg] \n', mfuelBO, moxiBO)

end
    if plot_true == true
        Do_Plotting
```

```
    end

end
function Do_Plotting(t_record, fuel_data, oxi_data)
%% Plot Fuel Parameters
figure(1)
subplot(3,1,1)
title('LH_2 Height, Mass, and Boil-Off Rate Over Mission Duration')
hold on
    plot(t_record/(24*3600), fuel_data(1 , :), 'LineWidth', 2);
    xlabel('Time (day)'); ylabel('Fluid height h (m)');
    yline(0)
    yline(2*r_fuel)
    xline(t_f/(24*3600))
hold off

subplot(3,1,2)
hold on
    plot(t_record/(24*3600), fuel_data(2 , :), 'LineWidth', 2);
    xlabel('Mission Time (day)'); ylabel('Fluid Mass (kg)')
    xline(t_f/(24*3600))
hold off


subplot(3,1,3)
hold on
    plot(t_record/(24*3600), fuel_data(3 , :), 'LineWidth', 2);
    xlabel('Mission Time (day)'); ylabel('Fluid Boil-Off Rate (kg/s)')
    xline(t_f/(24*3600))
hold off

%% Plot Oxidizer Parameters
figure(2)
subplot(3,1,1)
title('LOx Height, Mass, and Boil-Off Rate Over Mission Duration')
hold on
    plot(t_record/(24*3600), oxi_data(1 , :), 'LineWidth', 2);
    xlabel('Time (day)'); ylabel('Fluid height h (m)');
    yline(0)
    yline(2*r_oxi)
    xline(t_f/(24*3600))

hold off

subplot(3,1,2)
hold on
    plot(t_record/(24*3600), oxi_data(2 , :), 'LineWidth', 2);
    xlabel('Mission Time (day)'); ylabel('Fluid Mass (kg)')
    xline(t_f/(24*3600))
hold off


subplot(3,1,3)
hold on
    plot(t_record/(24*3600), oxi_data(3 , :), 'LineWidth', 2);
```

```
    xlabel('Mission Time (day)'); ylabel('Fluid Boil-Off Rate (kg/s)')
    xline(t_f/(24*3600))
hold off

end

% diary off
end


%% Functions

function h_dot = ODE(h_t,r,hvap,rho,Q)
      h_dot = 2*Q*r / (rho*hvap*(-2*r+h_t));
end

function f = calc_height(h,r,m,rho)

    f = (1/3)*pi*h^2*(3*r-h)-m/rho;

end

function P = get_fuel_properties(config)

    % Fluid 1 - Fuel [LH2]
    rho_LH2     = 71;               % Propellent density [kg/m3]
    h_vap_LH2   = 446.1*1000;       % Enthalpy of vap [J/kg]
    ISP_LH2     = 450;              % ISP of Spacecraft with Liquid Hydrogen [s]
    mr_H2_LOx   = 5.5;              % Mixutre ratio of propellant for Liquid Oxygen
to Liquid Hygrogen (XX:1)
    m_RL10      = 190.5;            % Thruster Mass [kg]

    % Fluid 2 - Fuel [LCH4]
    rho_LCH4     = 1149;             % Propellent density [kg/m3]
    h_vap_LCH4   = 509*1000;         % Enthalpy of vap [J/kg]
    ISP_LCH4     = 362;              % ISP of Spacecraft with Liquid Methane [s]
    mr_LCH4_LOx  = 3.4;              % Mixutre ratio of propellant for Liquid Oxygen
to Liquid Methane (XX:1)
    m_M10        = 260;              % Thruster Mass [kg]


    if config == 1
        fprintf('\nSelected Fuel: LH2')
        rho = rho_LH2; hvap = h_vap_LH2; ISP = ISP_LH2; mixrat = mr_H2_LOx; mthruster
= m_RL10;
    elseif config == 2
        fprintf('\nSelected Fuel: LCH4')
        rho = rho_LCH4; hvap = h_vap_LCH4; ISP = ISP_LCH4; mixrat = mr_LCH4_LOx;
mthruster = m_M10;
    end

    P = [rho, hvap, ISP, mixrat, mthruster];

end
```

```
function rho = get_tank_material_properties(config)
    % Material 1 - AA 2024-T3
    rho_AA2024     = 2768;              % Material density [kg/m3]

    % Material 2 - Grafil 34-700 CFRP
    rho_Grafil     = 1530;              % Material density [kg/m3]

    if config == 1
        fprintf('\nSelected Tank Material: AA 2024-T3\n')
        rho = rho_AA2024;
    elseif config == 2
        fprintf('\nSelected Tank Material: Grafil 34-700 CFRP\n')
        rho = rho_Grafil;
    end

end

function [m, r] = tank_sizing(rho_mat, m_fluid, rho_fluid)
    %   Tank Sizing
    Fsafety = 1.05;      % Fuel tank volume safety factor

    V_fluid     = (m_fluid/rho_fluid);          % Fluid volume [m^3]
    V_tank      = Fsafety*V_fluid;              % Tank volume [m^3]
    r           = ((3/4)*(1/pi)*V_tank)^(1/3);  % Tank radius [m]

    % Tank Wall Thickness (Assumed 1mm regardless of tank material)
    t = 0.001; % m

    % Mass Factor (For PMD, Mounting Components, etc)
    MF = 1.25;

    % Tank (internal) Surface Area
    SA = 4*pi*r^2;

    m_tank = rho_mat*t*MF*SA;    % Tank mass [kg]

    % MLI Parameters
    rho_MLI     = 658;                          % MLI density [kg/m^3]
    t_MLI       = 0.02;                         % MLI thickness [m]
    r_MLI       = r + t + t_MLI;                % Radius of tank with MLI [m]
    r0          = r + t;                        % Radius of tank without MLI [m]
    V_MLI       = (4/3)*pi*((r_MLI^3)-(r0^3)); % MLI Volume [m^3]
    m_MLI       = rho_MLI*V_MLI;                % MLI Mass

    m           = m_tank + m_MLI;               % Total tank mass
end

function [mp_fuelf, mp_oxif, failcheck, mp_burn, m_sc] = executeDeltaV(ISP, DV,
m_sc_dry, mp_fueli, mp_oxii, perburnFuel, perburnOxi)
    g = 9.81;           % Gravity [m/s^2]

    % Apply Rocket Equation
       M_i      = m_sc_dry + mp_fueli + mp_oxii;
       M_f      = M_i * exp(-DV/(ISP*g));
       mp_burn  = M_i - M_f;
```

```
        mp_fuelf = mp_fueli - mp_burn*perburnFuel;
        mp_oxif  = mp_oxii - mp_burn*perburnOxi;
        m_sc     = M_f;

    if mp_fuelf < 0
           failcheck(1)= true;
        else
           failcheck(1) = false;
    end

    if mp_oxif < 0
           failcheck(2) = true;
        else
           failcheck(2) = false;
    end
end
```

6.8 Initial Determination of Boil-Off Rates via Excel Spreadsheet

For the majority of the project, the team first sought to calculate the boil-off rates of each propellant by iterating upon the wet mass of the spacecraft until it converged (as described in section 2.2.2) using the model presented in section 0, as opposed to selecting a range of propellants and O:F mass ratio. This approach was ultimately changed as there were too many variables between each configuration to compare the boil-off rates of each propellant fairly and accurately. However, the original approach is documented below for completeness, and to showcase the different iterations of this process.

To computationally determine the boil-off rates, the following Excel spreadsheet was first created.

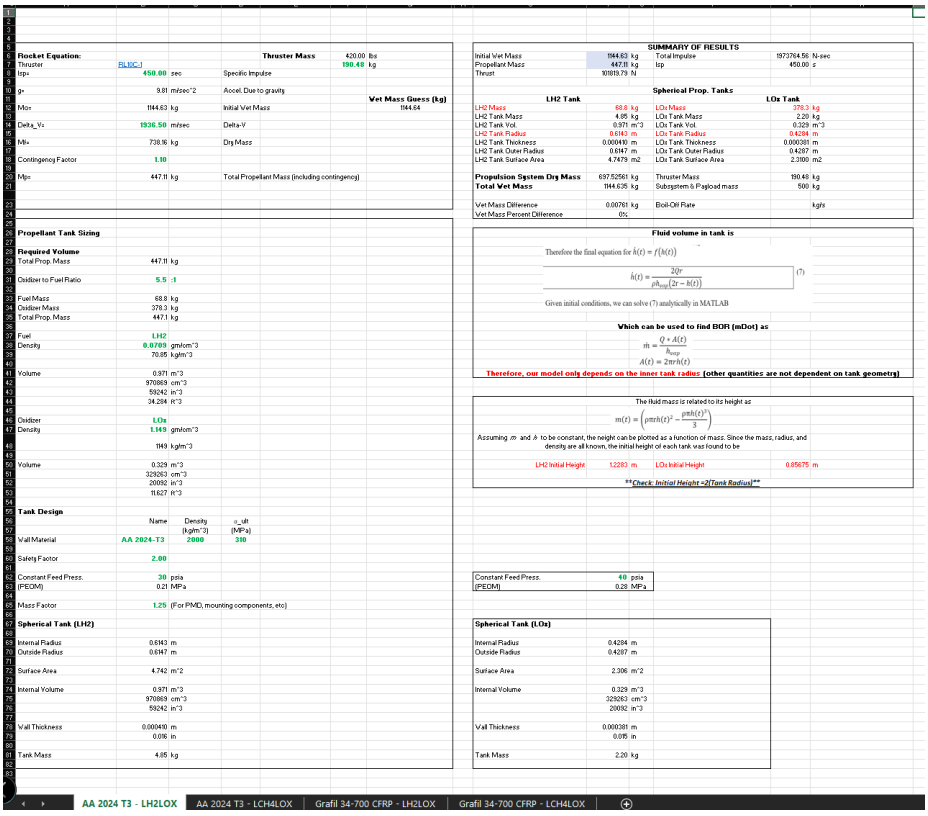

Figure 81: Excel spreadsheet used to determine boil-off rate

The cells in green represent user input data that can be obtained from manufacturer technical data sheets, and the cells in red represent desired outputs. The following parameters were all calculated using the corresponding formulas presented in sections 1.1.4 and 2.2:

- Initial Wet Mass
- Dry Mass
- Total Propellant Mass
- Fuel Mass
- Oxidizer Mass
- Fuel Tank Volume
- Fuel Tank Inner Radius
- Fuel Tank Surface Area
- Fuel Tank Thickness
- Fuel Tank Mass
- Oxidizer Tank Volume
- Oxidizer Tank Inner Radius
- Oxidizer Tank Surface Area
- Oxidizer Tank Thickness
- Oxidizer Tank Mass

Upon setting up the spreadsheet with the corresponding formulas, the thruster I_{sp}, thruster mass, required ΔV, and propellant contingency factor (for a LH_2/LOx configuration, in this case) were first entered in the "Rocket Equation" section of the spreadsheet, as shown below in Figure 82.

1							
2							
3							
4							
5							
6	**Rocket Equation:**				**Thruster Mass**	420.00	lbs
7	Thruster	RL10C-1				190.48	kg
8	Isp=	450.00	sec	Specific Impulse			
9							
10	g=	9.81	m/sec^2	Accel. Due to gravity			
11							**Wet Mass Guess (kg)**
12	Mo=	1144.63	kg	Initial Wet Mass			1144.64
13							
14	Delta_V=	1936.50	m/sec	Delta-V			
15							
16	Mf=	738.16	kg	Dry Mass			
17							
18	Contingency Factor	1.10					
19							
20	Mp=	447.11	kg	Total Propellant Mass (including contingency)			
21							
23							

Figure 82: Rocket Equation section of spreadsheet

Next, the thruster oxidizer-to-fuel ratio, fuel and oxidizer name, densities, and operating pressures, tank material name, density, ultimate strength, safety factor, and mass factor were entered in the “Propellant Tank Sizing” section of the spreadsheet, as shown in Figure 83 and Figure 84.

25							
26	**Propellant Tank Sizing**						
27							
28	**Required Volume**						
29	Total Prop. Mass	447.11	kg				
30							
31	Oxidizer to Fuel Ratio	5.5	:1				
32							
33	Fuel Mass	68.8	kg				
34	Oxidizer Mass	378.3	kg				
35	Total Prop. Mass	447.1	kg				
36							
37	Fuel	LH2					
38	Density	0.0709	gm/cm^3				
39		70.85	kg/m^3				
40							
41	Volume	0.971	m^3				
42		970869	cm^3				
43		59242	in^3				
44		34.284	ft^3				
45							
46	Oxidizer	LOx					
47	Density	1.149	gm/cm^3				
48		1149	kg/m^3				
49							
50	Volume	0.329	m^3				
51		329263	cm^3				
52		20092	in^3				
53		11.627	ft^3				
54							
55	**Tank Design**						
56		Name	Density	σ_ult			
57			(kg/m^3)	(MPa)			
58	Wall Material	AA 2024-T3	2000	310			
59							
60	Safety Factor	2.00					
61							
62	Constant Feed Press.	30	psia				
63	(PEOM)	0.21	MPa				
64							
65	Mass Factor	1.25	(For PMD, mounting components, etc)				
66							
67	**Spherical Tank (LH2)**						
68							
69	Internal Radius	0.6143	m				
70	Outside Radius	0.6147	m				
71							
72	Surface Area	4.742	m^2				
73							
74	Internal Volume	0.971	m^3				
75		970869	cm^3				
76		59242	in^3				
77							
78	Wall Thickness	0.000410	m				
79		0.016	in				
80							
81	Tank Mass	4.85	kg				
82							

Figure 83: Propellant tank sizing section of spreadsheet

Constant Feed Press.	40	psia
(PEOM)	0.28	MPa
Spherical Tank (LOx)		
Internal Radius	0.4284	m
Outside Radius	0.4287	m
Surface Area	2.306	m^2
Internal Volume	0.329	m^3
	329263	cm^3
	20092	in^3
Wall Thickness	0.000381	m
	0.015	in
Tank Mass	2.20	kg

Figure 84: Oxidizer tank sizing section of spreadsheet

After entering this data, the initial total wet mass (cell T21) was calculated by summing the fuel and oxidizer masses, fuel and oxidizer tank masses, thruster mass, and subsystem and payload mass, as shown in Figure 85.

LH2 Tank			LOx Tank		
LH2 Mass	68.8	kg	LOx Mass	378.3	kg
LH2 Tank Mass	4.85	kg	LOx Tank Mass	2.20	kg
LH2 Tank Vol.	0.971	m^3	LOx Tank Vol.	0.329	m^3
LH2 Tank Radius	0.6143	m	LOx Tank Radius	0.4284	m
LH2 Tank Thickness	0.000410	m	LOx Tank Thickness	0.000381	m
LH2 Tank Outer Radius	0.6147	m	LOx Tank Outer Radius	0.4287	m
LH2 Tank Surface Area	4.7479	m2	LOx Tank Surface Area	2.3100	m2
Propulsion System Dry Mass	697.52561	kg	Thruster Mass	190.48	kg
Total Wet Mass	1144.635	kg	Subsystem & Payload mass	500	kg
Wet Mass Difference	0.00761	kg			
Wet Mass Percent Difference	0%				

Figure 85: Mass summary section of spreadsheet

This initial wet mass was then used as the input for the new initial wet mass (cell B12), which automatically updated the spreadsheet to yield a new total wet mass. This process of using

the total wet mass as the initial wet mass was repeated until the total wet mass and initial wet mass converged to the same value.

After competing this iterative process, the fuel and oxidizer mass, as well as the internal radius of each tank, were found. These are the desired outputs as, from 0, the fluid height in each tank only depends on its internal radius (all other parameters are independent the tank geometry). Additionally, from equation (28), the fuel and oxidizer masses are needed to solve for the initial height of each fluid in their corresponding tanks.

After obtaining these values, the fuel or oxidizer mass was plotted against equation (30) (with the corresponding internal tank radius and propellant density) in software such as Desmos to find the fluid height that corresponds to the calculated fluid mass. Since this analysis assumes that each tank is 100% filled, a check one can use to confirm the outputs are correct is to ensure the initial fluid height is equal to twice the internal tank radius, i.e.

$$h_0 = 2r_{inner} \tag{45}$$

Next, using [an earlier version of] the MATLAB script provided in 6.7, the initial fluid height found from the Excel spreadsheet was used to solve equation (30). Then, using these results in equations (25) and (24), the boil-off rate was calculated.

6.9 Rotating Spacecraft Solar Flux Excel Data Table

The table below shows a cut-out of the data table inserted into COMSOL for the rotating spacecraft thermal analysis testing. As seen on the left, the user can adjust the ‘sun – on’ and ‘sun – off’ time, measured in minutes. In this example, the ‘sun – on’ and ‘sun – off’ time is 10 minutes, therefore one full rotation of the spacecraft is 20 minutes and 3 rotations are completed per hour. Two data fidelities were calculated depending on the resolution desired for the COMSOL test. The value of q, the solar flux, is automatically loaded into the cells and adjusted with the ‘sun – on’ and ‘sun – off’ time through the code: =IF(MOD(D4,B3*2)<B3,1360,0), where cell D4 represents the current cell under q, and cell B3 is the ‘sun – on’ and ‘sun – off’ time. The table can then be expanded manually for however long of a study is desired.

Set 'Sun On' / 'Sun Off' Time	0.1 min Fidelity		1 min Fidelity	
10	t	q	t	q
	0	1360	1	1360
	0.1	1360	2	1360
	0.2	1360	3	1360
	0.3	1360	4	1360
	0.4	1360	5	1360
	0.5	1360	6	1360
	0.6	1360	7	1360
	0.7	1360	8	1360
	0.8	1360	9	1360
	0.9	1360	10	0
	1	1360	11	0
	1.1	1360	12	0
	1.2	1360	13	0
	1.3	1360	14	0
	1.4	1360	15	0
	1.5	1360	16	0
	1.6	1360	17	0
	1.7	1360	18	0
	1.8	1360	19	0
	1.9	1360	20	1360
	2	1360	21	1360
	2.1	1360	22	1360
	2.2	1360	23	1360
	2.3	1360	24	1360
	2.4	1360	25	1360
	2.5	1360	26	1360
	2.6	1360	27	1360
	2.7	1360	28	1360
	2.8	1360	29	1360
	2.9	1360	30	0
	3	1360	31	0
	3.1	1360	32	0
	3.2	1360	33	0
	3.3	1360	34	0
	3.4	1360	35	0
	3.5	1360	36	0
	3.6	1360	37	0
	3.7	1360	38	0
	3.8	1360	39	0
	3.9	1360	40	1360
	4	1360	41	1360
	4.1	1360	42	1360
	4.2	1360	43	1360

6.10 General Fluid Systems Simulation Program

In the process of solving the problem of boiling propellant, the team considered using a NASA software called the General Fluid Systems Simulation Program (GFSSP). It was developed by Andre LeClair, Alok Majumdar, and Ric Moore from the Marshall Space Flight Center (MSFC) in Huntsville, Alabama. GFSSP is designed for the simulation of complex models involving fuel and oxidizer, tanks, pipes, insulation and other systems related to spacecraft propellant management. GFSSP uses governing equations referencing thermodynamics and heat transfer to calculate the amount of propellant that would boil away within a tank under certain conditions. This software was used to develop a model of this project to determine how much propellant would boil away over the course of the mission.

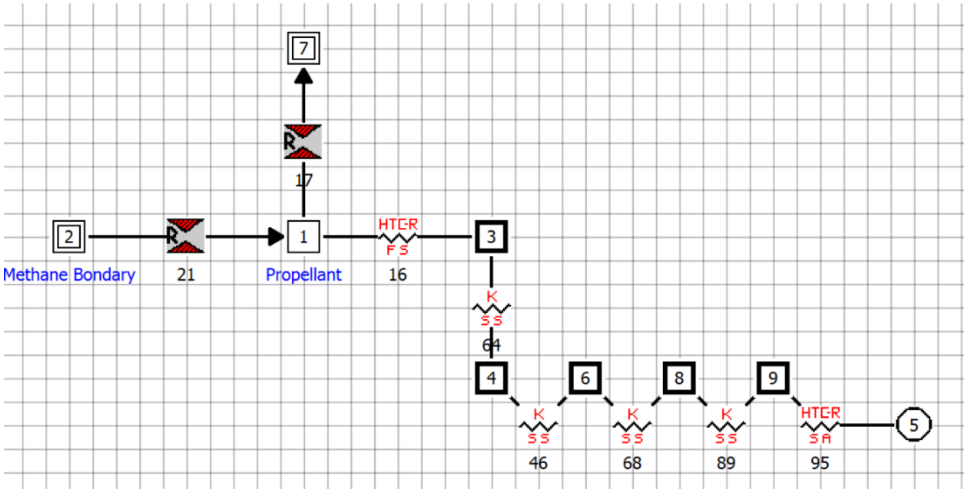

Figure 86: GFSSP model of a tank containing liquid oxygen in deep space

In working with Doctor LeClair, the model shown in Figure 86 was able to be developed, but when refining the model to more specifically match this project's needs, a lack of time and expertise led to unusable results. This software seems highly valuable for a project focused on determining the boil-off of a cryogenic propellant tank, but could not be used for this project.

6.11 Transient Model for Air Flow MATLAB Script

```
clear all
close all
clc

y = 1.4; % spec heat ratio for air
R = 287; % J/kg k
P0 = 284270.84; % Pa, (initial pressure), = 26.53 psig
```

```
T0 = 293; % K
Pa = 101325; % Pa, atmospheric pressure
V = 0.0114; % m^3, = 3 gallons
A = 7.316856334e-7; % m^2, for 0.038 inch orifice
p0 = P0/(R*T0); % kg/m^3, initial density using ideal gas law
m0 = p0*V; % kg


dt = 0.1; %time step
tf = 22; % seconds
tspan = 0.1:dt:tf;

% choked flow for tank pressures greater than 191846.622 Pa (13.1 psig) for venting
into
% sea level atm conditions

% ODE solution:
for t = tspan


    [t1,m1] = ode45(@(t,m) chokedflow(m,t,V,T0,p0,P0,y,R,A),tspan,m0);


end

% Dutton and Coverdill model:
for i = 1:1:22


    tp(i) = i./(V./(A*sqrt(y*R*T0)));
    Pp = (1+((y-1)/2)*((y+1)/2).^((-1*(y+1))/(2*(y-1)))*tp).^((-2*y)/(y-1));


end


j = 1:1:22;

k = 0:28;

P_est = Pp.*P0;

p = m1/V;
P = P0 *(p/p0).^y;

psi = P./6895-14.7;



figure(1)
plot(t1,m1)
title('Air Mass Flow')
xlabel('time (s)')
ylabel('Mass (kg)')
```

```
figure(2)
plot(t1,P,'LineWidth',1)
hold on
plot(j,P_est, 'o','LineWidth',1)
hold off
title('Comparison of Transient Models')
xlabel('time (s)')
ylabel('Pressure (Pa)')
legend('Differential Equation Model', 'Dutton & Coverdill Model')


figure(3)
plot(t1,psi,'linewidth', 1)
hold on
plot(k,VD)
hold off
title('Tank Pressure Over Time')
xlabel('time (s)')
ylabel('Pressure (psig)')
legend('Theoretical', 'Experimental')
% xlim([0 22])

% For constant upstream pressure:

clc
clear all
close all


P = 308167.7;  % Pa, = 110 psig
R = 287; % J/kgk
T = 293; % K
p = 1.2; % kg/m^3
V = 0.0114; % m^3, = 3 gallons
Vdot = 0.00014211667; % m^3/s, volume flow rate of calibrated sonic nozzle
mdot = Vdot*p;

for t = 1:100


    P(t) = 101325+((mdot*R*T)/V)*t;


end

% Insert experimetnal data as PD

psi = (P)./6895-14.7;

x = 0:326;
plot(t,psi,'o')
hold on
plot(x,PD,'linewidth', 1.5)
```

```
title('Tank Pressure Over Time Comparison to Calibration')
xlabel('time (s)')
ylabel('Pressure (psig)')
legend('Theoretical', 'Experimental')

% ODE Function
function mdot = chokedflow(m,t,V,T0,p0,P0,y,R,A)


 mdot = (A*(P0*((m/V)/p0)^y))/(sqrt(T0*((m/V)/p0)^(y-
1)))*sqrt(y/R)*((y+1)/2)*((-y+1)/(2*(y-1)));


end
```